論文 / 著書情報
Article / Book Information

題目(和文)	
Title(English)	New insights on the formation of the terrestrial planets
著者(和文)	MAHJingyi
Author(English)	Jingyi Mah
出典(和文)	学位:博士(理学), 学位授与機関:東京工業大学, 報告番号:甲第12058号, 授与年月日:2021年9月24日, 学位の種別:課程博士, 審査員:井田 茂,中本 泰史,横山 哲也,奥住 聡,太田 健二
Citation(English)	Degree:Doctor (Science), Conferring organization: Tokyo Institute of Technology, Report number:甲第12058号, Conferred date:2021/9/24, Degree Type:Course doctor, Examiner:,,,,
学位種別(和文)	博士論文
Type(English)	Doctoral Thesis

NEW INSIGHTS ON THE FORMATION OF THE TERRESTRIAL PLANETS

by

Jingyi Mah

A thesis submitted to the
Department of Earth and Planetary Sciences
of the
Tokyo Institute of Technology
in partial fulfilment of the requirements for the degree of
Doctor of Science

2021

Abstract

Not only do the sampled terrestrial worlds (Earth, Mars and asteroid 4 Vesta) differ in their nucleosynthetic isotopic compositions of Ca, Ti, Cr and Mo, but in addition the magnitude of these anomalies also appear to correlate with heliocentric distance. These cosmochemistry observations can be used to constrain plausible dynamical mechanisms for planet formation in the inner Solar System. While several studies examining the feeding zones of the terrestrial planets in the framework of the classical and Grand Tack models show that the terrestrial planets are more likely to have formed by the accretion of mostly-local materials with little material mixing in the protoplanetary disc, recent works challenge the 'traditional' view that the terrestrial planets formed by collisions of increasingly massive planetesimals by showing that the accretion of cm- to m-sized planetary bodies known as 'pebbles' can also reproduce the mass-orbit distribution of the terrestrial planets.

In this thesis, we adopt a two-pronged approach to determine the more plausible formation pathway of the terrestrial planets by combining *N*-body simulations with constraints from cosmochemistry data. We apply the pebble accretion model and the depleted disc model to the inner Solar System and study their dynamical outcomes and cosmochemistry implications. For the pebble accretion model study, we modelled the growth of a disc of planetesimals in the terrestrial planet region subjected to a flux of pebbles assumed to originate from the outer Solar System. The simulations were ran for a period of 4 Myr, after which we quantify the amount of mass in pebbles accreted by the inner disc planetesimals. For the depleted disc model study, we simulated the growth of a solid disc in the inner Solar System made up of planetesimals and embryos preferentially concentrated in an annulus within $1 - 1.5$ au sans an inward-drifting pebble flux. The simulations were carried out in two phases: the first 5 Myr with a gas disc and the subsequent 150 Myr without. At the end of the simulations, we compute the feeding zones of the terrestrial planet analogues and the formation location of Vesta analogues.

Our results show that pebble accretion, if it occurred, can increase the mass in the solid disc by at least a few times its initial mass with reasonable assumptions that pebbles fragment to smaller-sized grains at the snow line and that gas-disc-induced orbital migration effects are in force. Such a large contribution in mass by pebbles would imply that the isotopic composition of the inner Solar System would be similar to the outer Solar System, where the pebbles are assumed to have originated from. This implication is in contrast to the observed isotopic dichotomy of the Solar System as sampled by known meteorites. The pebble accretion mechanism, however, is capable of generating a compositional gradient in the inner Solar System only if the planetesimals have diameters less than 300 km because of the dependence of pebble accretion efficiency with distance from the Sun.

The terrestrial planets that formed within the framework of the depleted disc model have feeding zones that correlate with their semi-major axis, indicating that they accreted most of their building blocks locally and that there was limited mixing of the solids in the disc. Furthermore, Vesta analogues also originate from regions in the disc close to Vesta's current orbit. If the isotopic composition of the solids in the inner Solar System was heterogeneous and the isotopes were distributed along a heliocentric gradient, then the results from the depleted disc model imply that Earth, Mars and Vesta can be isotopically distinct.

Based on cosmochemical arguments we conclude that it is unlikely that pebble accretion played a major role in the formation of the terrestrial planets. The terrestrial planets should have formed via the mergers of planetesimals and embryos instead. In addition, there

should have been isotopic gradients in the inner Solar System established before the formation of the planetesimals. The isotopic gradients could have been generated by the accretion of material from the interstellar medium, as suggested by several studies, or that it could be innate to the Solar System.

Publications associated with this dissertation

Parts of this thesis have appeared in the following publications and preprints:

- **Mah, J.**, Brasser, R., 2021. Isotopically distinct terrestrial planets via local accretion. Icarus 354, 114052
- **Mah, J.**, Brasser, R., Mojzsis, S.J., Bouvier, A., Effects of pebble accretion on the growth of planetesimals in the inner Solar System. *in prep.*
- **Mah, J.**, Brasser, R., Woo, J.M.Y., Bouvier, A., Mojzsis, S.J., Evidence for an incipient isotopic gradient in the inner region of the solar protoplanetary disc. *in prep.*

Acknowledgements

I would like to extend my gratitude to the following persons and institutions:

- Ramon Brasser for his guidance and support throughout my time here as a student at the Earth Life Science Institute. His advice and comments, at times critical yet very constructive, have spurred me to challenge limits, push boundaries and reach for greater heights.
- Shigeru Ida for accepting me as a member of his research group, his valuable insights during the early stages of my candidature, and his support on various administrative matters throughout the past three years.
- Tommy Lau and Man Hoi Lee at the University of Hong Kong for their generosity in sharing their *N*-body code. I was able to make more progress in a shorter time with their help.
- Audrey Bouvier, Lucy Kwok, Stephen Mojzsis, Ayame Okuyama, Siau Yong Tan, Chen-En Wei, Emily Wong and Jason Woo for their contributions, in one way or another, to my personal well-being and the enrichment of my student life here in Japan.
- my thesis reviewing committee for their comments to clarify key points and improve the thesis.
- my family for granting me the freedom to pursue my interests and forging my own path in life.
- the Earth Life Science Institute for hosting me as a student and providing me with a comfortable research environment and ample computing resources.
- the Tokio Marine Kagami Memorial Foundation for their generous scholarship that helped to alleviate my financial burden and allow me to focus on my research work.

Contents

List of Figures

List of Tables

1 Introduction

Understanding the formation of the terrestrial planets in our Solar System is a continuous endeavour motivated in part by humanity's curiosity of our own origins. How did the Earth form? What made the Earth? Where can we find clues? These seemingly basic questions turn out to be complex puzzles that require contributions from multiple fields such as astronomy, cosmochemistry and planetary science, to name a few. In recent years, researchers from these apparently disparate but complementary fields have taken notice of the developments in each other's fields and started to collaborate towards achieving a more comprehensive model of planet formation. Some of the results of these studies may be negative, appear inconclusive, challenge long-held perceptions and lead to even more questions, but our understanding of planet formation nevertheless increases because of the debate that these results ignited.

In this thesis, we synthesise state-of-the-art knowledge from theories of planet formation and cosmochemistry data and use this information to answer the question of whether the terrestrial planets grew by the accumulation of small (cm-sized) solids or were they the products of mergers between large (km-sized) planetary bodies. We will put forward a proposal to explain cosmochemistry data trends based on the outcomes of our numerical investigations. The thesis consists of two studies, each examining the formation of the terrestrial planets from one of the two aforementioned pathways. We aim to convey the message that utilising a variety of relevant cosmochemistry data can help to distinguish between different planet formation models and point to the direction(s) that future studies could follow in the quest of gaining full understanding of how the terrestrial planets take shape. In the following sections we will review several dynamical models of planet formation, introduce relevant cosmochemistry data used in our work, and outline the motivation and approach of the studies presented in this thesis.

1.1 Developments in planet formation theories

Studies to unravel the mysteries surrounding the formation pathways of the terrestrial planets have made considerable advances since the initial proposal by Safronov (1969) on the genesis of planetesimals via the agglomeration of dust particles in the protoplanetary disc. It is commonly accepted in the community that the terrestrial planets formed from collisions among protoplanets (also known as planetary embryos) of increasing size, although, as we will later discuss, this paradigm is starting to be challenged. The Classical model of terrestrial planet formation (Chambers, 2001) was built upon the results of early analytical derivations (e.g., Wetherill, 1980; Wetherill and Stewart, 1989) and numerical simulations (Kokubo and Ida, 1995, 1996, 1998) of the evolution of a self-gravitating solid disc of planetesimals. Several planetesimals in the solid disc will grow much faster than the rest and produce a bimodal population in the disc comprising larger-sized planetary embryos and smaller-sized planetesimals (Kokubo and Ida, 1998). The embryos continue growing by accreting nearby planetesimals until they exhaust all the planetesimals in their feeding zones, by which time the embryos will collide and merge among themselves to finally form the terrestrial planets. Chambers (2001) shows that the growth timescales of the terrestrial planets are around several tens of millions of years.

A fundamental shortcoming of the Classical model is that it systematically produces planets that are several times the mass of Mars around 1.5 au. This shortcoming — termed as the 'small Mars problem' — spurred successive improvisations and refinements to the Classical model to form the terrestrial planets with the correct masses and orbits. Several studies found that starting with the gas giants Jupiter and Saturn located near their current orbits but with orbital eccentricities twice their current value (Raymond et al., 2009), or that starting with a narrow ring of material concentrated between 0.7 au and 1.0 au (Hansen, 2009) are favourable initial conditions to reproduce Mars analogues with the correct mass. These studies show that rather specific initial conditions are needed to reproduce the masses and orbits of the terrestrial planets. For example, it was noted by Raymond et al. (2009) that the high eccentricities required of the gas giants are rather unrealistic, and the means to truncate the material in the solid disc is lacking (although see Pierens et al. (2014) and Clement et al. (2021) for the possibility of more eccentric Jupiter and Saturn).

In the following years, a radical proposal for the disc truncation mechanism was put forward. Walsh et al. (2011) presented a scenario wherein Jupiter and Saturn are locked in a mean-motion resonance (MMR) and migrated through the asteroid belt twice — first inwards, then outwards — aided by their interactions with the surrounding gas disc. In the process they concentrated the solid material in the terrestrial region to a narrow annulus. The gas-driven migration of the gas giants, dubbed as the 'Grand Tack', is successful at reproducing the small mass of Mars because the solid disc is truncated at around Earth's orbit and this left the planetesimals in Mars' region with insufficient material to grow to large sizes. The Grand Tack model has since been widely studied (e.g., Jacobson et al., 2014; Jacobson and Morbidelli, 2014; O'Brien et al., 2014; Jacobson and Walsh, 2015; Brasser et al., 2016; Deienno et al., 2016; Matsumura et al., 2016) and became well-established over time because it provided a plausible framework of the evolutionary history of the Solar System in addition to its ability in explaining the low mass of the asteroid belt and the apparent compositional diversity among its constituents (DeMeo and Carry, 2014), which seem to suggest that radial mixing of solid material occurred in the disc.

Despite the successes of the Grand Tack model, there are some studies that scrutinised the model and found that the migration of Jupiter with Saturn in tow depends sensitively on the initial conditions of the gas disc. For example, D'Angelo and Marzari (2012) showed that the outward migration of Jupiter and Saturn to the region beyond 5 au only works for limited values of gas viscosity, surface density and temperature, and Zhang and Zhou (2010) showed that the surface density of the gas disc affects the orbital eccentricities of the gas giants which in turn determines the order of the MMR that they are captured in and whether the MMR is stable.

Alternatives to the Grand Tack scenario as the mechanism to truncate the solid disc have also been proposed. The works of Izidoro et al. (2014, 2015) and Raymond and Izidoro (2017b) explored the possibility of reproducing the orbital configuration of the terrestrial planets and the low mass of the asteroid belt by considering a local mass depletion around Mars' orbit and various surface density profiles of the solid disc. The model achieved success with a very steep solid surface density profile (Izidoro et al., 2015) and also with the extreme assumption that the asteroid belt region was initially devoid of solid material (Raymond and Izidoro, 2017b). It was, however, not further elaborated nor investigated how the presupposed distribution of the solids came to be nor whether such steep density gradients are realistic.

Another model that was recently found to be capable of reproducing the configuration of the inner Solar System is the early instability model (e.g., Clement et al., 2018, 2019). It is the outcome of a sophisticated reinvestigation of the earlier proposed Nice model (e.g., Tsiganis et al., 2005) which is based on the conjecture that a dynamical instability occurred in the outer Solar System sometime in the history of the Solar System that resulted in the observed dynamical features of the current Solar System after a phase of giant planet scattering and migration (Thommes et al., 1999). Clement et al. (2018) found using direct simulations of both the inner and outer Solar System that a giant planet instability occurring within 10 Myr from the time of the dispersal of the gas disc is consistent with many currently observed features of the Solar System. A follow-up study (Clement et al., 2019) with simulations including the effects of collisional fragmentation further revealed that the formation timescale of the terrestrial planets in the framework of this model are also consistent with the measurements from radioactive chronometers (e.g., Touboul et al., 2007; Kleine et al., 2009; Dauphas and Pourmand, 2011).

1.2 Formation of the terrestrial planets: Planetesimals or pebbles?

Until now it seems to be the case that the community is approaching a clearer understanding of the appropriate initial conditions to form the terrestrial planets with the aid of progressively high-resolution simulations performed on fast computers. The dynamical models that we have described so far are based on the conventional understanding that the terrestrial planets evolved to their current size through a series of accretion processes involving increasingly massive planetary bodies. However, there is now an emerging view which postulates that the growth of the terrestrial planets could in fact be a consequence of the accretion of small cm-sized bodies called 'pebbles' instead, in direct challenge to the traditional view. Although the *pebble accretion* model (Ormel and Klahr, 2010; Lambrechts and Johansen, 2012) was originally developed to resolve a problem related to the formation of the core of gas giants, several recent studies (Levison et al., 2015b; Johansen et al., 2021) have applied this model to the terrestrial planet region and found positive results that encourage further investigations on the plausibility of this formation pathway for the terrestrial planets.

Pebbles, observed to be abundant in protoplanetary discs (e.g., Testi et al., 2003; Wilner et al., 2005; Rodmann et al., 2006), are thought to have formed via the coagulation of smaller-sized dust particles in the outer regions of the disc (Lambrechts et al., 2014; Ida et al., 2016). They tend to spiral towards the central star under the influence of gas drag because dynamical friction with the surrounding gas causes them to lose angular momentum (Weidenschilling, 1977). During their passage through the protoplanetary disc these pebbles will encounter planetesimals in the inner Solar System and some of these will have been accreted onto the planetesimals.

The effect of this pebble flux on the formation of the terrestrial planets has been investigated by Levison et al. (2015b) and by Johansen et al. (2021). By adopting specific values for the various parameters of the gas disc, Johansen et al. (2021) showed that it is possible for planetesimals in the inner Solar System to achieve masses close to the current terrestrial planets within the lifetime of the gas disc. The planetesimals that become the terrestrial planets are assumed to have formed at different times and migrated to their current orbits from a distant location. The rapid growth of the terrestrial planets in this model is made possible by the continuous but gradually diminishing flux of pebbles. The authors further proposed that the pebbles that were initially accreted onto the terrestrial planets have composition akin to the volatile-depleted non-carbonaceous (NC) meteorites while the later-accreted pebbles have composition akin to the volatile-rich carbonaceous (CC) meteorites. The proposal is based on a plausible dynamical evolution pathway of protoplanetary discs where material in the inner region tend to spread outwards initially due to viscous expansion but will eventually drift inwards to the central star at a later time. The authors fitted the time for the compositional change to be 3.8 Myr (presumably after the formation of the Calcium-Aluminium-rich inclusions (CAI) usually adopted as time zero for the Solar System; e.g., Amelin et al., 2010; Bouvier and Wadhwa, 2010; Connelly et al., 2012) based on the results of Schiller et al. (2018, 2020) that the fraction of CC in the Earth and Mars could be 42% and 36%, respectively.

The composition of the terrestrial planets is an area of active research and studies adopting different initial conditions and assumptions arrive at different results, although there is a general agreement among earlier works (e.g., Lodders, 2000; Fitoussi et al., 2016; Brasser et al., 2017; Dauphas, 2017; Woo et al., 2018), which we will describe in the next section, that the contribution of CC material to the terrestrial planets should be fairly limited. Based on this assumption, Levison et al. (2015b) investigated the outcome of having the pebbles that form the terrestrial planets originate locally from the inner Solar System instead. In this model, the pebbles contribute to the growth of planetesimals in the inner disc in the first few Myr but the planetary bodies did not reach the full size of the terrestrial planets. Levison et al. (2015b) find that the planetesimals closer to the central star accrete more pebbles and grow to larger sizes compared to planetesimals further away because the pebble accretion cross-section has a semi-major axis dependence resulting from their assumptions on the Stokes number. Mars' smaller size compared to Earth and Venus can therefore be easily reproduced because it formed from the mergers of smaller-sized planetesimals. It is perhaps more accurate to describe the contribution of the pebble accretion mechanism in this model as helping to generate the appropriate initial mass-semi-major axis distribution of planetesimals that would naturally reproduce the masses of the terrestrial planets via subsequent collisions and mergers. However, the model proposed by Levison et al. (2015b) requires a rather high value for the surface density of the gas disc which raises questions about its feasibility and plausibility; in addition, they did not include planet migration in their study.

The results of these studies examining the formation of the terrestrial planets in the framework of the pebble accretion model are indeed interesting and they set the stage for further research in this direction. The work of Levison et al. (2015b) found that pebble accretion played a supportive role in the early growth stages of planetesimals in the inner Solar System while Johansen et al. (2021) reported that pebble accretion could potentially be responsible for the formation of the actual terrestrial planets in one stage. Did pebble accretion play a role in the formation of the terrestrial planets? If it did, how much mass did the pebbles contribute? Further studies would benefit from incorporating constraints from cosmochemistry, as demonstrated in the work of Johansen et al. (2021) (for example) to be useful. In the following section we will delve into the cosmochemistry data that are helpful to our work described in this thesis.

1.3 Cosmochemistry data and trends

1.3.1 Isotopic dichotomy in the Solar System

The bulk isotopic and elemental compositions of a planetary body is the cumulative average of its constituent building blocks (e.g., Drake and Righter, 2002; Fitoussi et al., 2016; Dauphas, 2017; Mezger et al., 2020), and is the end-product of the protoplanetary disc region(s) from which the planetary body accreted. The sampled solar system bodies for which we know (or infer) the parent bodies are: Earth, Moon, Mars and asteroid 4 Vesta. Known Martian meteorites include the Shergotty, Nakhla and Chassigny (SNC) meteorites, ALH 84001, NWA 7034, Tissint, Zagami and some more, while Vesta is very likely to be represented by the Howardite-Eucrite-Diogenite (HED) class of meteorites (e.g., McCord et al., 1970; Consolmagno and Drake, 1977; Binzel and Xu, 1993; Keil, 2002; McSween et al., 2013). Furthermore, asteroids 434 Hungaria and 6 Hebe may also be represented in our meteorite collections (Greenwood et al., 2020) because they could be the parent bodies of the aubrites (Zellner, 1975; Zellner et al., 1977; Clark et al., 2004; Ćuk et al., 2014) and H chondrites, which are one of the components of the ordinary chondrites group (Gaffey et al., 1993; Gaffey and Gilbert, 1998; Binzel et al., 2004, 2019), respectively. Collectively, the meteorites representing these planetary bodies fall into a larger group known as the non-carbonaceous (NC) group based on their bulk isotopic compositions (Warren, 2011). The constituents of the NC group are thought to have originated from the inner Solar System, in contrast to the carbonaceous (CC) group which is thought to represent the outer Solar System (Warren, 2011).

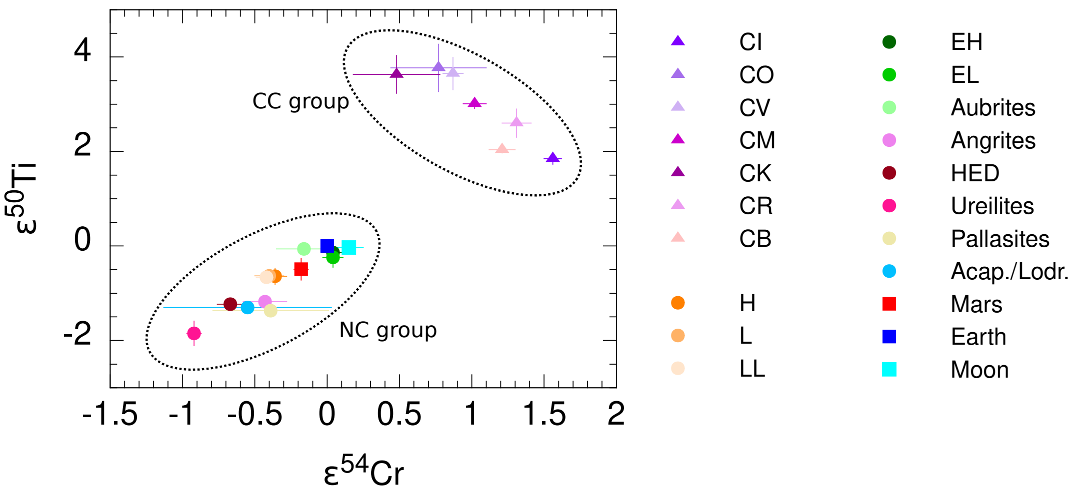

FIGURE 1.1: Measured ε^{50}Ti and ε^{54}Cr isotopic anomalies of known meteorites normalised to the values for the Earth. The meteorites fall into two distinct groups thought to represent the inner and outer Solar System, suggesting that the material in these two regions were kept separate at least until the formation of the chondrites. Acap. and Lodr. are abbreviations for Acapulcoites and Lodranites, respectively. Data sourced from Shukolyukov and Lugmair (2006); Trinquier et al. (2007, 2008, 2009); Qin et al. (2010a,b); Yamashita et al. (2010); Larsen et al. (2011); Petitat et al. (2011); Zhang et al. (2011, 2012); Yamakawa and Yin (2014).

The compositional dichotomy of the Solar System is perhaps most obvious from a plot of ε^{50}Ti versus ε^{54}Cr, which are the most neutron-rich stable isotopes of these elements (Fig. 1.1). The components of the carbonaceous (or jovian) group are relatively enriched in ε^{50}Ti and ε^{54}Cr while the components of the non-carbonaceous (or terrestrial) group are relatively depleted in these isotopes. The clustering of the meteorites into two distinct groups is also observed for many other elements with different geochemical characteristics such as O, Mo, Ni, Ru and W (Qin and Carlson, 2016; Kleine et al., 2020, and references therein). The clear clustering of the meteorites and the dearth of known meteorites plotting in the region connecting the two groups led to the notion that the two meteorite reservoirs are separated in space and/or time (e.g., Warren, 2011). A popular proposal for the means to keep the two reservoirs separated is the formation and growth of Jupiter (Kruijer et al., 2017) — proto-Jupiter with a mass of about 20 Earth masses (M_{E}) (Lambrechts et al., 2014) pushes away the gas near its orbit, creating a gap (density deficit) in the protoplanetary disc that traps inflowing solid material at the outer edge (Morbidelli et al., 2016). Furthermore, Kruijer et al. (2017) showed using iron meteorites — thought to have formed at an earlier time than the chondrites (Kruijer et al., 2014) — that the NC and CC reservoirs must have been separated for at least 4 Myr after the formation of the Solar System. However, the capacity of Jupiter as the purported 'barrier' is challenged by Brasser and Mojzsis (2020) who showed that a substantial amount of outer Solar System material could have flowed past Jupiter into the inner Solar System during Jupiter's growth, 'contaminating' the inner Solar System with outer Solar System material and reducing the isotopic differences between the two regions. Brasser and Mojzsis (2020) proposed instead that the two reservoirs could be separated by the presence of ring-like gaps that are innate to the protoplanetary disc. Despite the ongoing debate, what remains certain is the existence of an early and sustained separation between the inner and outer regions of the protoplanetary disc.

1.3.2 Isotopic heterogeneity in the non-carbonaceous chondrite group and the potential building blocks of the terrestrial planets

Another observation from Fig. 1.1 is the difference in the isotopic compositions of the Earth, Mars, HED meteorites, aubrites and H chondrites despite them being part of the same large NC group. In fact, there are measurable differences in their nucleosynthetic isotope anomalies on the scale of parts per 10^4 to 10^6 for elements such as Ba, Ca, Cr, Fe, Mo, N, Nd, Ni, O, Ru, Sm, Ti, W, Xe and Zr (see Qin and Carlson, 2016, for an in-depth review). The variations in these nucleosynthetic isotopes are due to the particular distribution of presolar dust grains in the Solar protoplanetary disc and are thought to be impervious to planetary processes. Theory dictates that no two planetary bodies will exhibit the same isotopic composition unless they both accreted their building blocks from the same reservoir(s) with the same proportion of nucleosynthetic isotopes. Therefore, the distinct isotopic compositions of the above planetary bodies suggests that there are differences in the compositions of their building blocks which would imply formation at various locations throughout the disc (e.g., Carlson et al., 2018).

In particular, the dissimilarity between Earth's and Mars' isotopic compositions has prompted studies to identify the potential building blocks of the terrestrial planets from known meteorites. In mixing models that use meteorite isotopic compositions as constraints, chondrites (enstatite chondrites (EC), ordinary chondrites (OC) and carbonaceous chondrites (CC)) are more commonly employed as the starting point instead of achondrites because the bulk chemical compositions of the former's parent bodies are better constrained (Dauphas, 2017). The aim of such mixing model is to compute, using the Monte Carlo method, the composition of the terrestrial planets as a mixture of chondrites given constraints from the isotopic anomalies and elemental abundances measured for known chondrites by lowering the χ^2 of the fit.

For the Earth, the best-fit combination obtained from chondritic mixing models give 70% EC + 21% H + 5% CV + 4% CI (Lodders, 2000), 91% EC + 7% OC + 2% CC (Dauphas et al., 2014b), 71% EC + 24% OC + 5% CC (Dauphas, 2017) and 50% angrites + 32% H + 8% CI + 10% CV (Fitoussi et al., 2016) when achondrites are considered, while dynamical modelling arrives at 87% EC + 13% OC in the framework of the Grand Tack model (Brasser et al., 2017; Woo et al., 2018). These results suggest that the dominant building blocks of the Earth are enstatite chondrites (or, more precisely, parent bodies whose isotopic composition are akin to enstatite chondrites) with minor contributions from parent bodies isotopically akin to ordinary and carbonaceous chondrites. Earth's water budget and hydrogen isotope composition also appears to support an enstatite chondrite source (Piani et al., 2020).

This mixing model results for the potential building blocks of the Earth stand in contrast to the results for Mars where the models give 85% H + 11% CV + 4% CI based on oxygen isotopes (Lodders and Fegley, 1997), 45% EC + 55% OC when taking into account chromium, molybdenum, nickel and titanium isotopes (Sanloup et al., 1999; Tang and Dauphas, 2014), 68% EC + 32% OC when combining dynamical simulations with the mixing model (Brasser et al., 2018), and 55% angrites + 36% H + 9% CI in the special case when achondrites are considered (Fitoussi et al., 2016). These results show that the mixture of building material — assuming only chondrites — that went into the Earth is different from that of Mars, and furthermore that the mixtures of each planet are dependent on the isotopes considered in the model.

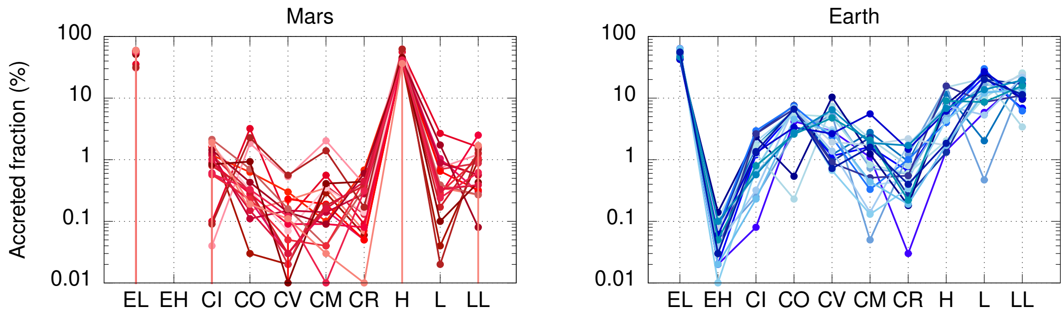

FIGURE 1.2: Contribution of various chondrite group to the composition of Mars and Earth computed from a Monte Carlo mixing model. The model uses meteorite isotopic compositions and elemental abundances as inputs and the isotopic compositions of Earth and Mars (Fitoussi et al., 2016; Dauphas, 2017) as constraints. Shown here are the 20 best-fit combinations (lowest χ^2) from 20 mixing model simulations. The maximum contribution of carbonaceous chondrites to the building blocks of the Earth and Mars is about 10%. Plot taken from Mah and Brasser (2021).

We have also carried out our own computations for the composition of the Earth and Mars assuming only chondritic meteorites as input. We have expanded on the mixing models of Fitoussi et al. (2016), Dauphas (2017) and Brasser et al. (2018) by adding the CM and CR meteorite components of the carbonaceous chondrite variety while separating the CO and CV into individual components. In addition, we also split up the enstatite chondrites and ordinary chondrites — which were taken to be one single component by the previous studies — into their respective components. Our mixing model computes the contribution by each meteorite component while taking into account the isotopic anomalies in Δ^{17}O, ε^{50}Ti, ε^{54}Cr, ε^{62}Ni and ε^{92}Mo and the respective concentration of these elements. A description of the inner workings of our mixing model is given in Appendix A. We show the 20 best-fit compositions of the Earth and Mars obtained from 20 mixing model simulations in Fig. 1.2. Taking the average from the 20 best-fit outcomes, our mixing model gives (52 ± 6)% EC + (36 ± 4)% OC + (12 ± 2)% CC for the Earth and (53 ± 9)% EC + (45 ± 8)% OC + (2 ± 1)% CC for Mars. The uncertainties are given as one standard deviation of the mean. Our results are broadly consistent with those from earlier works where it was found that the contribution of EC and OC are roughly equal for Mars with almost no contribution from CC whereas EC dominates the composition of the Earth with the maximum contribution of CC capped at about 10%. We note that the contribution of EC to Earth is slightly lower in our model compared to previous studies and this is likely due to the large uncertainties in the ε^{92}Mo measurement for the meteorites.

The results of the mixing model studies give us an estimate of the regions in the protoplanetary disc from which the Earth and Mars accreted their building materials. Mars' best-fit chondritic mixture suggests that it could have formed near the boundary between the EC and OC reservoirs while the Earth could have formed in the EC reservoir and further away from the EC-OC boundary (Woo et al., 2018). The contribution of CC to the building blocks of the Earth, however, is open to interpretation. On the one hand, it could be that CC did contribute to the Earth's making by delivering water and other volatiles, although this became disputed by a recent study that reports on the similarity between the deuterium/hydrogen (D/H) ratio of EC and the Earth's mantle (Piani et al., 2020). On the other hand, it is also possible that the mixing model returns CC as part of the Earth's building blocks simply because Earth is an end-member of the non-carbonaceous chondrite group and a mixture of solely EC and OC cannot reproduce the isotopic composition of the Earth; this is especially true for oxygen.

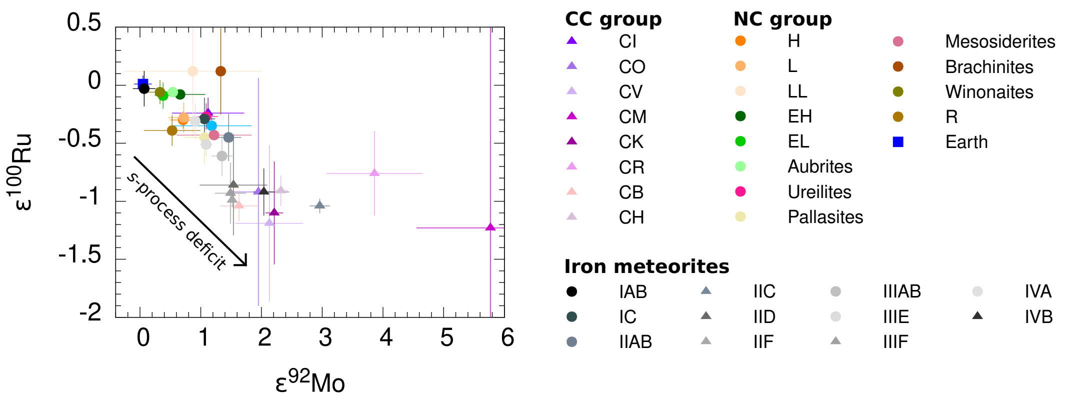

FIGURE 1.3: Measured ε^{92}Mo and ε^{100}Ru isotopic anomalies of known meteorites normalised to the values for the Earth. All the known meteorites plot to the lower right following a trend of increasing deficit of *s*-process isotopes and perhaps also an increasing formation distance from the Sun. The Earth has an end-member composition that prompted proposals that it accreted material from a possibly extant reservoir enriched in *s*-process isotopes. Data for ε^{92}Mo sourced from Dauphas et al. (2002); Burkhardt et al. (2011, 2012, 2014, 2017); Budde et al. (2016, 2018, 2019); Kruijer et al. (2017); Poole et al. (2017); Render et al. (2017); Worsham et al. (2017, 2019); Bermingham et al. (2018); Hilton et al. (2019); Hopp et al. (2020); ε^{100}Ru data are from Chen et al. (2010); Fischer-Gödde et al. (2015); Bermingham and Walker (2017); Burkhardt et al. (2017); Fischer-Gödde and Kleine (2017); Bermingham et al. (2018); Worsham et al. (2019); Hopp et al. (2020).

It has been shown (e.g., by Drake and Righter, 2002 and more recently, a review by Mezger et al., 2020) that the current repository of known meteorites does not constitute the whole picture of the Earth's building blocks. Earth's location as an end-member in plots of Ti versus Cr (Fig. 1.1; Trinquier et al., 2009; Warren, 2011) and Ru versus Mo (Fig. 1.3; Dauphas et al., 2014a; Fischer-Gödde et al., 2015) could also hint at an additional reservoir in the region closer to the Sun than where the ECs are thought to have formed. Fig 1.3 illustrates the fact that one cannot get the isotopic composition of the Earth by mixing EC, OC and CC. This therefore prompted the suggestion of the existence of an additional reservoir characterised by an enrichment in *s*-process isotopes. The Earth should have accreted some material from this reservoir to offset the *s*-process deficit signature of the other meteorites (Fischer-Gödde and Kleine, 2017; Render et al., 2017). However, meteorite samples from this *s*-process-enriched reservoir have not been found to date and it has been suggested that all the material from this reservoir have been accreted into the terrestrial planets (Drake and Righter, 2002; Burkhardt et al., 2011, 2016). Indeed, Fischer-Gödde et al. (2020) may have found evidence of this reservoir in ancient terrestrial rocks that show positive ε^{100}Ru anomalies, but more measurements are needed to confirm this hypothesis.

1.3.3 Potential isotopic gradients in the inner Solar System and the origins of the isotopic heterogeneity

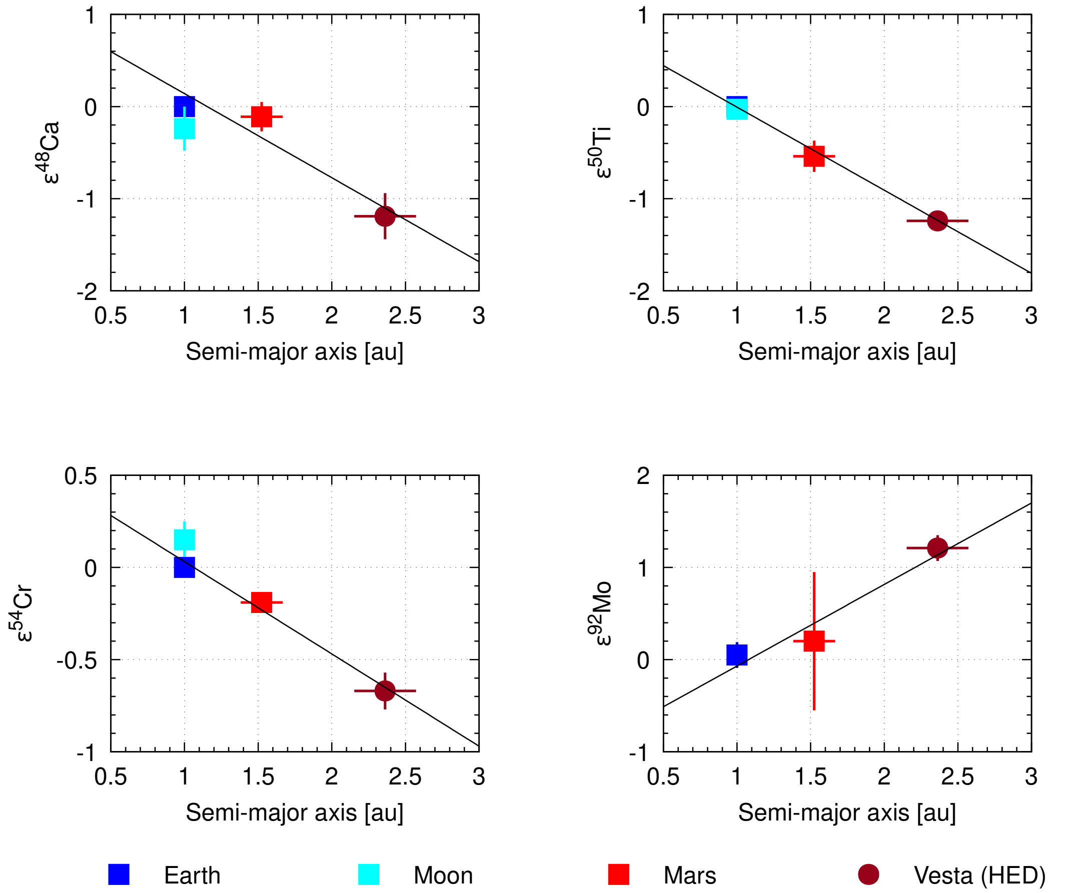

FIGURE 1.4: Calcium, titanium, chromium and molybdenum isotopic anomalies for the Earth, Moon, Mars and Vesta (sampled by the HED meteorites) plotted with respect to the semi-major axes of these planetary bodies. The isotopic compositions of these planetary bodies appear to correlate with their distance from the Sun, hinting at the presence of isotopic gradients in the inner Solar System (e.g., Trinquier et al., 2009; Yamakawa et al., 2010). Data sourced from the compilation of Dauphas (2017) and references therein. The ε^{92}Mo data point for HED is plotted using data for Mesosiderites sourced from Dauphas et al. (2002) because measurements for HED meteorites are unavailable in the literature.

Examining the isotopic composition of the Earth with respect to several other differentiated bodies in the inner Solar System could help in understanding the bigger picture of how planetary bodies in the inner Solar System formed. Several works (e.g., Trinquier et al., 2009; Yamakawa et al., 2010) identified an apparent correlation between the isotopic anomalies in ε^{50}Ti and ε^{54}Cr and the semi-major axis of the Earth, Mars and Vesta (HED meteorites). We show in Fig. 1.4 that the reported correlation also exists for ε^{48}Ca (e.g., Schiller et al., 2018) and possibly for ε^{92}Mo (e.g., Burkhardt et al., 2011).

The origin of the observed correlations in ^{50}Ti and ^{54}Cr favoured by Yamakawa et al. (2010) is that Type 1a supernovae supplied these isotopes to the inner Solar System just before the formation of the planetesimals that became the precursors of Earth, Mars and Vesta, although the supernova-origin view is still highly debated. The authors argued for a short isotope delivery timing because of the rapid homogenisation of nuclides in the protoplanetary disc. Results of hydrodynamical simulations show that radionuclides injected by supernovae spread out evenly in the protoplanetary disc in 10^3 to 10^6 years (e.g., Ouellette et al., 2009, and references therein). The correlated isotopic compositions of the Earth, Mars and Vesta therefore reflects a potential gradient in the distribution of ^{50}Ti and ^{54}Cr isotopes in the inner protoplanetary disc where there is an increased depletion of these isotopes with increasing distance from the Sun. Furthermore, the isotopes ε^{48}Ca, ε^{50}Ti and ε^{54}Cr show the same trend (Fig. 1.4) because they are thought to share a common origin, i.e., a supernovae source (e.g., Hartmann et al., 1985; Woosley, 1997; Wanajo et al., 2013). The trend for ε^{92}Mo is different because Mo isotopes are synthesised via the *p*-, *s*- and *r*- processes (e.g., Brennecka et al., 2013).

The origin of the observed diversity in the isotopic anomalies of the differentiated bodies in the inner Solar System is still not well known. It is commonly thought to be the product of imperfect mixing of dust and gas during the early stages of the Solar System's formation (e.g., Birck, 2004; Andreasen and Sharma, 2007; Trinquier et al., 2007; Brennecka et al., 2013). There have been several proposals to explain how the heterogeneity came about. The first of these is that the heterogeneity is a 'cosmic chemical memory' that the Solar nebula inherited during its birth in the natal molecular cloud (Clayton, 1982; Dauphas et al., 2002) which could have been the shell of a Wolf-Rayet star's wind bubble (Dwarkadas et al., 2017). The second group of proposals accounting for the heterogeneity calls for the late addition of external material from the interstellar medium. It has been suggested that fresh ejecta from asymptotic giant branch (AGB) stars or supernovae was added late into the Solar nebula (Trinquier et al., 2007), or that there was a temporal change in the composition of infalling material from the molecular cloud, with early infalling material having CC composition and later infalling material having NC composition (Nanne et al., 2019). The third group of proposals relates the isotopic heterogeneity to physical processes in the Solar nebula itself. Thermal gradients in the protoplanetary disc could have selectively remove volatile elements, moderately-volatile elements and thermally-unstable presolar silicates in the region closer to the Sun, creating a compositional gradient with distance from the Sun (e.g., Trinquier et al., 2009; Burkhardt et al., 2012; Ek et al., 2020). Furthermore, thermal processing could also modify the composition of infalling material from the molecular cloud (Ek et al., 2020). Other than thermal gradients in the disc, the outward-then-inward movement of the water snow line throughout the lifetime of the disc has also been suggested to be the mechanism to generate two planetesimal populations with distinct compositions in the inner and outer Solar System (Lichtenberg et al., 2021).

Recently, there is also a new interpretation of the isotopic data. Schiller et al. (2018) suggested that the ε^{48}Ca isotopic heterogeneity among the Earth, Mars and Vesta is correlated with the masses (and sizes) of these planetary bodies and could reflect instead their different accretion timescales, i.e., Vesta accreted earliest, followed by Mars and finally, the Earth. The authors suggest that the correlation is due to a change in the inner Solar System's composition and that the change could be brought about by the influx of pebbles from the outer Solar System. Assuming that the initial composition of the planetesimals in the inner Solar System is initially homogeneous and akin to those of the ureilites (a type of primitive achondrite with the lowest abundance of ε^{48}Ca), Schiller et al. (2018) showed that the gradual accretion of CI carbonaceous chondrite-like material from the outer disc over the lifetime of the gas disc is consistent with the isotopic compositions of Earth, Mars and Vesta. The interpretation that the isotopic heterogeneity among the major inner Solar System bodies is generated by the introduction of outer Solar System material over time is in contrast with the interpretations by other authors described in the previous paragraphs that the isotopic differences present in the major planetary bodies reflect a spatial heterogeneity in the protoplanetary disc. This proposal formed the basis of further investigations by Johansen et al. (2021) who used semi-analytical simulations to study the feasibility of forming the terrestrial planets via pebble accretion (described earlier in Section 1.2), although they did not perform a suite of *N*-body simulations.

1.4 Key questions and structure of thesis

High-precision isotope data of meteorites made available in the past decade have been gradually adopted by studies seeking to understand how the terrestrial planets formed. The distinct isotopic compositions of the Earth and Mars have been employed to constrain dynamical models of planet formation. Previous studies examining the classical model (Chambers, 2001) found that the feeding zones (region of the protoplanetary disc where a planet sourced most of its building material) of the terrestrial planets show a correlation with their semi-major axis (e.g., Raymond et al., 2004; O'Brien et al., 2006; Fisher and Ciesla, 2014; Kaib and Cowan, 2015; Woo et al., 2018). This is because the planets are thought to grow by the accretion of solid material within their respective feeding zones in the classical model. Consequently, Earth and Mars' isotopic differences can be reproduced if the material that these two planets accreted have different isotopic compositions. However, forming Mars analogues at 1.5 au with the correct mass is a fundamental shortcoming of this model.

Studies examining the Grand Tack model (Walsh et al., 2011) found that the feeding zones of the terrestrial planets are wide and strongly overlapping with no obvious correlation with semi-major axis (Brasser et al., 2017; Woo et al., 2018). The main reason for this outcome is the migration of the gas giants. Jupiter and Saturn's excursion through the asteroid belt region excited the orbits of the material in the terrestrial planet region and caused them to undergo mixing (Carlson et al., 2018). If there was a difference in the composition of the material in the terrestrial planet region, it is expected that the difference will be homogenised. The similar feeding zones of the terrestrial planets in the Grand Tack model thus imply that they should have similar compositions, in contrast with the isotope data. However, there is still a low but non-zero probability ($< 5\%$) that Mars analogues can have feeding zones that are distinct to that of the Earth (Brasser et al., 2017; Woo et al., 2018).

The terrestrial planet feeding zones computed from the classical and Grand Tack models suggest that the formation pathway of the terrestrial planets is more likely to follow the classical model, i.e., the planets accreted the majority of their building blocks locally within their feeding zone with limited mixing of material in the disc. This is backed up by very recent high-resolution simulations run on graphics cards (Woo et al., 2021). In addition, the growth of the terrestrial planets should have proceeded via collisions among planetesimals followed by collision among larger-sized planetary embryos. This view is recently challenged by studies showing that pebble accretion could have contributed (in various extents) to the formation of the terrestrial planets (Levison et al., 2015b; Johansen et al., 2021). The contribution from pebble accretion, if found to be substantial, could potentially change our understanding of planet formation in our Solar System because it is also associated with the interpretation of the isotope data proposed by Schiller et al. (2018). It is therefore eminent to conduct further investigations to understand how pebble accretion works in the inner Solar System.

In this thesis, we will study the formation of planetary bodies in the inner Solar System as a whole. We will use the correlation between isotopic compositions of Earth, Mars and Vesta and their respective semi-major axis, as well as the distinct compositions of these planetary bodies as additional constraints to help us understand their formation pathway and formation location. To this end, we will employ a two-pronged approach. We will examine two different models of planet formation — the pebble accretion model (Ormel and Klahr, 2010; Lambrechts and Johansen, 2012), and the depleted disc model (Izidoro et al., 2014, 2015) — with the aim of answering the following questions:

- Did pebble accretion play a role in the inner Solar System?
- Are the distinct isotopic compositions of the terrestrial planets and Vesta a natural outcome of the depleted disc model?
- Did the terrestrial planets primarily form by the accretion of pebbles or planetesimals, or a mixture of both?

The remainder of this thesis is made up of two chapters dedicated to the results of our studies on the pebble accretion model and the depleted disc model, and one chapter summarising our work followed by a discussion of potential future investigations. In Chapter 2 we report the results of our examination of the pebble accretion model. We applied the model to the inner Solar System to study the growth of a disc of planetesimals subjected to inward-drifting pebbles from the outer Solar System over the lifetime of the gas disc. In particular, we will quantify the amount of mass increase in the solid disc by the end of this period. We will also discuss if the pebble accretion mechanism can generate a compositional gradient in the inner Solar System and if its implications for the composition of the terrestrial planets are consistent with cosmochemistry data.

In Chapter 3 we report the dynamical outcomes of the depleted disc model. We constructed a solid disc containing both planetary embryos and planetesimals based on the original model proposed by Izidoro et al. (2014, 2015) but using a more realistic gas disc model developed by Ida et al. (2016). The solids are preferentially concentrated within 1 au – 1.5 au to mimic a mass concentration in the terrestrial planet region and a mass depletion beyond the orbit of Mars. We compute the feeding zones of the terrestrial planets formed in this model and determine if the distinct isotopic compositions of Earth, Mars and Vesta can be reproduced naturally.

Finally, in Chapter 4 we summarise the outcomes and implications of the two studies presented in this thesis and discuss possible future directions to take in the quest of gaining a more comprehensive understanding of how the terrestrial planets in our Solar System formed. Last but not least, the novel points of our studies are: (1) we conduct high-resolution N-body simulations with a wide range of initial conditions for the gas disc to quantify the effects of pebble accretion in the inner Solar System, and (2) we are the first to study in detail the dynamical outcomes and cosmochemistry predictions of the depleted disc model by using a realistic gas disc model and testing for a variety of initial conditions.

2 Role of pebble accretion the inner Solar System

2.1 Introduction

In this chapter we study the effects of pebble accretion in the inner Solar System when Jupiter is still growing. We will use N-body simulations to model the growth of planetesimals in the inner Solar System that are subjected to a flux of pebbles over the course of Jupiter's growth, with the aim of quantifying the amount of mass delivered to the inner disc by pebble accretion. Our motivation stems from the promising results of several previous works, both from the aspects of planetary dynamics and cosmochemistry, that reported the potential of the pebble accretion mechanism (e.g., Lambrechts and Johansen, 2012) to lay the groundwork for the formation of the terrestrial planets (e.g., Levison et al., 2015b; Johansen et al., 2021) and its capability of explaining the correlation between the ε^{48}Ca isotopic composition and the mass (or size) of the Earth, Mars and Vesta (Schiller et al., 2018). However, there have also been reports (Brasser and Mojzsis, 2020; Kleine et al., 2020) challenging the efficiency of Jupiter as a competent barrier in preventing excessive pebbles from entering the inner Solar System and maintaining the isotopic dichotomy. In the following we briefly describe the method and outcome of several previous works that investigated the feasibility of the pebble accretion mechanism in forming the terrestrial planets.

The work of Levison et al. (2015b) employed numerical simulations to study the effect of pebble accretion in the inner Solar System. They subjected a population of planetesimals distributed between 0.7 au and 2.7 au to a flux of inward drifting pebbles that are continuously generated in the same region over a period of 2 Myr. The planetesimals are embedded in a gas disc with an r^{-1} (r is the distance to the star) surface density function. Since the pebbles are formed continuously in the inner Solar System, the surface density of the gas was chosen to be about 5 times the minimum mass solar nebula (MMSN; Hayashi, 1981), a value deemed sufficient to sustain continuous pebble formation in the disc in their simulations. Simulations with sufficient mass to form the terrestrial planets are continued for another 120 Myr. Levison et al. (2015b) found that the small mass of Mars is a natural outcome of their model because the efficiency of planetesimals to grow via pebble accretion decreases with distance from the star. The key assumption of this work is the local formation of pebbles that contributed to the mass of planetesimals that went on to form the terrestrial planets via planetesimal mergers. It is based on observations that show the composition of outer Solar System material to be too distinct to have contributed much to the terrestrial planets as well as the fact that the flux of pebbles necessary to form the giant planets (Levison et al., 2015a) is too great to form the terrestrial planets. The assumption of local pebble formation over time is, however, rather peculiar and deviates from the more common assumption used in many studies (including ours) that the pebbles originate in the outer Solar System.

Johansen et al. (2021) propose that the planetesimals that went on to become the terrestrial planets (Venus, Earth and Mars) all formed initially near the water snow line, and that these planetesimals subsequently migrated inwards to the current semi-major axis of the terrestrial planets while accreting pebbles along the way. The snow line in their disc model is initially located between 1.2 au to 2.0 au and migrates inwards with time. The planet formation scenario presented in their work is based on good analytical fits of the growth track equations of Johansen et al. (2019). The masses of Venus and Mars can be reproduced using reasonable values of the disc temperature profile ($T \propto r^{-3/7}$; Chiang and Goldreich, 1997), Stokes number ($10^{-3} < \mathcal{S} < 0.1$) and pebble flux. The study assumes that these planets' current masses are their masses at the time of gas disc dissipation, and that both Venus and Mars grew entirely from pebbles without giant impacts. Johansen et al. (2021) state that these planets began forming near 1.6 au and migrated to their current locations, and accreted mm-sized pebbles from inside the snow line. For Earth, the maximum mass achieved after the end of the pebble accretion phase (when the gas disc has dissipated) is 0.6 Earth mass ($M_{\rm E}$). A giant impact with a body of mass 0.4 $M_{\rm E}$ later in time is suggested so that the mass of the Earth can reach its current value, but it is unclear whether the impactor that formed the Moon had such a high mass. In their model, the terrestrial planets (Venus, Mars and proto-Earth) accreted pebbles of two different compositions in the sequence of (1) non-carbonaceous (specifically, ureilite-like) in the first few Myr, followed by (2) carbonaceous (specifically, CI-like) until the dissipation of the gas disc. They assume that $\sim 40\%$ of Earth's composition comes from pebbles that originated in the outer Solar System with an assumed CI-like isotopic composition (Schiller et al., 2018, 2020). The low mass of Mars can be achieved by assuming that it formed later than the other terrestrial planets. While the suggestion of planetesimal formation triggered by snow line passage is not new (Drążkowska and Alibert, 2017), the only manner in which this can result in planetesimals with a different composition is if the material that condensed at the snow line to become planetesimals has a different composition at a different distance to the Sun, which Johansen et al. (2021) argue occurred because of the initial viscous expansion of the disc. Planetesimal formation at a static snow line is difficult to reconcile with different isotopic compositions.

The major differences between our work and the studies summarised previously lie in the gas disc model we adopted (which we describe in Appendix B.1) and the computation and underlying assumptions of the value of the Stokes number. In our simulations, we follow Ida et al. (2016) and compute the radius and the Stokes number of the pebbles self-consistently depending on their location in the disc, and time. In contrast, the Stokes number used in the work of Levison et al. (2015b) is fixed while Johansen et al. (2021) assume that it lies in a particular range and that the pebbles are mm-sized. Our simulations are in a sense more realistic concerning the treatment of pebbles, but the downside is that a longer computational time is required and that our gas disc model may be too simplistic.

In the next subsection we will describe how pebble accretion works for planetesimals of different sizes and a minor but important modification to our numerical code that we inherited from Matsumura et al. (2017). This is followed by a description of the initial conditions of our simulations and the simulation outcomes. The content that we will henceforth present is currently in preparation for submission to a peer-reviewed journal.

2.2 Pebble accretion onto planetesimals

2.2.1 Basic formulation

Based on the formulation of Ormel and Klahr (2010) and Ormel and Kobayashi (2012) and modified by Ida et al. (2016), the accretion rate of cm-sized pebbles onto a planetesimal of mass M and located at distance r from the central star is derived to be

$$\dot{M} = \min\left[1, \frac{C\hat{b}^2\sqrt{1+4\mathcal{S}^2}}{4\sqrt{2\pi}\mathcal{S}\hat{h}_{\rm peb}}\left(1+\frac{3\hat{b}}{2\chi\eta}\right)\right]\dot{M}_{\rm F}, \tag{2.1}$$

where $\dot{M}_{\rm F}$ is the flux of pebbles through the disc at a specific location from the star; its temporal evolution depends on the gas accretion rate onto the central star and the formation efficiency of pebbles. We denote using a circumflex the quantities that are scaled by distance to the star. The pebble mass flux $\dot{M}_{\rm F}$ is one of the key quantities that control the pebble accretion rate. For our fiducial disc model it is given by (Ida et al., 2016)

$$\dot{M}_{\rm F} = 10^{-3}\alpha_3^{-1}\dot{M}_{*8}\left(\frac{L_*}{L_\odot}\right)^{2/7}\left(\frac{M_*}{M_\odot}\right)\left(\frac{t+t_{\rm off}}{1\ {\rm Myr}}\right)^{-1/3} M_{\rm E}\ {\rm yr}^{-1}, \tag{2.2}$$

where $\alpha_3 \equiv \alpha/10^{-3}$, α is the disc viscosity (also see Eq. B.2; Shakura and Sunyaev, 1973), $L_*(L_\odot)$ is the luminosity of the star (Sun), $M_*(M_\odot)$ is the mass of the star (Sun) and $t_{\rm off}$ is the timescale at which the planetesimals are assumed to instantaneously form. The other key quantity that influences the pebble accretion rate is the collision impact parameter b, which takes the form

$$b = 2\kappa R_{\rm H}\mathcal{S}^{1/3}\ \min\left(\sqrt{\frac{3R_{\rm H}}{\chi\eta r}}\mathcal{S}^{1/6}, 1\right), \tag{2.3}$$

where κ is the reduction factor accounting for cases where pebbles are weakly coupled to the gas resulting in inefficient accretion, $R_{\rm H} = r(M/3M_*)^{1/3}$ is the Hill radius of the planetesimal, $\mathcal{S}$ is the Stokes number which determines the degree of coupling between the pebbles and the gas, and η is the difference between the gas and Keplerian velocity. The terms in the parentheses encompass the two possible pebble accretion regimes, namely the Bondi regime (left-hand term) where the relative velocity between the planetesimal and a pebble is dominated by the pebble's drift velocity, and the Hill regime (right-hand term) where the relative velocity is dominated by Keplerian shear. The quantity χ is a function of the Stokes number $\mathcal{S}$, and is defined as

$$\chi = \frac{\sqrt{1+4\mathcal{S}^2}}{1+\mathcal{S}^2}, \tag{2.4}$$

The Stokes number itself is given by

$$\mathcal{S} = \frac{\rho_{\rm peb}R_{\rm peb}}{\rho_{\rm g}h_{\rm g}}\max\left(1, \frac{4R_{\rm peb}}{9\lambda}\right), \tag{2.5}$$

where $\rho_{\rm peb}$ and $R_{\rm peb}$ are the bulk density and the physical radius of a pebble, $\rho_{\rm g}$ is the gas midplane density, $h_{\rm g} = H_{\rm g}/r$ is the reduced disc scale height, and λ is the mean free path of the pebble. The gas midplane density $\rho_{\rm g}$ is related to the disc surface density $\Sigma_{\rm g}$ and the disc scale height $H_{\rm g}$ via

$$\rho_{\rm g} = \frac{\Sigma_{\rm g}}{\sqrt{2\pi}H_{\rm g}}, \tag{2.6}$$

where $H_{\rm g} = c_{\rm s}/\Omega_{\rm K} \propto T^{1/2}$ is a function of the disc temperature T, the sound speed $c_{\rm s}$ and the Keplerian orbital frequency $\Omega_{\rm K} = \sqrt{GM_*/r^3}$. The pebble mean free path is given by

$$\lambda = \frac{\mu m_{\rm H}}{\sigma_{\rm H_2}\rho_{\rm g}}, \tag{2.7}$$

where μ is the mean molecular weight of the gas (mostly hydrogen), $m_{\rm H}$ is the mass of a hydrogen atom (mostly that of the proton), and $\sigma_{\rm H_2}$ is the collisional cross section of a hydrogen molecule. The reduction factor κ is a function of the Stokes number, expressed as (Ormel and Kobayashi, 2012)

$$\ln \kappa = -\left(\frac{\mathcal{S}}{\mathcal{S}^*}\right)^{0.65}, \tag{2.8}$$

where the quantity $\mathcal{S}^*$ is defined as

$$\mathcal{S}^* = \min\left[2, 4\eta^{-3}\frac{M}{M_*}\right]. \tag{2.9}$$

The quantity η is the difference between the gas and Keplerian velocities due to the gas pressure gradient. It is given by

$$\eta = \frac{1}{2}h_\mathrm{g}^2\left|\frac{\mathrm{d}\ln P}{\mathrm{d}\ln r}\right|. \tag{2.10}$$

The remaining quantities in Eq. 2.1 that we have yet to describe are the constant C that determines the mode of accretion (whether 2D or 3D) and the pebble scale height h_peb. These quantities are expressed as

$$C = \min\left(\sqrt{\frac{8}{\pi}}\frac{h_\mathrm{peb}}{b}, 1\right), \tag{2.11}$$

and

$$h_\mathrm{peb} = \left(1 + \frac{\mathcal{S}}{\alpha_\mathrm{t}}\right)^{-1/2} h_\mathrm{g}, \tag{2.12}$$

where α_t is the gas disc's turbulent viscosity. Pebble accretion begins in 3D mode ($C \sim 1$) when the planetesimal is of low mass and then transitions into the 2D mode when the planetesimal grows larger and its Hill radius becomes larger than the scale height of the pebbles h_peb.

2.2.2 Application to small planetesimals

According to Ormel and Klahr (2010) pebble accretion causes rapid growth onto planetesimals with diameters of $\sim$ 200 km or greater. To understand how pebble accretion works on small(er) bodies the question becomes which of the paths in the min() statements in Equations 2.1, 2.3, 2.9 and 2.11 dominate.

We mentioned previously that the two key quantities controlling the pebble accretion rate are the global pebble flux $\dot{M}_\mathrm{F}$ and the impact parameter b. In the following, we will demonstrate that the reduction factor κ (Eq. 2.8) turns out to be important as well. The quantity $\mathcal{S}^*$ (Eq. 2.9) sets the boundary between the so-called *settling regime*, in which the cross section for accretion is very large (Ormel and Kobayashi, 2012), and the *geometric regime*, in which the cross section is just the surface area of the planetesimal (Ormel and Klahr, 2010). The two regions are smoothly connected with the parameter κ, whose functional form is a fit that Ormel and Klahr (2010) obtained from numerical experiments. The critical Stokes number that separates the settling regime from the geometric regime results in $\mathcal{S}^* < 2$. At around 1 au, this translates to a critical planetesimal-to-star mass ratio of $M/M_* < \frac{1}{2}\eta^3 \lesssim 1.4 \times 10^{-9}$ which corresponds to a diameter of D = 1200 km for a bulk density of ρ = 3000 kg m^{-3} for the planetesimal, assuming nominal disc quantities (see Appendix B.1 for a description of our disc model). This critical value of M/M_* has a distance dependence. For example, at 3 au $\mathcal{S}^* < 2$ when the planetesimal mass is $M/M_* < 3.5 \times 10^{-9}$, or equivalent to a diameter of 1700 km. As such, when a planetesimal at 3 au has a diameter smaller than about twice that of Ceres, or that it is roughly 1200 km if it is located at 1 au, the quantity $\mathcal{S}^*$ can become smaller than 2, meaning that for these cases we are no longer in the settling regime and are instead approaching the geometric regime where the accretion cross section reduces to the surface area of the planetesimal. This has important implications with regards to the pebble accretion rate and efficiency of planetesimals below a critical diameter at a given semi-major axis.

In the asteroid belt, the typical value for the pebble Stokes number $\mathcal{S}$ is 0.1 and the quantity $\mathcal{S}^*$ is often equal to 2 (Ida et al., 2016). For these values, the reduction factor $\kappa = 0.87$. Suppose now that we want to study accretion onto the parent body of the HED meteorites, which, despite existing controversies, we here assume to be the asteroid 4 Vesta (McCord et al., 1970; Consolmagno and Drake, 1977; Binzel and Xu, 1993; Keil, 2002; McSween et al., 2013). Vesta's diameter is $D \sim 500$ km and $M/M_* = 1.3 \times 10^{-10}$. For our nominal disc model at 2.5 au (where Vesta is currently located), $\eta \sim 3 \times 10^{-3}$ and $\mathcal{S}^* \sim 0.02$. If the Stokes number is the typical value of 0.1 then $\kappa = 0.06$, but if $\mathcal{S}$ is higher then κ will be lower, resulting in a much lower rate of accretion than when the impact parameter is almost equal to the Hill radius. Pebble accretion onto the proposed H-chondrite parent body 6 Hebe (Gaffey et al., 1993; Gaffey and Gilbert, 1998; Binzel et al., 2004, 2019), with $D \sim 200$ km and $M/M_* \lesssim 7 \times 10^{-12}$, is much less efficient yet again because the quantities $\mathcal{S}^*$ and κ work out to be $\lesssim 10^{-3}$ and $\lesssim 2 \times 10^{-9}$, respectively. Thus, because of the κ factor, which is related to how the pebbles accrete in the settling regime (Ormel and Klahr, 2010; Ormel and Kobayashi, 2012), accretion onto small objects with $D \sim 200$ km could become *extremely inefficient*. However, the impact parameter b must always be equal to or greater than the radius of the planetesimal for it to be physically meaningful. For a planetesimal with bulk density $\rho = 3000$ kg m^{-3} we have $R/r_\mathrm{H} \sim 5.7 \times 10^{-3}$ so that the relative impact parameter in terms of the Hill radius cannot go much below this value. The revised impact parameter therefore should read

$$b = \max\left[2\kappa r_\mathrm{H}\mathcal{S}^{1/3}\ \min\left(\sqrt{\frac{3r_\mathrm{H}}{\chi\eta r}}\mathcal{S}^{1/6}, 1\right), R\right], \tag{2.13}$$

where R is the radius of the planetesimal. This shows that the accretion rate of pebbles cannot become arbitrarily low, but that small planetesimals are still severely disadvantaged in terms of their accretion rate over their larger brethren.

2.2.3 The role of the snow line and fragmentation

Morbidelli et al. (2016) suggest that the pebbles lose their volatiles at the snow line and could fragment into mm-sized grains akin to chondrules. This fragmentation, if confirmed by mechanical arguments, lowers the Stokes number (Eq. 2.5). The Stokes number can either be $\mathcal{S} \propto R_\mathrm{peb}$, called the Epstein regime, or $\mathcal{S} \propto R_\mathrm{peb}^2$, called the Stokes regime, depending on the distance to the star and the properties of the gas disc. The transition between the two regimes occurs at (Ida et al., 2016)

$$r_\mathrm{ES} = 2.2\rho_\mathrm{peb}^{-7/26}\left(\frac{L_*}{L_\odot}\right)^{-3/13}\left(\frac{M_*}{M_\odot}\right)^{17/26}\left(\frac{\dot{M}_\mathrm{F4}^{1/3}\dot{M}_{*8}}{\alpha_3}\right)^{21/52}\ \mathrm{au}, \tag{2.14}$$

where $\dot{M}_\mathrm{F4} \equiv \frac{\dot{M}_\mathrm{F}}{10^{-4}\ M_\mathrm{E}\ \mathrm{yr}^{-1}}$, and $\dot{M}_{*8} \equiv \frac{\dot{M}_*}{10^{-8}\ M_\odot\ \mathrm{yr}^{-1}}$, . For nominal gas disc temperature and surface density at 1 au, the pebble mean free path $\lambda \sim 2$ cm. Inside the snow line, where fragmentation could occur, the pebble radius is assumed to be $R_\mathrm{peb} \sim 1$ mm (Morbidelli et al., 2016) and so in this case $\mathcal{S} \propto R_\mathrm{peb}$ because $R_\mathrm{peb} \ll \lambda$ (Eq. 2.5). Assuming a pebble density of $\rho_\mathrm{peb} = 1000$ kg m^{-3}, the Stokes number at 1 au for nominal disc parameters is approximately $\mathcal{S} \sim 0.2$, but after fragmentation it is lowered to $\mathcal{S} \sim 10^{-4}$ (Brasser and Mojzsis, 2020).

With the reduction of the Stokes number at 1 au from $\mathcal{S} \sim 0.2$ to $\mathcal{S} \sim 10^{-4}$ as a consequence of potential fragmentation, pebble accretion only becomes inefficient once $\mathcal{S}^* \lesssim 2 \times 10^{-5}$, i.e., when $M/M_* \lesssim 10^{-14}$, which corresponds to a planetesimal diameter of $D \lesssim 50$ km. This critical diameter is lower than that derived previously for the case where fragmentation is not considered (cf. $D \sim 200$ km). With the inclusion of the fragmentation effect the range of planetesimal diameters for which pebble accretion can proceed efficiently is wider. However, the accretion rate depends strongly on the Stokes number, and a lower Stokes number actually results in a much slower rate of accretion with everything else being equal. Nevertheless, due to the debilitating effect of κ, accretion onto small planetesimals by fragmented pebbles is still faster than by intact pebbles beyond the snow line. As such, if fragmentation occurred, pebble accretion onto planetesimals with a diameter comparable to the H-chondrite parent body or smaller can still proceed, albeit with low efficiency, but only as long as they remain inside the snow line. In conclusion, the temporal evolution of the snow line plays a critical role in the growth rate of planetesimals in the inner disc from the inward spiralling pebbles.

2.2.4 Analytical computation of pebble accretion rate

We combine all of these aspects to show a global accretion map in Fig. 2.1, which is a contour plot of $\log(M_\mathrm{f}/M_\mathrm{i})$, i.e., the final mass of a planetesimal divided by its initial mass. The map was created by integrating Eq. 2.1 as a function of time either for at most 4 Myr or until the pebble isolation mass (Lambrechts et al., 2014) was reached. The pebble isolation mass of a planetary body is the mass above which pebble accretion stops due to the planetary body causing perturbations in the disc that halt the flow of pebbles (Lambrechts et al., 2014). Each data point on the map is the result of an integration of a single planetesimal at a fixed location. We assume the temperature of the gas disc to be 200 K at 1 au. The disc evolution that was used follows that outlined in Appendix B.1 and the pebble flux is computed using Eq. 2.2.

The top row of Fig. 2.1 has $t_\mathrm{off} = 0.1$ Myr, the middle row has $t_\mathrm{off} = 0.5$ Myr and the bottom row has $t_\mathrm{off} = 1$ Myr. These three different starting times account for the delay in the timing of planetesimal formation in the disc. The left column has fragmentation included while the right does not. It is clear that the mass distribution is bimodal: planetesimals either grow large or they barely grow at all. This result is mainly dependent on the initial diameter of the planetesimals, which in turn determines their pebble accretion efficiency. If their diameter is below a critical value (which has a slight dependence on disc parameters), then they are in the geometric regime and thus accreting pebbles is very inefficient regardless of their distance to the Sun (purple region in the left side of all the panels in Fig. 2.1). If they are larger than the critical diameter, then they are in the settling regime wherein the pebble accretion efficiency is high, and they will thus experience more growth. The planetesimal's critical diameter between the geometric and settling regimes depends on the location in the disc, the formation time of the planetesimal, whether pebble fragmentation at the snow line is assumed, and also very likely the temperature of the disc (although this factor is not investigated here).

Without fragmentation (right column of Fig. 2.1) only planetesimals with $M \gtrsim 3 \times 10^{-5}\ M_\mathrm{E}$ ($D \gtrsim 500$ km) will efficiently accrete pebbles, with a slight dependence on their initial location in the disc; everything smaller will barely accrete anything (large purple region in the left part of the panels in the right column of Fig. 2.1). Fragmentation, on the other hand, allows for the creation of a narrow annulus of large bodies between 0.8 au to at most 1.5 au whose exact extent depends on the time of the formation of the planetesimals relative to the evolution of the snow line (left column of Fig. 2.1). The snow line does not

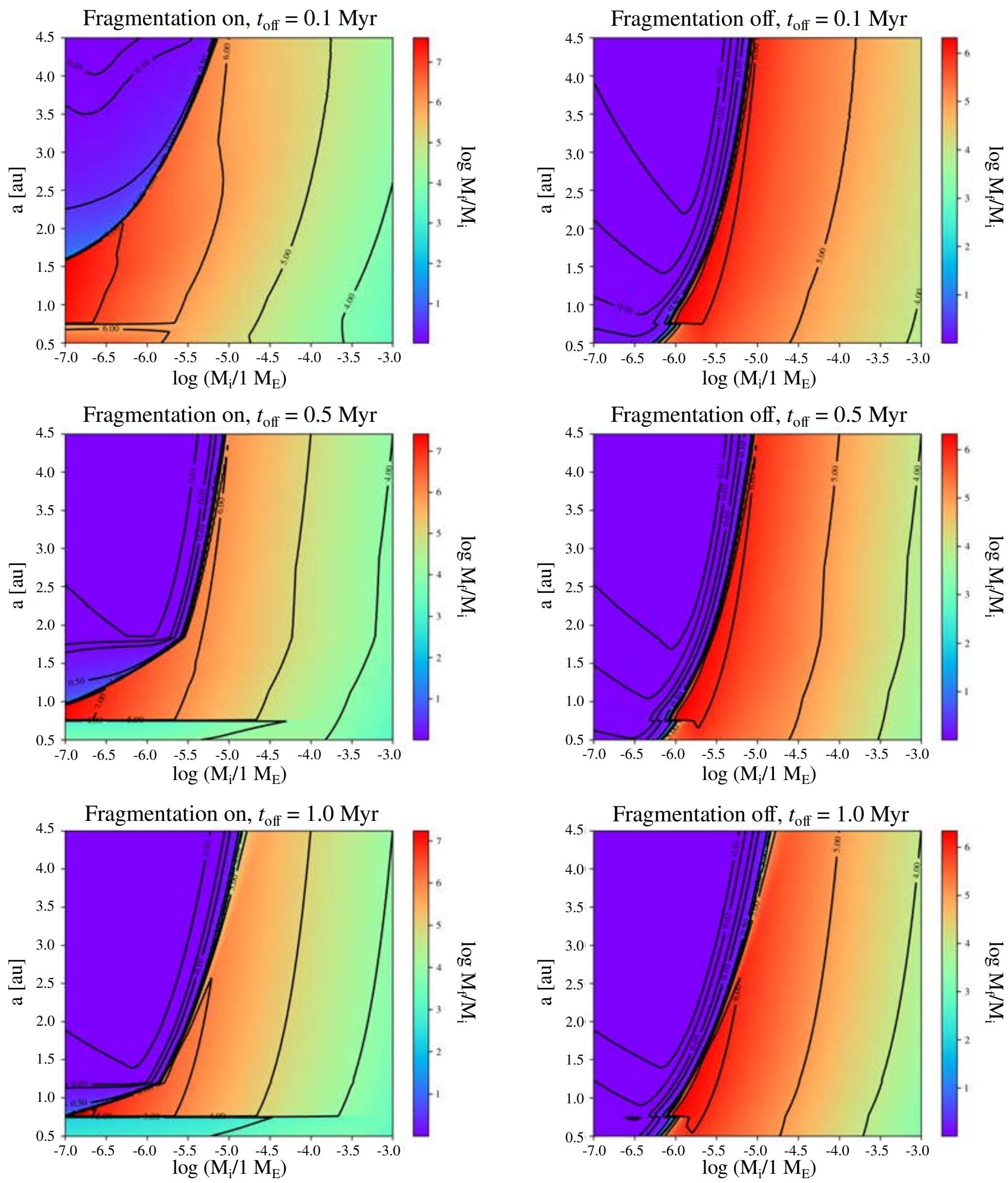

FIGURE 2.1: Contour plot depicting final mass $M_{\rm f}$ of planetesimals after a phase of pebble accretion as a function of their initial mass $M_{\rm i}$ and semi-major axis, with and without pebble fragmentation at the snow line. The top row assumes all planetesimals form together with the disc at $t = 0.1$ Myr, the middle row assumes planetesimal formation after 0.5 Myr and the bottom row after 1 Myr. Regardless of our choice of parameters (initial planetesimal size, planetesimal semi-major axis, planetesimal formation timing, inclusion/exclusion of fragmentation effects), pebble accretion onto small planetesimals in the asteroid belt is very inefficient. The planetesimal diameter can be computed from $\log(D/1\ \mathrm{km}) = \frac{1}{6}\log(M/1\ M_{\rm E}) + 3.597$, so that $M/M_{\rm E} = 10^{-5}$ corresponds to $D = 580$ km.

reach inside 0.75 au so accretion inside of this distance can be inefficient if planetesimals are predominantly small ($D \lesssim 300$ km) and formed late ($t_{\rm off} \gtrsim 1$ Myr). In our fiducial model the snow line is at 1.2 au when $t+t_{\rm off} = 1$ Myr, and it passes 2 au by the time $t+t_{\rm off} = 0.44$ Myr, thus substantial pebble accretion in the terrestrial planet region can only occur if planetesimals form very early and/or form large. In the asteroid belt region accretion generally stops really early on, at a time comparable to the formation age of the iron meteorites, and possibly before most chondrule formation ages – typically about 1.5 Myr (Luu et al., 2015) – because of the rapid inward migration of the snow line. Beyond 2 au accretion is generally insubstantial for small planetesimals.

What is further evident in Fig. 2.1 is that more mass is accreted closer to the Sun than farther away (Ida et al., 2016). In other words, pebble accretion creates a gradient in mass per unit distance. Accretion is more efficient closer to the star, everything else being equal, so pebble accretion naturally creates a compositional gradient in the solid part of the inner disc, with the innermost planetesimals near Mars' orbit being more enriched in outer Solar System (jovian) material than planetesimals in the (outer) asteroid belt.

2.3 Methodology of *N*-body simulations

In essence, we investigate the growth of a disc of planetesimals that is subjected to a flux of inward drifting pebbles ($\rho_{\rm peb} = 1000$ kg m^{-3}, $R_{\rm peb} = 10$ cm) originating from a pebble front located in the outer Solar System beyond the orbit of Jupiter (e.g., Lambrechts and Johansen, 2014; Ida et al., 2016) over the lifetime of the gas disc.

2.3.1 Gas disc model

We include a gas disc based on the model of Ida et al. (2016) in our simulations, with the detailed prescriptions given in Appendix B.1. The gas disc is a steady accretion disc with a constant value for α (viscosity parameter; Shakura and Sunyaev, 1973). The temperature of the disc depends on two heating sources, i.e., viscous dissipation or stellar irradiation, which dominate at different regions of the disc. Equations describing the disc temperature profiles Eq. B.4 due to the aforementioned heating sources are obtained from empirical fits to the disc model of Garaud and Lin (2007). The thermal structure of the disc in turn determines the scale height and surface density.

In our simulations, the gas disc dissipates away with time and was photoevaporated away in 500 kyr when the stellar accretion rate $\dot{M}_* < 10^{-9}\ M_\odot\ {\rm yr}^{-1}$. We further include the effects of disc-induced orbital migration and orbital eccentricity damping (Appendix B.2; e.g., Tanaka et al., 2002; Matsumura et al., 2017) and gas envelope accretion for massive bodies (Appendix B.3; Matsumura et al., 2017). We also simulate for the case where orbital migration is excluded.

The starting time t_0 of our simulations is chosen to be 0.4 Myr after the formation of the CAIs. This value of t_0 determines the initial values of the stellar accretion rate $\dot{M}_*(t = t_0)$ and the initial pebble flux $\dot{M}_{\rm F}(t = t_0)$ in the simulation. It also plays a role in computing the subsequent values of $\dot{M}_*(t)$ and $\dot{M}_{\rm F}(t)$ throughout the simulation. In our simulations, the initial stellar accretion rate $\dot{M}_* = 2.63 \times 10^{-8}\ M_\odot\ {\rm yr}^{-1}$ and the initial pebble flux $\dot{M}_{\rm F} = 10^{-4}\ M_{\rm E}\ {\rm yr}^{-1}$.

2.3.2 Pebble accretion

The pebble accretion formulation we use in this work is based on previous studies that have developed and refined the formulation (e.g., Ormel and Klahr, 2010; Ormel and Kobayashi, 2012; Ida et al., 2016), and studies which applied it to the formation of the giant planets in our Solar System and found success in building the cores of giant planets quick enough to allow gas envelope accretion before the dissipation of the gas (e.g., Lambrechts and Johansen, 2012, 2014). We apply the equations derived by Ida et al. (2016) for the pebble accretion rate at different locations in a steady state accretion disc while taking into account the various properties of the gas disc (e.g., temperature, surface density, scale height). We chose to use this particular pebble accretion formulation for its simplicity and elegance, and because it does not invoke any additional assumptions (such as was done by Levison et al., 2015b; Johansen et al., 2021).

The pebbles are assumed to have originated in the outer regions of the protoplanetary disc where most of the solids (dust) are located (e.g., Youdin and Shu, 2002; Garaud, 2007; Birnstiel et al., 2012). In this region, sub-micron-sized dust grains can grow into pebbles because their growth timescale is much shorter than their migration timescale and the collision rate is low (Birnstiel et al., 2012). Upon reaching a critical size (or a critical Stokes number), the migration timescale becomes comparable to the growth timescale and the pebbles commence their inward migration towards the Sun by virtue of gas drag (Ida et al., 2016). Due to the strong radial dependence of the growth timescale, there will be a location in the disc where dust clumps have just reached pebble size and start to migrate inwards. This is known as the pebble formation front and it moves outwards with time until it reaches the outer edge of the protoplanetary disc (Lambrechts and Johansen, 2014; Ida et al., 2016), after which the pebble flux is severely reduced because all the solids in the disc have been consumed (e.g., Chambers, 2016; Sato et al., 2016).

We implemented the pebble accretion prescriptions of Ida et al. (2016) into the N-body code based on that presented in Matsumura et al. (2017). We do not directly compute the growth of planetesimals by accretion of physical pebbles, but instead compute their mass increase based on the pebble flux at their respective locations in the disc. Pebble accretion onto planetesimals occurs outside in, that is, planetesimals at the outer edge of our solid disc are the first to encounter the pebbles. They will accrete a fraction of the pebbles, reducing the pebble flux by a factor of $1-\dot{M}_{\mathrm{p}}/\dot{M}_{\mathrm{F}}$. The planetesimals that are next in line will see a reduced pebble flux and the amount of pebbles they can accrete is computed from the reduced pebble flux. Furthermore, when a planetesimal (or more accurately, planetary embryo) reaches its pebble isolation mass $M_{\mathrm{p,iso}} \sim 1/2(h_{\mathrm{g}}/r)^3 M_*$ we assume that its accretion stops and pebbles are prevented from flowing past its orbit to other planetary bodies residing closer to the Sun. We assume that pebbles were fragmented (or sublimated) into grains of 1 mm when they cross the snow line on their path towards the Sun (Morbidelli et al., 2016). We also study the outcome of excluding this effect.

2.3.3 Initial conditions

Our planetesimal disc contains planetary bodies with an initial density of $\rho = 2500$ kg m^{-3} and diameter D assigned following a cumulative size-frequency distribution of $N(>D) \propto D^{-5/2}$ (Fig. 2.2). Their orbital eccentricities e and orbital inclinations I are assigned at random from a uniform distribution with intervals [0,0.01) and [0°,1°), respectively. The remaining orbital angles (longitude of ascending node Ω, argument of periapsis ω and mean anomaly $\mathcal{M}$) are assigned values between 0° and 360°, also randomly chosen from a uniform distribution. The semi-major axis of the planetesimals ranges from 0.5 au $< a <$ 2.0 au and they are distributed according to an r^{-1} surface density profile. Our choice to limit the outer edge of the solid disc to 2 au is guided by the analytical results in Fig. 2.1 and our intent to save computation time (our simulations contain a fairly large number of planetesimals and they are all self-gravitating). Furthermore, planetesimals smaller than $D \lesssim 500$ km located beyond 2 au are not expected to grow by much (Fig. 2.1), whereas for bodies with diameter larger than 500 km the growth can be substantial (Brasser and Mojzsis, 2020).

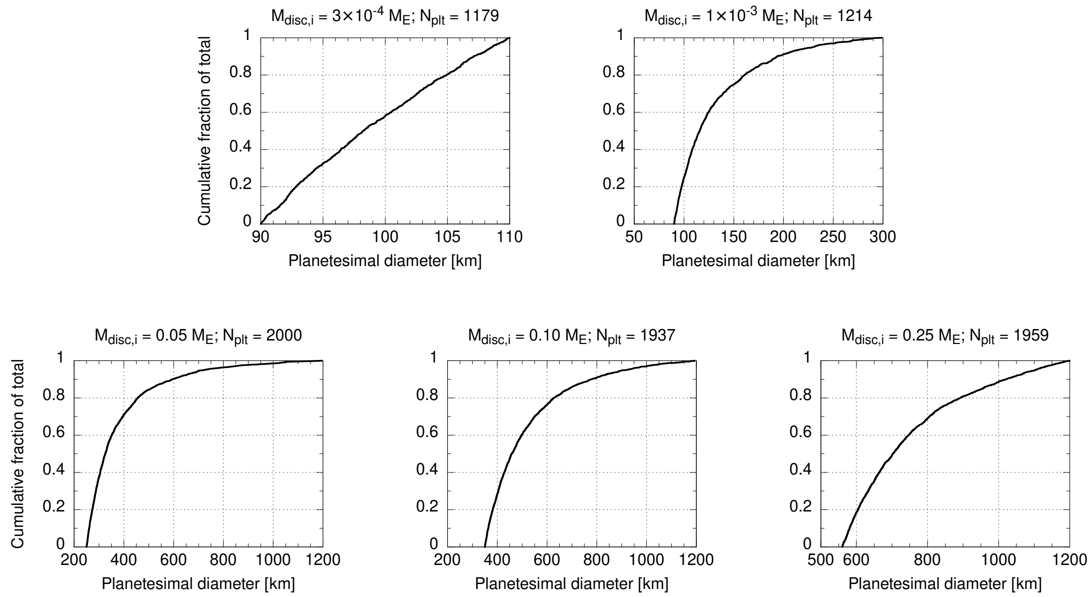

FIGURE 2.2: Cumulative distribution of planetesimal diameter D for various values of initial solid disc mass $M_{\text{disc,i}}$.

TABLE 2.1: Initial solid disc mass $M_{\text{disc,i}}$ in units of Earth masses, range of planetesimal diameters D in each disc, and initial number of planetesimals in each disc N_{plt} for the pebble accretion simulations. We repeat the simulations using the same set of initial conditions shown here for different values of initial disc temperature $T_{1\text{ au}} = 200$ K, 250 K, and 300 K.

$M_{\text{disc,i}}$ (M_E)	D (km)	N_{plt}
3×10^{-4}	$90-110$	~ 1200
1×10^{-3}	$90-300$	~ 1200
0.05	$250-1200$	~ 2000
0.10	$350-1200$	~ 2000
0.25	$560-1200$	~ 2000

The variables in our simulations are: (1) the initial solid disc mass $M_{\text{disc,i}}$, (2) the range of planetesimal diameters D, and (3) the initial disc temperature at 1 au ($T_{1\text{ au}} = 200$ K, 250 K, and 300 K) which corresponds to different disc scale heights h_g and pebble scale heights h_{peb}. The lower mass discs ($M_{\text{disc,i}} = 3\times10^{-4}\ M_E,\ 1\times10^{-3}\ M_E$) contain ~ 1200 planetesimals while the more massive discs contain $\sim$ 2000 planetesimals. All the planetesimals in our simulations are self-gravitating, that is, they are able to interact with each other via gravity. We summarise the initial conditions in Table 2.1.

Our choice of planetesimal diameters are based on the results of previous works. The characteristic diameter of early planetesimals that formed via turbulent concentration or streaming instability in a Solar-like protoplanetary disc ranges from $\sim$ 100 km up to maybe

1000 km (e.g., Chambers, 2010; Johansen et al., 2014; Klahr and Schreiber, 2020), with a size-frequency distribution that follows a shallow power law $N(> D) \propto D^{-1.8}$ for diameter, corresponding to $N(> M) \propto M^{-0.6}$ for mass (e.g., Johansen et al., 2015; Simon et al., 2016; Schäfer et al., 2017; Abod et al., 2019). Models of the collisional evolution of the asteroid belt also suggest that the primordial asteroids were typically 100 km in diameter (Morbidelli et al., 2009). The combined results of these studies suggest that the initial planetesimal population likely consisted of many small planetesimals and a few massive bodies. Vesta could be one of the early-formed massive bodies at the tail end of the distribution.

In addition to the planetesimal disc, following the work of Brasser and Mojzsis (2020) our initial set-up also includes a 0.01 M_{E} planetary embryo placed at 5.2 au that would eventually become Jupiter. When Jupiter reaches its pebble isolation mass (20 M_{E}; Lambrechts et al., 2014) in about 1 Myr (Kruijer et al., 2017), it starts to open a partial gap in the disc around its orbit that prevents pebbles from beyond its orbit to spiral in towards the Sun, effectively shutting off the pebble flux to the inner Solar System (Lambrechts et al., 2014), although particles with sizes $\lesssim$ 100 μm are still able to pass through unobstructed (Paardekooper and Mellema, 2006).

We employ the SyMBA N-body code (Duncan et al., 1998) modified to include a pebble accretion subroutine (described in Section 2.2; Matsumura et al., 2017) and all the additional effects described in this paragraph to carry out our simulations. For each value of $M_{\mathrm{disc,i}}$ we ran one simulation for each permutation of initial conditions (disc temperature $T_{1\ \mathrm{au}}$, fragmentation on/off, migration on/off). In total we ran 60 simulations. The simulations were ran for 4 Myr with a time step of 0.01 yr.

We quantify the amount of mass increase in the inner Solar System resulting from the accretion of pebbles by computing the ratio of the final mass of the planetesimal disc versus its initial mass $M_{\mathrm{disc,f}}/M_{\mathrm{disc,i}}$. For the more massive discs ($M_{\mathrm{disc,i}} \geq 0.05\ M_{\mathrm{E}}$), the larger planetesimals will accrete pebbles efficiently and they can grow to large masses quickly, as we will show in the following section. Therefore, the final disc mass for these cases do not only reflect growth via pebble accretion, but also additional growth due to mergers and gas envelope accretion. However, the additional growth processes from mergers and gas envelope accretion should not affect the cosmochemical outcome and the conclusion of this study.

2.4 Results

2.4.1 Amount of mass increase in the inner disc

We present the results for the ratio of the final mass in the disc to its initial mass ($M_{\mathrm{disc,f}}/M_{\mathrm{disc,i}}$) in the region between 0.5 au and 2.0 au plotted with respect to the initial disc mass and the disc temperature in Fig. 2.3. We find that the final mass of the solid disc depends mostly on its initial mass. A higher initial disc mass results in a higher final disc mass because these discs have, on average, a higher number of large planetesimals which are more efficient at accreting pebbles. This result is similar to the outcome of the single-planetesimal computations shown earlier in Fig. 2.1, which illustrates that a planetesimal's accretion regime abruptly transitions from the less efficient geometric regime to the more efficient settling regime when their masses are above a critical threshold given a specific set of gas disc parameters. We also observe a general inverse correlation between the amount of mass increase and the initial temperature of the gas disc because (1) for hotter discs the scale height is higher and this lowers the pebble accretion efficiency (Ida et al., 2016), and (2) the snow line is on average farther away in hotter discs than in cooler discs.

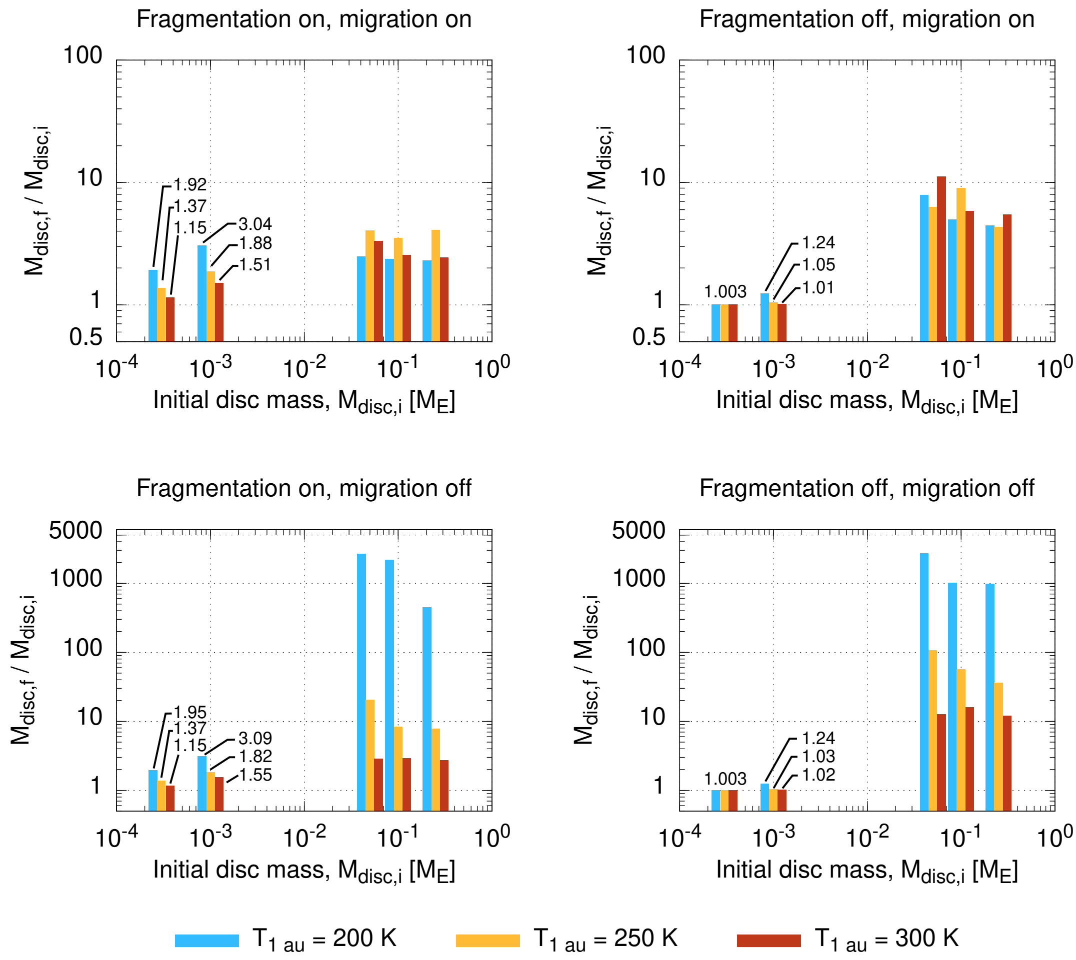

FIGURE 2.3: Ratio of final mass in the disc to its initial mass ($M_{\mathrm{disc,f}}/M_{\mathrm{disc,i}}$) in the region between 0.5 au and 2.0 au as a result of pebble accretion over a period of 4 Myr since the formation of CAIs, plotted with respect to the initial disc mass and disc temperature. The accretion efficiency depends on the sizes of the planetesimals. Large amounts of mass in the form of pebbles can still be accreted by large planetesimals within 2 au before Jupiter reaches its pebble isolation mass at $t = 1.5$ Myr.

Our results show that the growth of small planetesimals with $D \lesssim 300$ km located between 0.5 au and 2.0 au is very limited as they are not in the settling regime. The final mass of the disc is not affected by disc-induced migration effects because these planetesimals do not have the opportunity to grow to large sizes for migration to be significant. On the other hand, there is an observable difference in the final disc mass due to pebble fragmentation effects. If pebble fragmentation at the snow line is taken into consideration, we find that the final disc mass is about 1 to 2 times higher and 1.5 to 2.5 times higher respectively for discs with initial mass $M_{\mathrm{disc,i}} = 3 \times 10^{-4}\ M_{\mathrm{E}}$ ($D \approx 100$ km) and $M_{\mathrm{disc,i}} = 1 \times 10^{-3}\ M_{\mathrm{E}}$ (90 km $\leq D \leq$ 300 km), compared to the case when fragmentation effects are excluded. The numerical N-body simulations confirm that small planetesimals have difficulty accreting pebbles efficiently if the pebbles did not break into smaller sizes at the snow line. The discs containing planetesimals with $D \lesssim 110$ km barely grow at all (just a 0.3% increase) while the discs containing planetesimals with $D \lesssim 300$ km recorded a growth ranging from 1 – 2% for hot discs to 24% for cold discs.

When planetesimals are larger their growth is affected by both disc-induced migration and pebble fragmentation effects. Compared to fragmentation, migration effects exert a stronger influence on the final mass in the disc. In the extreme case where migration is excluded, the final solid mass of planetesimals in cold discs can reach a few hundred to a few thousand times their initial mass due to gas envelope accretion onto planetary embryos (Ikoma et al., 2000). Indeed, the combined effects of a lower gas disc scale height and a closer-in snow line results in a high accretion efficiency that allows planetesimals to grow to large sizes very quickly with some planetesimals attaining masses sufficient to trigger gas accretion. For the warm and hot discs the mass increase is a few times to a few tens of times their initial mass. When migration effects are included, the final mass in the disc is at most ten times its initial mass depending on the disc temperature. This is because large planetesimals that formed earlier were continuously removed from the disc: when planetesimals reach a certain mass, the angular momentum exchange with the surrounding gas disc results in their inward migration towards the disc inner edge (Tanaka et al., 2002) and their eventual loss to the Sun. Migration is especially important in cold discs such that the maximum solid disc mass (assuming the same initial disc mass) is achieved when the initial gas disc temperature is 250 K rather than 200 K. Pebble fragmentation effects, when excluded, generally results in a higher final disc mass, roughly a few times higher compared to the case when fragmentation was included. The total solid mass in the disc by the end of the simulations for these massive discs are in fact higher than what is presented here for 0.5 au $< a <$ 2.0 au because planetesimals are scattered away from their initial location by their more massive counterparts. The planetesimal disc expanded into the region beyond 2.0 au and up to around 3.0 au in the case of cold discs (Fig. 2.4 which we discuss next). We chose to compute the final mass between 0.5 au and 2.0 au to be consistent with the computation for the less massive discs.

In Fig. 2.4 we plot, for a selected set of initial conditions, the distribution of solids within 3 au at the end of the simulations (t = 4 Myr). For the lower-mass discs ($M_{\mathrm{disc,i}} \leq 1 \times 10^{-3}\ M_{\mathrm{E}}$) that contain planetesimals with $D \lesssim$ 300 km, we show the results for the cases with both fragmentation and migration effects included. The results are similar for the cases with fragmentation and/or migration excluded, mainly because the planetesimals do not grow to sizes large enough to perturb the orbits of nearby planetesimals. Thus for these lower-mass discs, we can clearly see what is happening in the solid disc when the planetesimals are subjected to the pebble flux. There are several evident trends that we observe. First, planetesimals closer to the Sun are more efficient at accreting pebbles and growing larger. The trend of inside-out growth is due to the pebble accretion rate having a dependence on semi-major axis (Ida et al., 2016). This outcome can also be understood using a more physical explanation: planetesimals in the region closer to the Sun see a higher concentration of pebbles because the pebbles are confined to an increasingly narrow annulus when they drift inwards, which is effectively an increased surface density in the disc, and thus it is easier to accrete pebbles in this region. Second, planetesimals in a cold disc experience more growth than those in a hot disc. The dependence of planetesimal growth on the temperature of the disc can be traced to the disc temperature's effect on the pebble scale height. Pebbles in discs with a lower (higher) temperature have lower (higher) scale heights which allows them to be accreted more (less) efficiently onto planetesimals. Third, planetesimal growth is dependent on their size. We have shown in our analytical computation discussed previously in Section 2.2.4 that pebble accretion is only efficient for planetesimals with $D \gtrsim$ 300 km because of their larger accretion cross-section.

We show the results of $M_{\mathrm{disc,i}} = 0.1\ M_{\mathrm{E}}$ with fragmentation effects included (rows 3 and 4 of Fig. 2.4) as they are representative of the outcomes for the higher-mass disc ($M_{\mathrm{disc,i}} \geq 0.05\ M_{\mathrm{E}}$) simulations. Other than the difference in the amount of growth in the disc, there are no obvious differences in the mass versus semi-major axis distribution of solids in discs with $M_{\mathrm{disc,i}} = 0.05\ M_{\mathrm{E}}$ and $0.25\ M_{\mathrm{E}}$. Compared to the lower-mass discs, we do not see a clear inside-out growth trend for the higher-mass discs. This could be due to the discs containing much more larger planetesimals. These large planetesimals tend to grow faster due to their larger accretion cross-section (and higher accretion efficiency) thus perturbing the orbits of nearby planetesimals and scattering them to wider orbits. For example, planetesimals are scattered to 3 au and beyond in the case of a cold disc (with migration effects included) where planetesimal growth is more efficient. The difference between the simulations with migration effect included and those that do not is most obviously seen for a cold disc. With migration included, the most massive planetesimals in the disc is less than 1 M_{E}. This is because planetesimals that grew to large sizes earlier migrated towards the Sun and were removed from the simulation (Fig. 2.5). With migration excluded, planetesimals in a cold disc can reach masses on the order of 100 M_{E}, indicating that their core masses have crossed the threshold for gas envelope accretion to occur. The strong gravitational perturbation of a gas giant also scatters away most of the mass in the disc, leaving only a narrow annulus between 0.5 au and 1 au that will be cleared out in due time.

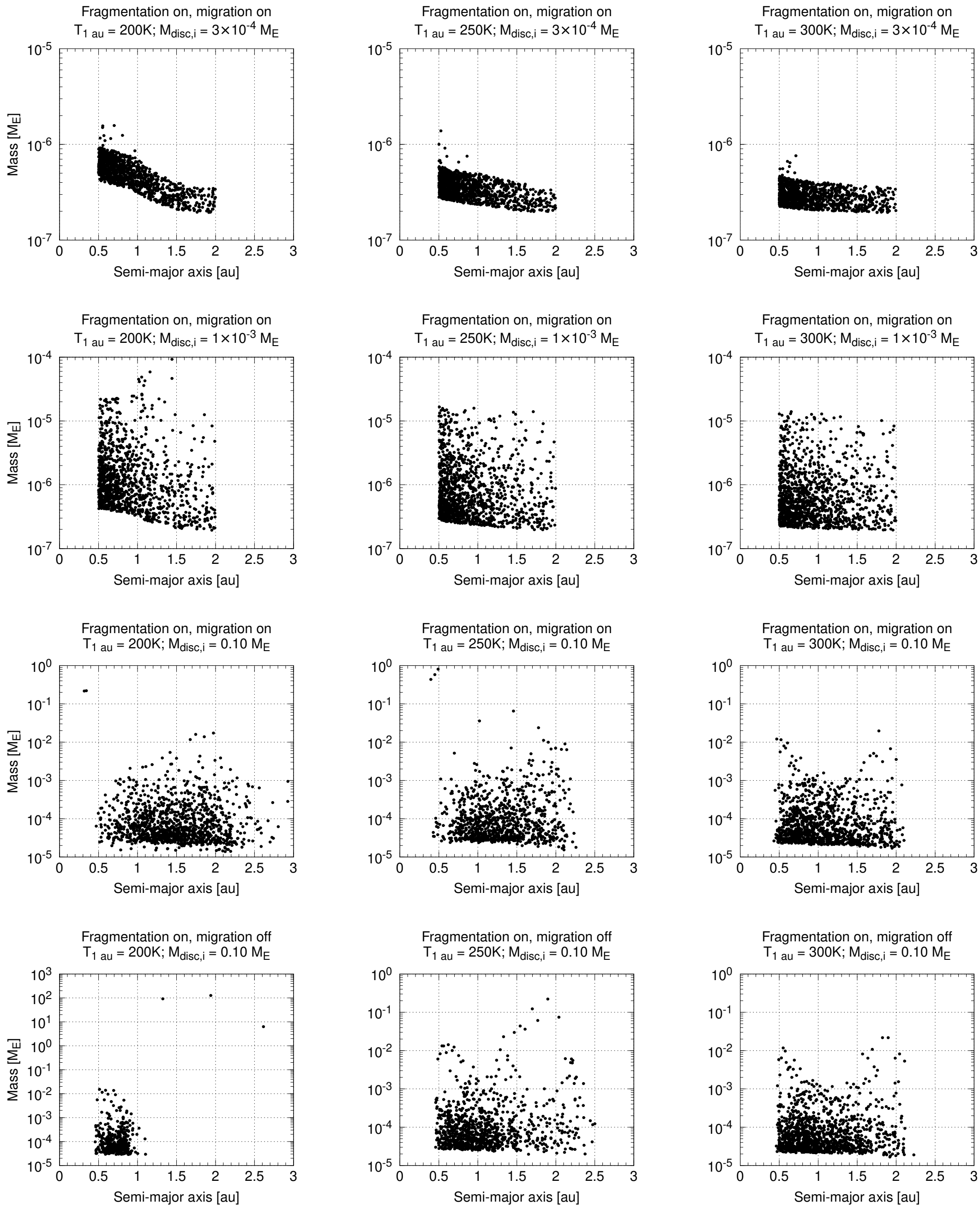

FIGURE 2.4: Distribution of mass in the inner disc at the end of the simulations. Shown here are plots for selected initial conditions representative of all possible outcomes.

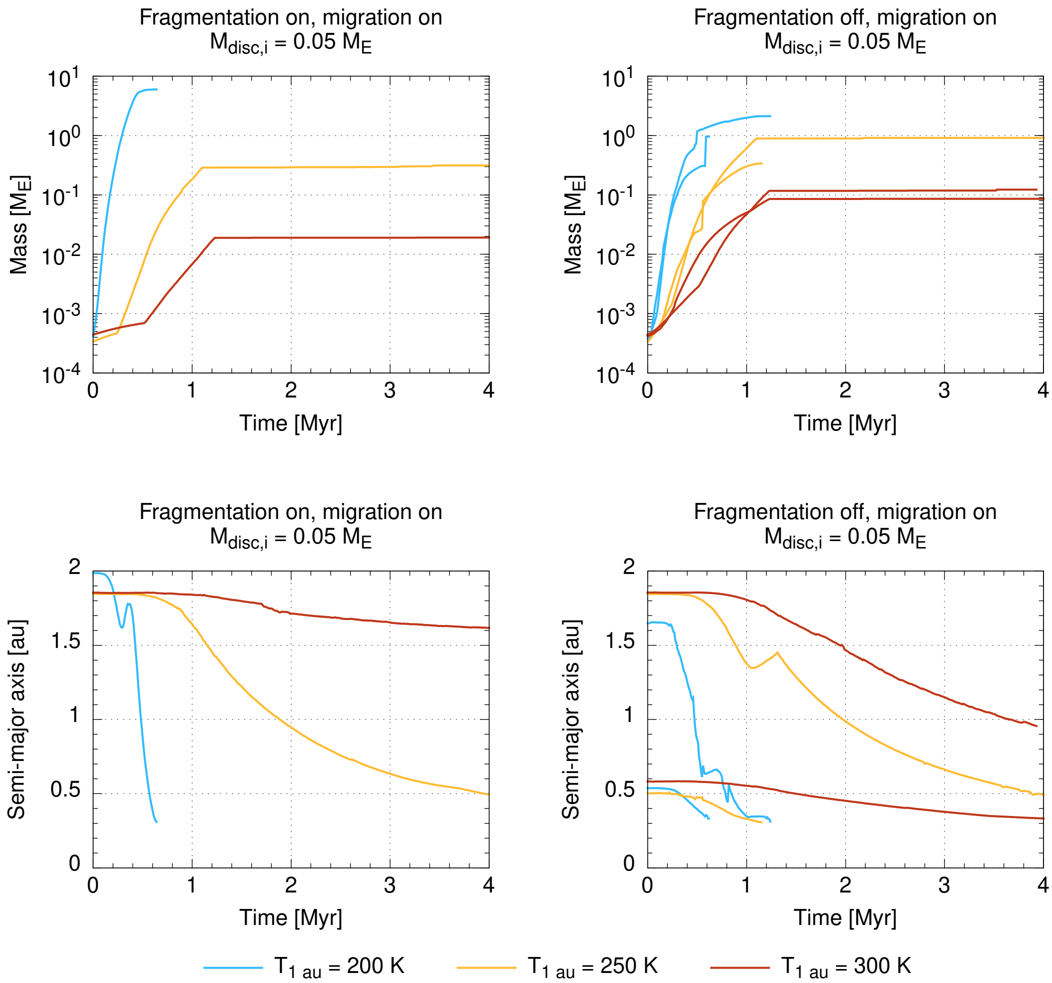

FIGURE 2.5: Selected growth curves of planetesimals in discs of the same mass but with different initial temperature. These planetesimals have diameter over 1000 km so they experience growth more quickly due to their higher pebble accretion efficiency. As migration effects are included in these simulations, these planetesimals will interact with the surrounding gas and migrate inwards to the Sun when they become sufficiently massive. In some cases, these planetesimals do not survive until the end of the simulations (e.g., truncated blue curves in the left and right panels). If we assume that the pebbles do not fragment at the snow line (right panels), then planetesimals near to the inner edge of the solid disc can also grow quickly because of the increased surface density of pebbles in the region closer to the Sun.

2.4.2 Establishing a gradient in mass: Lower-mass discs

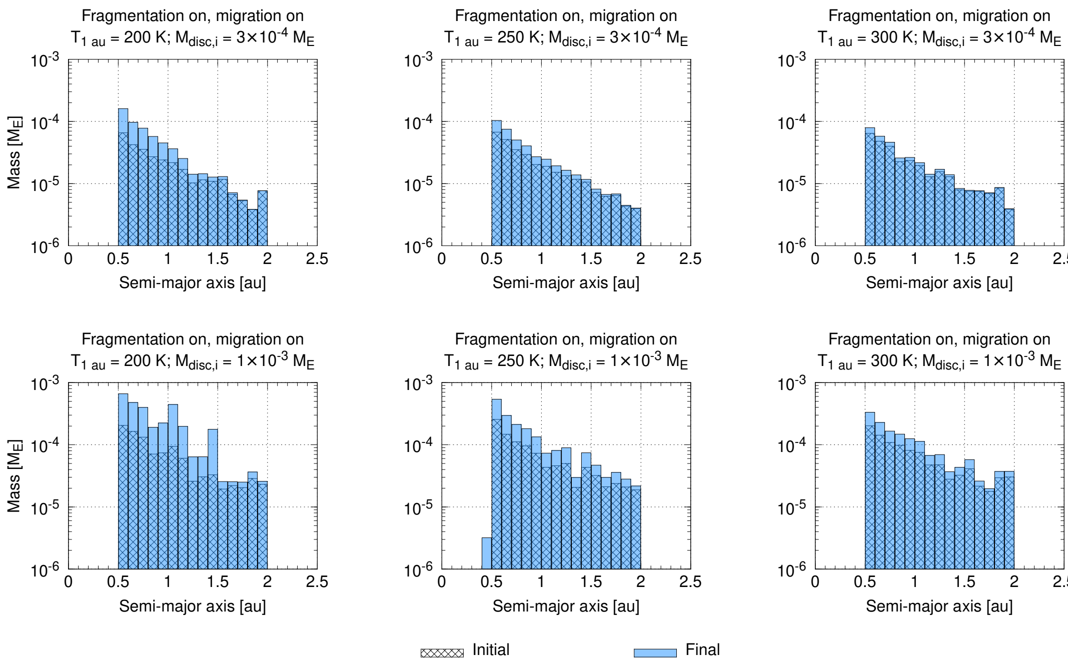

FIGURE 2.6: Initial and final mass distribution in each section of the disc. Shown here are the results for discs containing small planetesimals ($M_{\rm disc,i} = 3{\times}10^{-4}\ M_{\rm E}$ and $1{\times}10^{-3}\ M_{\rm E}$) at different initial temperatures, with both fragmentation and migration effects included.

In this and the following subsection we will take an even closer look at the mass distribution in the disc to determine how much mass is accreted in each section of the disc. We divided the inner disc into bins of size 0.1 au each and computed the initial and final mass in each bin. The results for discs containing small planetesimals with $D \lesssim 300$ km and the inclusion of fragmentation and migration effects (corresponding to the top-left panel of Fig. 2.3) are shown in Fig. 2.6. We observe a trend of inside-out growth: planetesimals closer to the Sun accrete, on average, more mass than those in the region further away (see also the top two rows of Fig. 2.4). The amount of mass accreted also has a dependence on the initial disc mass and the disc temperature, as discussed in the previous subsection. The same inside-out growth trend is also observed for the other simulations using the same initial disc masses with migration effects excluded and thus we opted to not show them. We do not show the results for the simulations with fragmentation effects excluded because the growth is insignificant.

We also computed the value of $M_{\rm disc,f} - M_{\rm disc,i}$ in each bin with the results shown in Fig. 2.7. In this plot we clearly see the semi-major axis dependence of the amount of mass accreted by the planetesimals. Therefore, if the solid disc is composed of planetesimals with $D \lesssim 300$ km and the disc is not disturbed by mergers and migration, its isotopic composition will naturally show a gradient.

2.4.3 Establishing a gradient in mass: Higher-mass discs

For the case of more massive discs (with $M_{\rm disc,i} \geq 0.05\ M_{\rm E}$), which are composed of larger planetesimals, the inside-out growth trend is not as clear. In Fig. 2.8, we observe a bump each around 1.5 au and inwards of 0.5 au for simulations with fragmentation and migration effects included. The bump around 1.5 au is the result of planetesimal growth caused by the inward migration of the snow line while the bump at $a < 0.5$ au is due to disc-induced migration

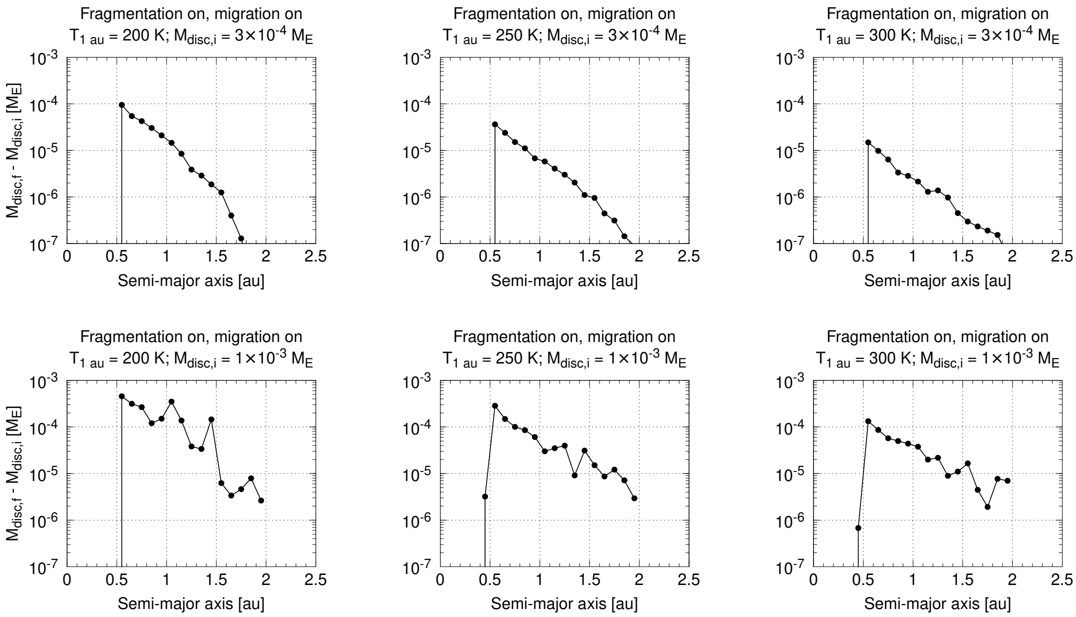

FIGURE 2.7: Mass increase ($M_{\mathrm{disc,f}} - M_{\mathrm{disc,i}}$) in each section of the disc. Shown here are the results for discs containing small planetesimals ($M_{\mathrm{disc,i}} = 3 \times 10^{-4}\ M_{\mathrm{E}}$ and $1 \times 10^{-3}\ M_{\mathrm{E}}$) at different initial temperatures, with both fragmentation and migration effects included.

effects causing massive bodies from farther away to migrate inwards and pile up near the disc's inner edge. In addition, because the planetesimals in these discs are more massive, they will have a higher pebble accretion efficiency which can accelerate their growth and thus enable them to perturb nearby smaller planetesimals. In the cold and warm discs where the environment is more conducive for planetesimal growth, we observe a wider spread in the distribution of mass in the disc due to large planetesimals scattering their nearby smaller counterparts away.

Unsurprisingly, we also do not observe a strong mass gradient in Fig. 2.9. Only in a few cases do we observe the trend but it is confined to the region within 1 au as in the case for warm discs or within 1.2 au as in the case of hot discs. This result is in contrast to the smoother slopes observed for the simulations using discs composed of smaller planetesimals (cf. Fig. 2.7); increasing the number of planetesimals in the more massive discs by including smaller bodies will not change the outcome, because the total mass growth is dominated by accretion onto the most massive bodies. The combined effect of high accretion efficiency and inward migration of large planetesimals in these discs dilute the mass gradient. In the case where migration effects are excluded, we observe spikes only in the region around and beyond 1.5 au and a mass gradient in the inner region from 0.5 au to about 1.2 au (Fig. 2.10). Because the planetesimals remained on their orbits while they grow in the simulations without migration, several prominent spikes can be seen in the region beyond 1.5 au for cold discs due the presence of gas giants. The outcomes for the warm and hot discs in the case without migration do not show obvious differences when compared to the outcomes with migration included because the higher gas temperature slows down pebble accretion and gas giant formation is more difficult.

We have seen in Fig. 2.3 that excluding the effects of fragmentation, i.e., allowing the pebbles to retain their size and mass when crossing the snow line into the inner regions of the disc, results in a general increase in the total mass of the discs. Compared to the case when fragmentation effects are implemented, the amount of mass increase is higher regardless of the disc temperatures and whether migration effects are included. In Fig. 2.11 we observe a distinct peak in the region within 0.5 au across all disc temperatures because of the inward migration of large planetesimals. There is no obvious gradient between 0.5 and 1.2 au, the inside-out growth trend is completely masked by the concentration of large bodies in the inner region of the disc. When both fragmentation and migration effects are excluded, the trend of inside-out growth became apparent once again, in addition to the spikes and peaks beyond 1.5 au and the overall larger mass increase in the whole disc (Fig. 2.12).

In this and the previous subsection, we show that pebble accretion can generate a mass gradient in the terrestrial planet region. This mass gradient does not, however, necessarily translate into a corresponding gradient in composition. A composition gradient is feasible only if the total mass added by pebbles does not exceed the original mass of the planetesimal disc, otherwise the composition of the disc becomes almost uniform and dominated by the composition of the pebbles.

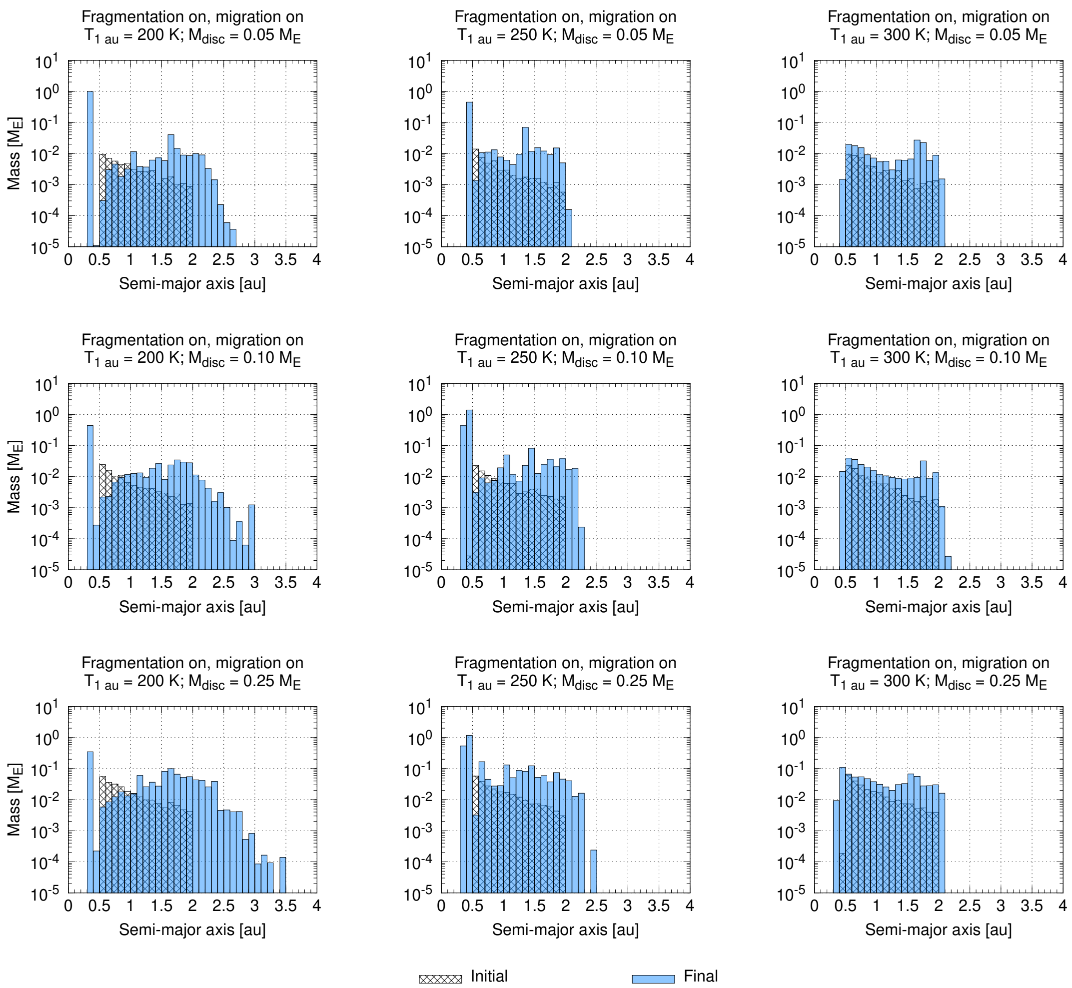

FIGURE 2.8: Initial and final mass distribution in each section of the disc. Shown here are the results for more massive discs containing large planetesimals ($M_{\mathrm{disc,i}} = 0.05\ M_{\mathrm{E}},\ 0.10\ M_{\mathrm{E}}$, and $0.05\ M_{\mathrm{E}}$) at different initial temperatures, with both fragmentation and migration effects included.

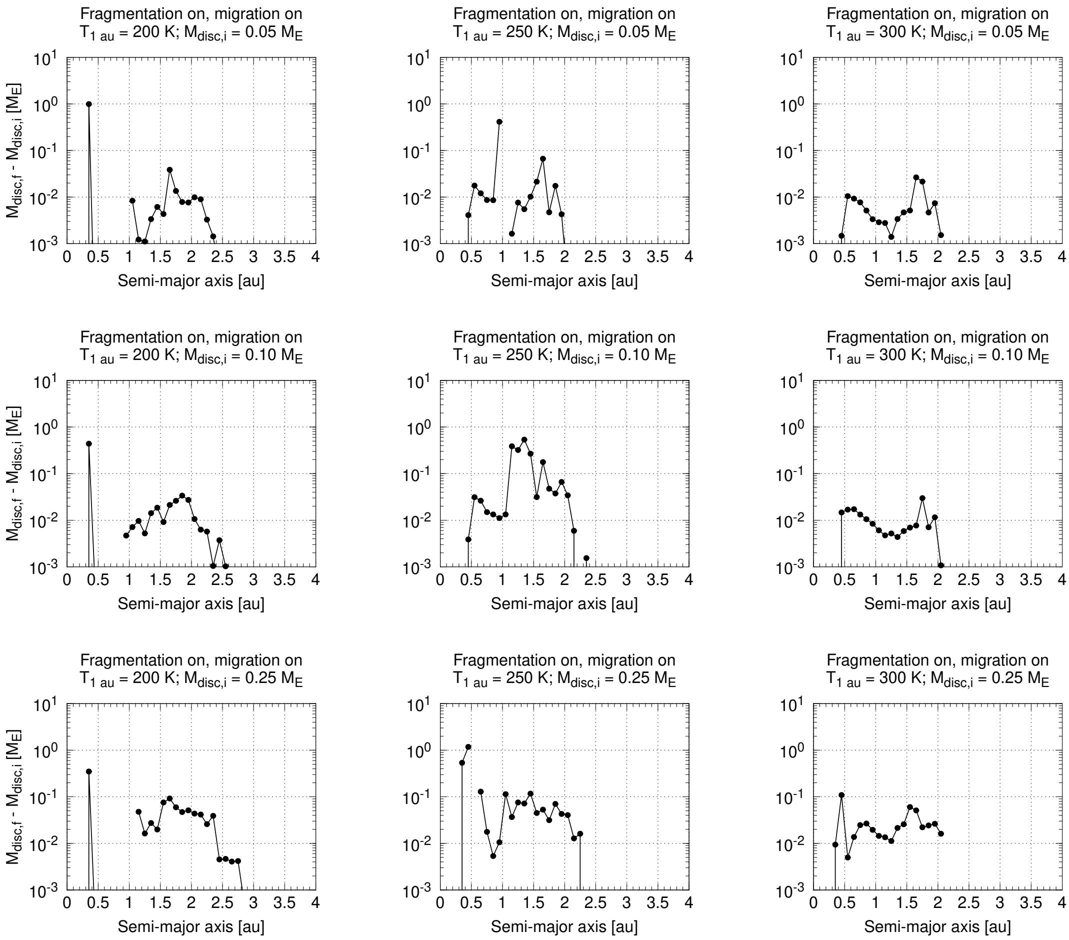

FIGURE 2.9: Mass increase ($M_{\mathrm{disc,f}} - M_{\mathrm{disc,i}}$) in each section of the disc. Shown here are the results for more massive discs containing large planetesimals ($M_{\mathrm{disc,i}} = 0.05\ M_{\mathrm{E}},\ 0.10\ M_{\mathrm{E}}$, and $0.05\ M_{\mathrm{E}}$) at different initial temperatures, with both fragmentation and migration effects included.

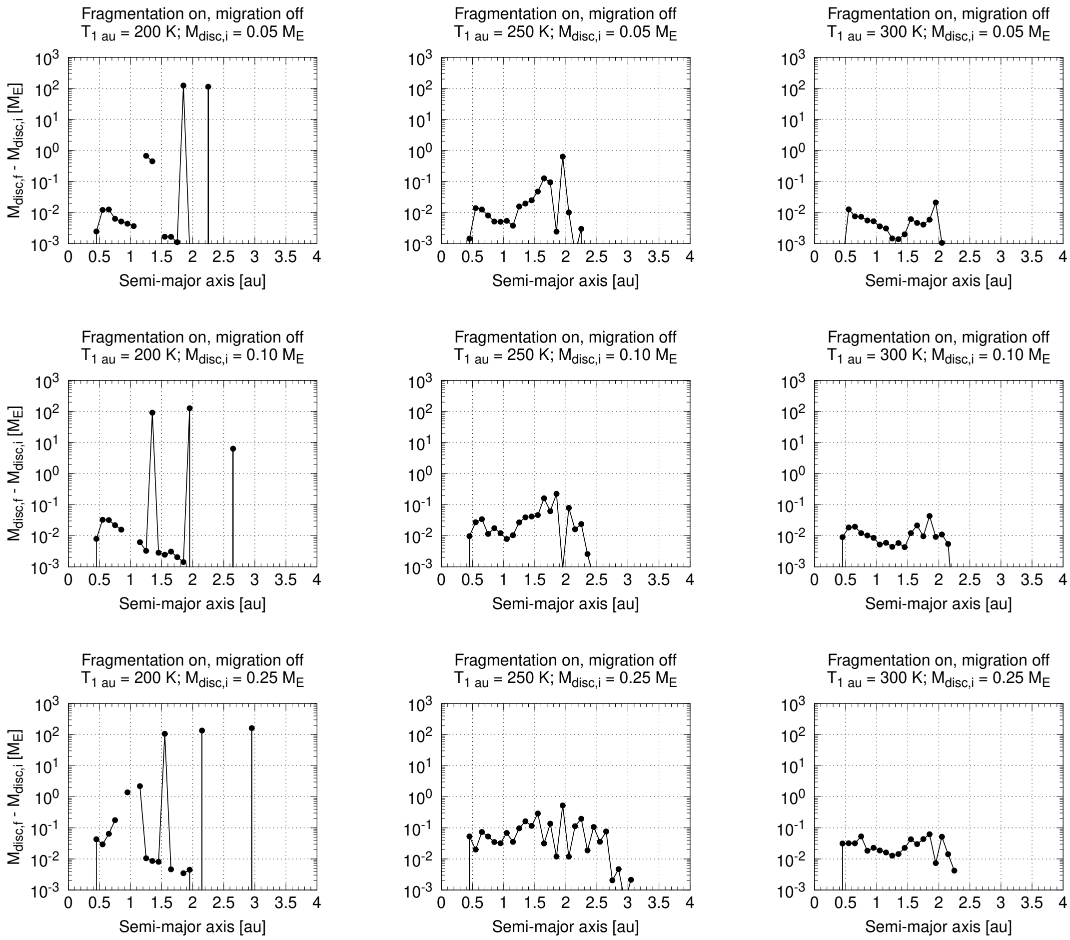

FIGURE 2.10: Mass increase ($M_{\mathrm{disc,f}} - M_{\mathrm{disc,i}}$) in each section of the disc. Shown here are the results for more massive discs containing large planetesimals ($M_{\mathrm{disc,i}} = 0.05\ M_{\mathrm{E}},\ 0.10\ M_{\mathrm{E}}$, and $0.05\ M_{\mathrm{E}}$) at different initial temperatures, with fragmentation effects included but migration effects excluded.

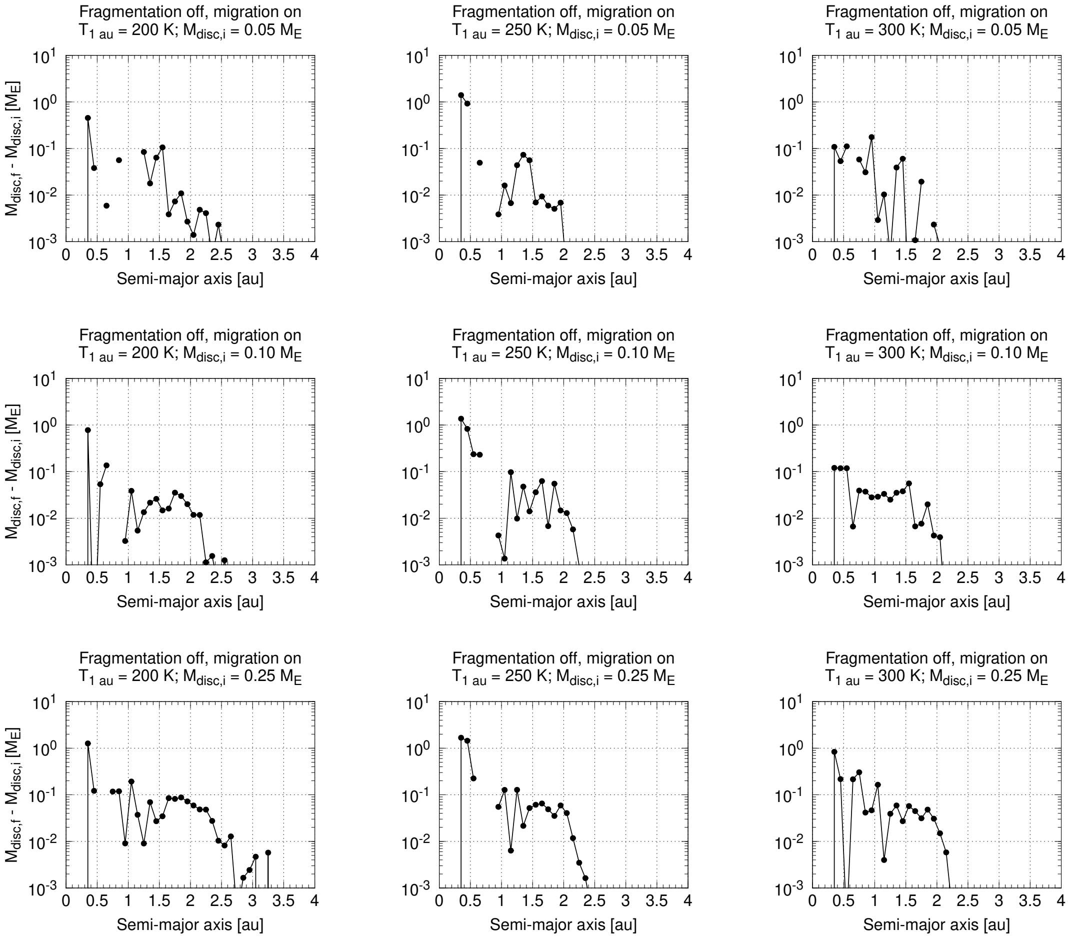

FIGURE 2.11: Mass increase ($M_{\mathrm{disc,f}} - M_{\mathrm{disc,i}}$) in each section of the disc. Shown here are the results for more massive discs containing large planetesimals ($M_{\mathrm{disc,i}} = 0.05\ M_{\mathrm{E}}$, $0.10\ M_{\mathrm{E}}$, and $0.05\ M_{\mathrm{E}}$) at different initial temperatures, with fragmentation effects excluded but migration effects included.

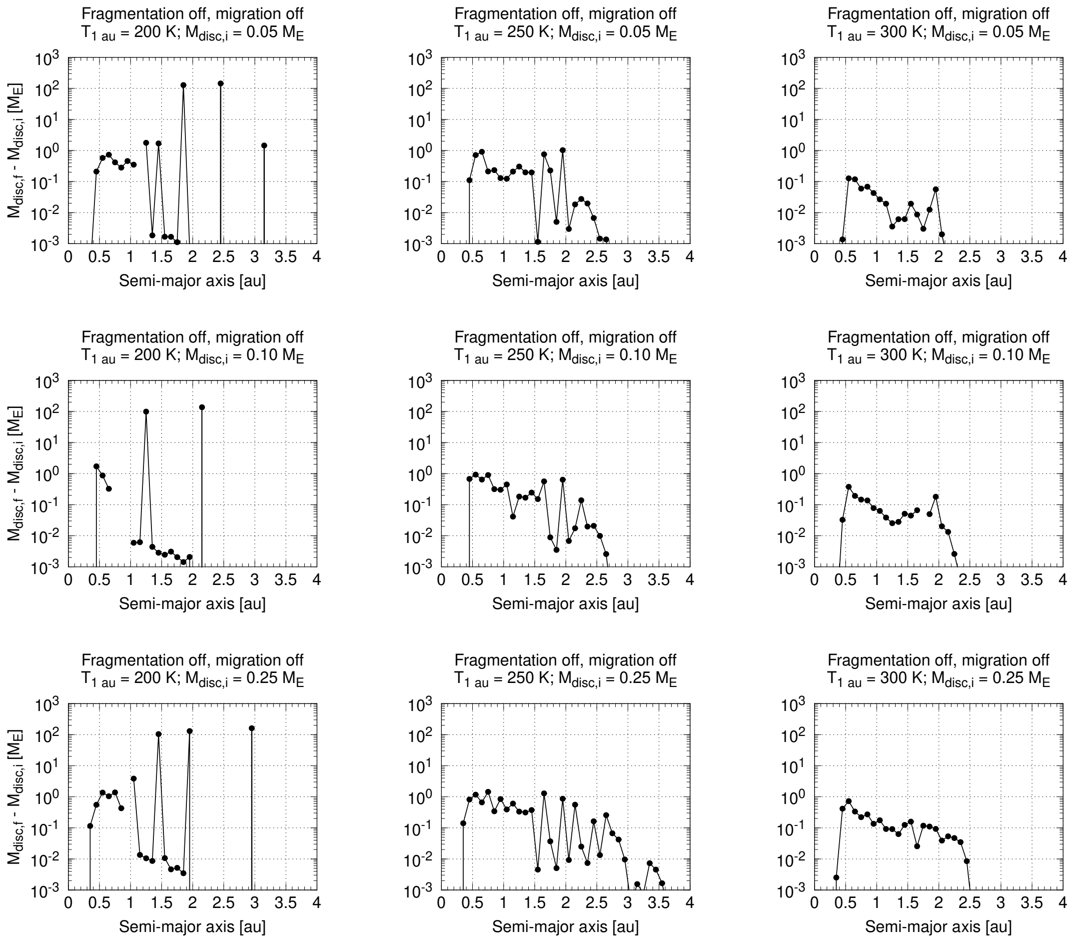

FIGURE 2.12: Mass increase ($M_{\mathrm{disc,f}} - M_{\mathrm{disc,i}}$) in each section of the disc. Shown here are the results for more massive discs containing large planetesimals ($M_{\mathrm{disc,i}} = 0.05\ M_{\mathrm{E}},\ 0.10\ M_{\mathrm{E}}$, and $0.05\ M_{\mathrm{E}}$) at different initial temperatures, with both fragmentation and migration effects excluded.

2.5 Discussion

2.5.1 Jupiter's capacity as a pebble barrier

From the observed isotopic dichotomy among iron meteorites and chondrites that sample the inner and outer Solar System, it is thought that the two reservoirs should have been separated very early and remain separated for at least a few Myr (Kruijer et al., 2017). The means to sustain the separation of the inner and outer Solar System has been suggested to be the growth of Jupiter (e.g., Kruijer et al., 2017). The results of a study by Brasser and Mojzsis (2020) showing large amounts of pebbles could flow past Jupiter while it is still growing and contribute to the growth of planetesimals in the inner Solar System depending on the size of the planetesimal and the temperature of the gas disc raise doubts on the capacity of Jupiter as a pebble barrier.

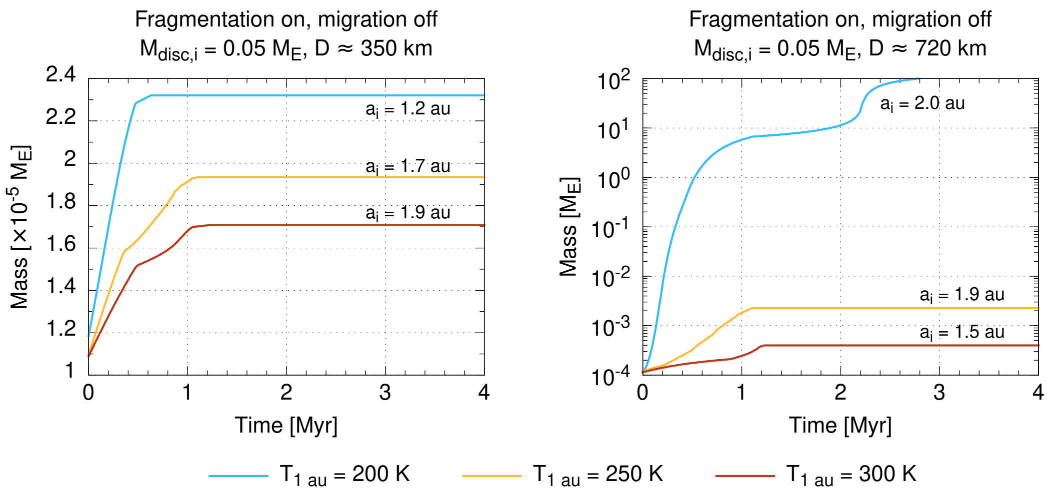

FIGURE 2.13: Growth curves of selected planetesimals of different initial size located beyond 1.2 au over the total simulation time of 4 Myr taken from simulations using the same initial disc mass of $M_{\rm disc,i} = 0.05\ M_{\rm E}$ but at different disc temperatures. These examples illustrate the substantial mass increase contributed by pebbles (and gas in the case of cold discs) despite Jupiter shutting off the pebble flux when it reaches its isolation mass.

We obtain outcomes similar to those of Brasser and Mojzsis (2020) in that that planetesimals with $D > 300$ km in the region around Mars' orbit can grow substantially after the passage of the snow line under special conditions when Jupiter is growing. Planetesimals in this region can grow to large sizes by mergers and, in some cases, gas accretion, thereby contributing to most of the mass in the disc. In Fig. 2.13 we illustrate this point using growth curves of selected planetesimals of different sizes initially located beyond 1.2 au in discs of different temperature. Our selected 350 km planetesimal in a cold disc increased its mass by 90% while a 720 km planetesimal in the same simulation attained sufficient mass to accrete gas. The swift growth of the larger planetesimal is due to its size and its semi-major axis. Located in the outer edge of the solid disc, it is one of the first few planetesimals to encounter the pebble flux. In a hot disc where the pebble accretion efficiency is lower and the snow line is located farther away, our selected 350 km planetesimal nevertheless managed to increase its mass by 50% from pebbles while its 700 km counterpart increased its mass by about 400%.

Despite Jupiter effectively shutting off the pebble flux once it reaches its pebble isolation mass, we find that planetesimals of 300 km and above have accreted a rather large amount of pebbles during this time which could potentially alter their initial isotopic composition. If the inner Solar System contained a high number of planetesimals with diameter

300 km and above, then the substantial contribution by pebbles can result in the inner Solar System's final isotopic composition after 4 Myr to be akin to that of the outer Solar System, thus diminishing the isotopic differences between these two reservoirs. In this sense, previous studies suggesting that Jupiter acts as an efficient gatekeeper in preventing pebbles from flowing past its orbit towards the inner disc and maintaining the isotopic dichotomy of the early Solar System (e.g., Kruijer et al., 2017) may need to be revisited. It is therefore more likely the case that some other factor(s) is/are at play at preserving the isotopic dichotomy, e.g., a structural gap in the protoplanetary disc located just within the orbit of Jupiter, proposed by Brasser and Mojzsis (2020).

2.5.2 Comparing dynamical outcomes with cosmochemistry data

From chondritic mixing models discussed in Chapter 1, a mass contribution from outer Solar System material by amounts greater than $\sim 10\%$ poses problems for reconciling the difference in isotopic composition of the terrestrial planets with that of the outer Solar System, and a mass increase beyond 100% will severely dilute the original composition of the inner disc and mostly homogenise it. Discs with initial mass of $\geq 0.05\ M_{\mathrm{E}}$ and containing many planetesimals larger than 300 km in diameter increase their mass by at least a few times the initial value, suggesting that their initial isotopic signatures will be replaced by the isotopic composition of outer Solar System material. If we take 10% as the upper limit for the amount of outer Solar System material present in the Earth and Mars, then the successful cases from our numerical simulations are the cases which fulfil all of the following criteria:

- $M_{\mathrm{disc,i}} \leq 1 \times 10^{-3}\ M_{\mathrm{E}}$, or if the disc is more massive then all planetesimals have $D \leq$ 300 km, and
- $T_{1\ \mathrm{au}} \geq 250$ K, and
- pebble fragmentation effects at the snow line are unimportant.

For these cases the overall mass increase in the disc ranges from 0.3% to 5%, consistent with the constraint from mixing models and cosmochemistry data. However, these cases have a critical shortcoming: although the amount of mass increase in the disc appears consistent with cosmochemistry data, the total mass in the disc at the end of 4 Myr is actually too little to build the terrestrial planets in the next stage of planet formation. A 5% mass increase for a disc with $M_{\mathrm{disc,i}} = 1 \times 10^{-3}\ M_{\mathrm{E}}$ is a mere $1.05 \times 10^{-3}\ M_{\mathrm{E}}$; at least 2 M_{E} of solids is required in the disc to form the terrestrial planets. To fulfil both requirements for the amount of mass increase ($\lesssim 10\%$) and disc mass at the end of the pebble accretion phase ($\gtrsim 2\ M_{\mathrm{E}}$), we should ideally start with a solid disc of $M_{\mathrm{disc,i}} = 1.8\ M_{\mathrm{E}}$ which will grow to 2 M_{E} assuming a 10% mass increase and that the disc contained planetesimals of size $D \leq 300$ km. However, modelling such a massive disc made up entirely of small planetesimals is at the limit of the capabilities of current hardware and *N*-body codes (Woo et al., 2021). We will therefore reserve this study for future work.

It could still be possible for the dynamical outcomes to be reconciled with cosmochemistry data (e.g., in ε^{48}Ca) by invoking specific assumptions, such as the inner disc planetesimals had a ureilite-like initial composition and the pebbles an isotopic composition akin to CI chondrites (Schiller et al., 2018). That study argues that the gradual accretion of CI-chondrite-like material from the outer Solar System over the lifetime of the gas disc (about 5 Myr) can explain the variation in ε^{48}Ca with mass of the major differentiated bodies in the inner Solar System (Vesta, angrite parent body, Mars and Earth). When the gas disc dissipates, the isotopic composition of the planetesimals and planetary embryos stopped changing, with the largest embryos (including proto-Earth) having up to 40% of their mass contributed from the outer Solar System (Schiller et al., 2020). Indeed, by looking at single isotopes independently it is always possible to find a combination of end-member meteoritic reservoirs with the correct mixing proportion to explain the isotopic composition of a planetary body. The difficulty is to find a single mixing ratio that matches all isotopes simultaneously.

Schiller et al. (2018) and Schiller et al. (2020) argue for pebble accretion in the inner Solar System based on ε^{48}Ca and ε^{54}Fe isotopes in the Earth and other meteorites. Their combined results argue for the Earth having 40% CI-chondrite-like material in its mantle. For the ureilite parent body Schiller et al. (2018) list $\varepsilon^{48}\mathrm{Ca} = -1.46 \pm 0.46$ and for the CI chondrite parent body $\varepsilon^{48}\mathrm{Ca} = 2.06 \pm 0.085$. If we denote by x the fraction of CI chondrite in Earth's mantle, then according to Schiller et al. (2018) x is the solution to $2.06x - 1.46(1-x) = 0$, which yields $x = 0.41 \pm 0.12$ (2σ). The uncertainties were computed using a Monte Carlo method. If these results are correct, they should also hold for the isotopes of other elements commonly used as tracers, such as oxygen, chromium and titanium because the Earth can only be made up of a single mixture of sources rather than different mixtures for different elements. For the ureilite parent body $\Delta^{17}\mathrm{O} = -1.16 \pm 0.55$ (Clayton and Mayeda, 1996) and $\Delta^{17}\mathrm{O} = 0.39 \pm 0.14$ for the CI chondrites (Clayton and Mayeda, 1996). The required mass fraction of CI chondrite based on oxygen isotopes is $x = 0.75 \pm 0.23$ (2σ). This fraction is, however, grossly inconsistent with that advocated by Schiller et al. (2018) based on calcium isotopes. In addition, if molybdenum isotopes are considered then there is no acceptable solution for x as the isotopic anomalies in ε^{92}Mo for both ureilites and CI chondrites have the same sign. We arrive at the same conclusion as well if we were to consider the more abundant isotopes of molybdenum ($\varepsilon^{94,95}$Mo).

The above analysis shows that it is difficult to establish whether or not pebble accretion occurred in the inner Solar System when using isotopes alone because the end-member case Ureilite + CI chondrite can often be invoked as a mixture to explain the isotopic anomalies of the terrestrial planets (albeit not always in the same proportions). It is therefore necessary to look beyond nucleosynthetic isotopes alone to establish whether the simple model suggested by Schiller et al. (2018, 2020) and pebble accretion can account for the growth and composition of the terrestrial planets. In the following, we examine the constraints from the major elemental abundances in known meteoritic reservoirs and planetary bodies.

It has been reported (e.g., Drake and Righter, 2002; Dauphas et al., 2015) that the combination of chondritic (and perhaps achondritic) meteorites is unable to reproduce the Mg/Si ratio of the terrestrial planets. Following Drake and Righter (2002) we plot in Fig. 2.14 the Mg/Si versus Al/Si elemental ratios for the terrestrial planets and the known meteorite parent body compositions. The CI chondrites are similar in elemental composition to the Sun's photosphere (e.g., Anders and Grevesse, 1989; Lodders, 2003) and there is little variation amongst the carbonaceous chondrites. The non-carbonaceous meteorites, which formed in the same reservoir as the Earth and Mars, all have lower Mg/Si ratios due to nebular and planetary processes (e.g., Larimer, 1979; Alexander, 2019); they all have more or less forsterite- or enstatite-rich composition (Dauphas et al., 2015).

The possible compositions of the bulk Silicate Earth (crust and mantle) computed from models based on terrestrial rocks and chondrites (e.g., McDonough and Sun, 1995; Palme and O'Neill, 2014) place it at an end-member location in Fig. 2.14, indicating that the chemical composition of the Earth is unlike any of the known meteorites. An exception is the result of Javoy et al. (2010) (blue square labelled with J10 in the figure) which is obtained by assuming that the Earth is made up entirely of enstatite chondrites. This result should however be interpreted with caution as a more recent study examining the δ^{30}Si and Mg/Si composition of the Earth showed that it is similar to the enstatite chondrites isotopically but not chemically (Dauphas et al., 2015).

There remains uncertainty in the composition of the Earth's lower mantle, which is challenging to determine but important in deriving accurate estimates of the bulk Silicate Earth's composition. Although the different bulk Silicate Earth models make different assumptions about the composition of the upper and lower mantle, they are all consistent with geochemistry (McDonough, 2016). The models of McDonough and Sun (1995) and Palme and O'Neill (2014) assume a homogeneous (pyrolitic with Mg/Si $\sim$ 1.3) composition for the whole mantle while the model of Javoy et al. (2010) requires that the upper and lower mantle differ in their compositions. Results from seismic tomography observations of subducted crustal slabs (Fukao and Obayashi, 2013), computations and measurements of mineral elasticities (Wang et al., 2015; Kurnosov et al., 2018) support a compositionally homogeneous mantle, although there are alternative proposals for a non-pyrolitic and silicon-enriched lower mantle based on its sound-velocity structure (Murakami et al., 2012; Mashino et al., 2020). Be that as it may, the Mg/Si ratios of the lower mantle derived from these studies ($\sim$ 1.0 for Murakami et al. 2012 and 1.14 for Mashino et al. 2020) still lie above the Mg/Si ratio of the known meteorites.

The amount of Si fractionated into the Earth's core is also uncertain, but it is estimated to be between 2 wt% to 7 wt% based on geochemical and geophysical constraints (e.g., Badro et al., 2007; Fitoussi et al., 2009; Moynier et al., 2020). We plot in Fig. 2.14 the corresponding Mg/Si and Al/Si ratios for the Earth assuming different amounts of Si in the core. The Earth's chemical composition is similar within uncertainties to the carbonaceous chondrites if more than 5 wt% of the Si is in the core. Nevertheless, this still does not change the fact that the Earth's chemical composition cannot be reproduced by any mixture of known planetary materials, not even the combination of ureilites and CI chondrites as suggested by Schiller et al. (2018, 2020) because this mixture would lower the Mg/Si ratio to below the 7 wt% Si value.

Will the outcome of the N-body simulations change by assuming a changing composition of the pebbles? In our study, we implicitly assume that the pebbles have the same composition, which we leave unspecified but one could assume any of the various carbonaceous chondrites as a proxy. In reality, the pebbles that formed at different times and at different locations in the disc could potentially have different compositions. The diversity in the isotopic compositions of the carbonaceous chondrites possibly reflects their distinct formation location and/or their formation time, although this is difficult to prove. For the isotopes of O, Cr and Ti the CI and CO chondrites plot in end-member positions of the CC group. This could mean that there was also a compositional gradient in the outer Solar System when these bodies formed. To model the effect of time-dependent pebble compositions, we need to understand how the compositional gradient scales with heliocentric distance. This information is currently unavailable, although Desch et al. (2018) suggested that the CI chondrites form farthest away from the Sun while CO chondrites form closest to the Sun, but this suggestion is based mostly on model predictions.

One possible way out of this impasse is to do a similar end-member study by estimating the contribution of CI or CO chondrites to the composition of the terrestrial planets using our isotope mixing models. We show in Fig. 2.15 (which is akin to Fig. 1.2) the computed best-fit composition of the Earth and Mars as a combination of enstatite chondrites, ordinary chondrites and CI or CO chondrites using the Monte Carlo mixing model algorithm described in Appendix A. With only CI or CO chondrites, the mixing model returns the maximum contribution of these chondrite types as $\leq$ 10%, similar to the results obtained by including various other types of carbonaceous chondrites (Fig. 1.2). For both planets the contribution from H-chondrites is most strongly affected by the choice of either CI or CO. Thus, even if we were to assume a time-dependent variation in the composition of the pebbles from CO-like at the beginning to CI-like at the end (or vice versa), it still remains difficult for our N-body simulation results to be reconciled with meteorite isotope and elemental ratio data of the inner planets: the amount of outer Solar System materials added to the terrestrial planets *cannot* be more than 10%!

Based on nucleosynthetic anomalies of several isotopes such as ^{50}Ti and ^{54}Cr, the contribution of carbonaceous chondrites towards the making of the Earth is limited to 10 – 25% (e.g., Warren, 2011; Mezger et al., 2020). We discussed the difficulty for O and Mo isotopes above. Taken together, the isotopic and elemental abundances as well as our modelling results argue against the isotopic gradient in the inner Solar System having been established through pebble accretion, and against pebble accretion having been a major source of planetary building blocks if the pebbles were sourced from the outer Solar System. For the gradient to have been established early either the injection of nebula material or thermal processing of molecular cloud material as suggested by some studies (Trinquier et al., 2009; Dwarkadas et al., 2017; Nanne et al., 2019; Ek et al., 2020) may be the generating mechanism(s), or it could be the case that the gradient is primordial and indigenous to the disc at the time of Solar System coalescence.

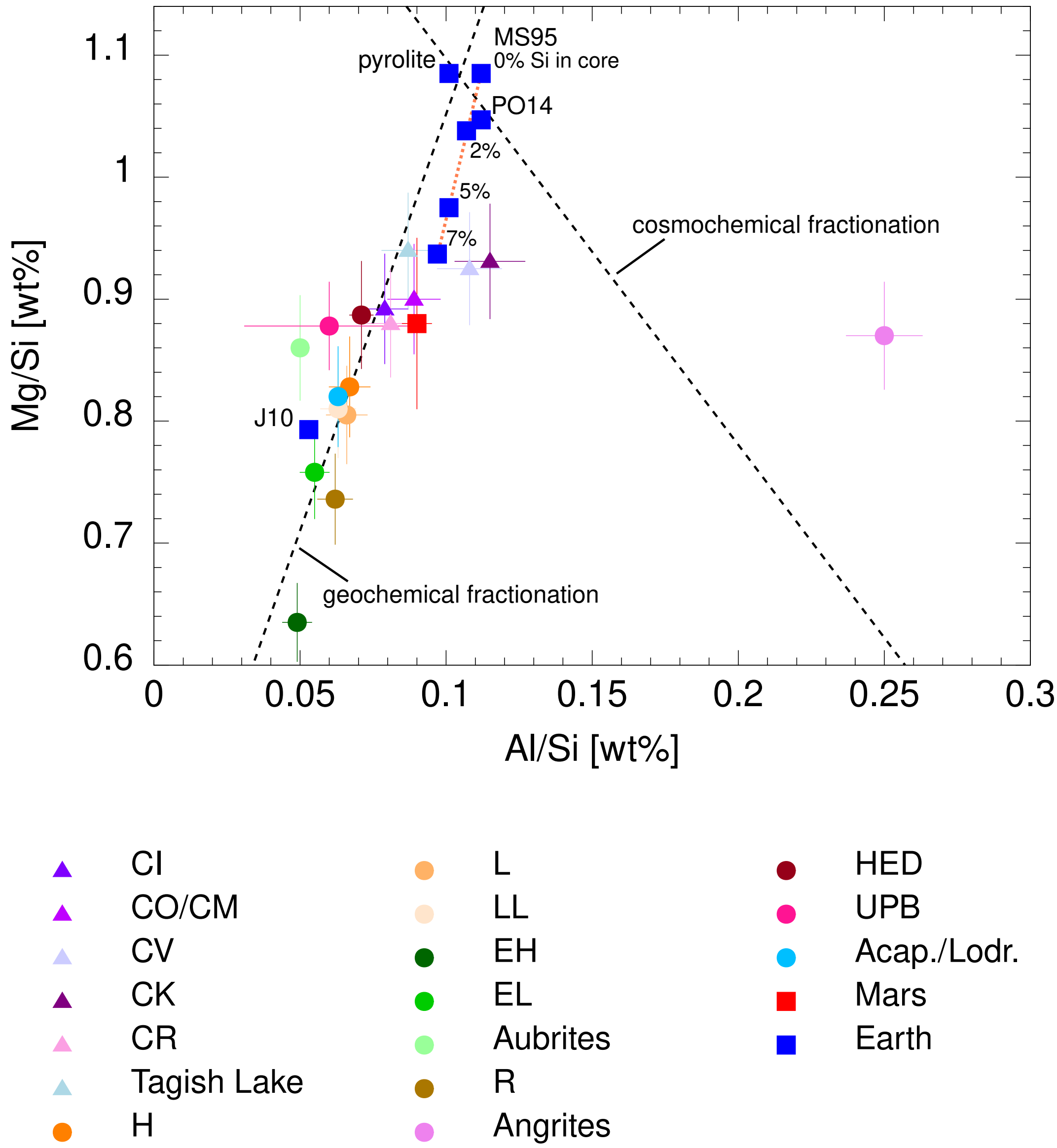

FIGURE 2.14: Mg/Si versus Al/Si for various chondrites, achondrites, Mars and the Earth. For the Earth, we also show the elemental abundance ratios of the Earth for different amount of Si in the core. The fractionation lines and pyrolite composition are from Jagoutz et al. (1979). Error bars are average variations for Mg/Si (5%) and Al/Si (10%) determinations for each parent body. UPB stands for ureilite parent body. Elemental abundance ratio for the Earth sourced from McDonough and Sun (1995), Javoy et al. (2010) and Palme and O'Neill (2014) while the data for meteorites are from Mason and Wiik (1962); Von Michaelis et al. (1968); Ahrens et al. (1973); Consolmagno and Drake (1977); Dreibus et al. (1977); Hertogen et al. (1977); Morgan et al. (1978); Jagoutz et al. (1979); Watters and Prinz (1979); Jarosewich et al. (1987); Wasson and Kallemeyn (1988); Jarosewich (1990); Kallemeyn et al. (1991, 1994, 1996); Kong et al. (1997); Mittlefehldt et al. (1998); Goodrich (1999); Longhi (1999); Brown et al. (2000); Wolf and Palme (2001); Greenwood et al. (2010); Bischoff et al. (2011); Stracke et al. (2012); Blinova et al. (2014); Hewins et al. (2014); Palme et al. (2014); Collinet and Grove (2020); Yoshizaki and McDonough (2020).

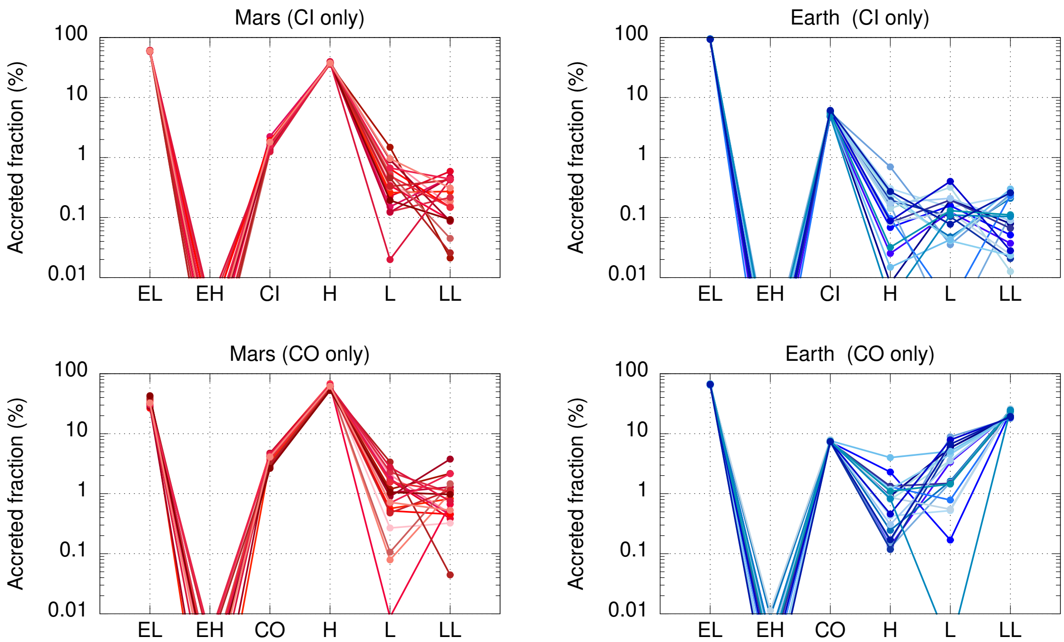

FIGURE 2.15: Best-fit contributions of enstatite chondrites, ordinary chondrites and CI or CO chondrites (end-members of the carbonaceous chondrite group for O, Cr and Ti isotopes) to the building blocks of Earth and Mars computed from 20 Monte Carlo mixing model simulations. The contribution of CI or CO chondrites to the Earth and Mars is limited to $\leq 10\%$.

2.6 Conclusions

The apparent correlation between semi-major axis and some nucleosynthetic isotope anomalies (ε^{48}Ca, ε^{50}Ti, ε^{54}Cr) for the Earth, Mars and Vesta can be used to constrain plausible dynamical mechanisms for planet formation in the inner Solar System. This correlation potentially points to the existence of isotopic gradients in the inner Solar System, for which the generating mechanism could possibly be the influx of material either from the outer disc or from the Solar nebula.

We investigated the role of the pebble accretion mechanism in the inner Solar System by performing *N*-body simulations modelling the growth of a disc of planetesimals subjected to a flux of pebbles originating from beyond the orbit of Jupiter. We found from simulation results that throughout the duration of Jupiter's growth from a 0.01 $M_{\rm E}$ planetary body to a ~ 300 $M_{\rm E}$ gas giant, depending on disc temperature and whether pebble fragmentation and/or disc-induced migration effects are considered, the final mass in the solid disc can be at least a few times its initial mass if it contained planetesimals of diameter $D \geq 300$ km; the final disc mass is at most 3 times the initial mass if the disc is made up of smaller planetesimals of diameter $D \leq 300$ km.

In particular, the amount of mass increase in warm and hot discs containing planetesimals less than 300 km in diameter is consistent with earlier studies (e.g., Dauphas, 2017) reporting that the Earth comprised of at most 10% of (CI) carbonaceous chondrites. However, the major drawback is that the growth of only a few per cent in mass cannot supply the inner disc with sufficient mass for the next stage of planet formation – planetesimal collision and mergers – to form larger bodies, unless the disc was more massive to begin with ($\gtrsim 1.5$ $M_{\rm E}$) and only consisted of very small planetesimals, which appears to contradict modern models of planetesimal formation. Indeed, the latest models of planetesimal formation show that they form with a fairly shallow size-frequency distribution, with diameters between 100 km to 1000 km (e.g., Chambers, 2010; Johansen et al., 2014; Klahr and Schreiber, 2020). Instead, if the inner disc had more mass it is expected to have contained many larger planetesimals ($D \geq 300$ km). In this case the mass increase of the disc due to pebble accretion becomes so large that the final isotopic composition of the planetesimals is akin to those of the (CI) carbonaceous chondrites, even with the assumption that the initial composition of the planetesimal disc was ureilite-like (Schiller et al., 2018).

Based on our results we conclude that pebble accretion played almost no role in the formation of the inner Solar System planetary bodies — the terrestrial planets and asteroid Vesta are more likely to have formed via the merging of planetesimals instead. Furthermore, the isotopic gradients in the inner Solar System were also unlikely to have been established over time by the accretion of outer Solar System material in the form of pebbles. The gradients could instead be (1) the outcome of accreting external material from the Solar nebula very early in the history of the Solar System (e.g., Dwarkadas et al., 2017; Nanne et al., 2019; Ek et al., 2020), (2) the outcome of thermally processed molecular cloud material (Trinquier et al., 2009), or (3) innate to the Solar System.

3 Formation of the inner Solar System bodies

3.1 Introduction

In the previous chapter we showed using cosmochemical trends and N-body simulations that the isotopic gradients in the inner disc were more likely to have been established via mechanisms like the accretion of nebular material or thermal processing in the disc, rather than the accretion of outer disc material in the form of cm-sized pebbles. Since the contribution of the pebble accretion mechanism to the growth of planetesimals in the inner disc is very minor, it should thus be more likely the case that the terrestrial planets (and possibly the larger asteroids) are products of collisional mergers among the inner disc planetesimals instead. Furthermore, when the planetary bodies in the inner disc were growing, the isotopic gradients should have remained unperturbed as is reflected in their correlated bulk isotopic compositions and semi-major axes (Yamakawa et al., 2010).

What, then, is the preferred formation pathway of the planetary bodies in the inner disc? Previous works that studied the Grand Tack (Walsh et al., 2011) and classical (Chambers, 2001) models to determine the feeding zones of the terrestrial planets found that the terrestrial planet feeding zones are very similar – wide with a large overlapping region – for the Grand Tack model (Brasser et al., 2017; Woo et al., 2018) whereas they are more localised and display a weak but nevertheless existent correlation with semi-major axis for the classical model (e.g., Raymond et al., 2004; O'Brien et al., 2006; Fisher and Ciesla, 2014; Kaib and Cowan, 2015; Woo et al., 2018). These results are verified with new, high-resolution GPU simulations (Woo et al., 2021). Given that the isotopic gradients are present in the inner disc during the formation of the inner Solar System bodies, the distinct isotopic compositions of Earth, Mars and Vesta therefore points to a classical-model-like formation pathway for these planetary bodies.

The major difference between the Grand Tack model and the classical model is that the former features an early gas-driven migration of Jupiter and Saturn while the latter does not. It turns out that this feature exerts a strong influence on the feeding zone outcomes. The migration of the gas giants causes the material in the inner disc to mix and thus homogenising any pre-existing isotopic differences (Carlson et al., 2018). It is therefore not surprising that the terrestrial planets that formed within the framework of the Grand Tack model have very similar feeding zones and isotopic compositions because they all accreted from the same homogenised mixture. If the gas giants did not migrate into the terrestrial region when the terrestrial planets were forming, as in the classical model, then it is more likely for the terrestrial planets to be isotopically distinct. However, the widely-known downside of the classical model is that its Mars analogues are systematically a few times too massive to be consistent with the current Mars unless the surface density slope is much steeper (Izidoro et al., 2015). We therefore need to seek out other dynamical models that can reproduce Mars with the correct mass without invoking the migration of the gas giants.

Here, we investigate the predictions of the depleted disc model (Izidoro et al., 2014) – a less-explored but promising model – for the isotopic compositions of the terrestrial planets. This model was proposed as an alternative to the Grand Tack model to emulate the orbital configuration of the terrestrial planets and the Earth-Mars mass ratio without the migration of Jupiter and Saturn. It features a depletion in the mass of the inner disc around and beyond the orbit of Mars, with the surface density of solids following a steep power law function of distance from the Sun (e.g., $\Sigma_s \propto r^{-5.5}$; Izidoro et al., 2015). We perform numerical simulations to study the formation of the terrestrial planets in this model and compute their corresponding feeding zones. We then determine the formation location of Vesta and compare the outcome with the results from the Grand Tack and classical models. Our aim is to find out whether the isotopic differences measured for the Earth, Mars and Vesta can be a natural consequence of this model.

The results for the feeding zones of the terrestrial planets have been published in Mah and Brasser (2021) while the results for the origin of Vesta is under preparation for submission to a peer-reviewed journal.

3.2 Methodology

We begin by simulating the formation of the terrestrial planets in the framework of the depleted disc model starting from a disc of planetary embryos (also known as protoplanets) and planetesimals with various reasonable initial conditions and studying the dynamical properties of the resultant planetary systems. Armed with the simulation outputs, we then proceed to identify terrestrial planet analogues – Venus, Earth and Mars – and compute their feeding zones.

Next, we identify the asteroid analogues – Hungaria, Vesta and Hebe – and work out their formation location. We also delve into our *N*-body simulation database to select asteroid analogues from the Grand Tack (Walsh et al., 2011) and classical (Chambers, 2001) models and carry out the same analysis as we did for the depleted disc model.

Finally, we compare the results for the terrestrial planets' feeding zones and the formation location of asteroids across all three dynamical models.

3.2.1 Initial conditions of depleted disc model *N*-body simulations

Our initial setup consists of a sequence of planetary embryos embedded in a disc of planetesimals (collectively referred to as solids). We set the inner edge of the solid disc to be at 0.5 au and the outer edge at 3.0 au. The free parameters are (1) the semi-major axis beyond where the mass is depleted r_{dep}, and (2) the scale or amount of mass depletion. We tested for three values of r_{dep}: 1.0 au, 1.25 au and 1.5 au, and three values for the scale of mass depletion: 50%, 75% and 95%. This gives us a total of nine sets of initial conditions (Fig. 3.1).

We followed the method of Brasser et al. (2016) to generate the distribution of embryos and planetesimals, assuming that the embryos have undergone oligarchic growth (Kokubo and Ida, 1998). Our method employs the semi-analytical oligarchic approach of Chambers (2006). In the following paragraphs, we provide a brief description of how we generated the initial mass-semi-major axis distribution of the solids in the disc.

As the first step, we computed the total mass in solids between 0.5 au and 3.0 au. We assumed a minimum-mass solar nebula (MMSN) solid surface density of $\Sigma_s = 7.1\ \text{g cm}^{-2}\ (r/1\ \text{au})^{-3/2}$ (Hayashi, 1981) for the whole disc and scaled the solid surface density down by 50%, 75%, or 95% with respect to the MMSN value in the region beyond the depletion radius r_{dep}. The

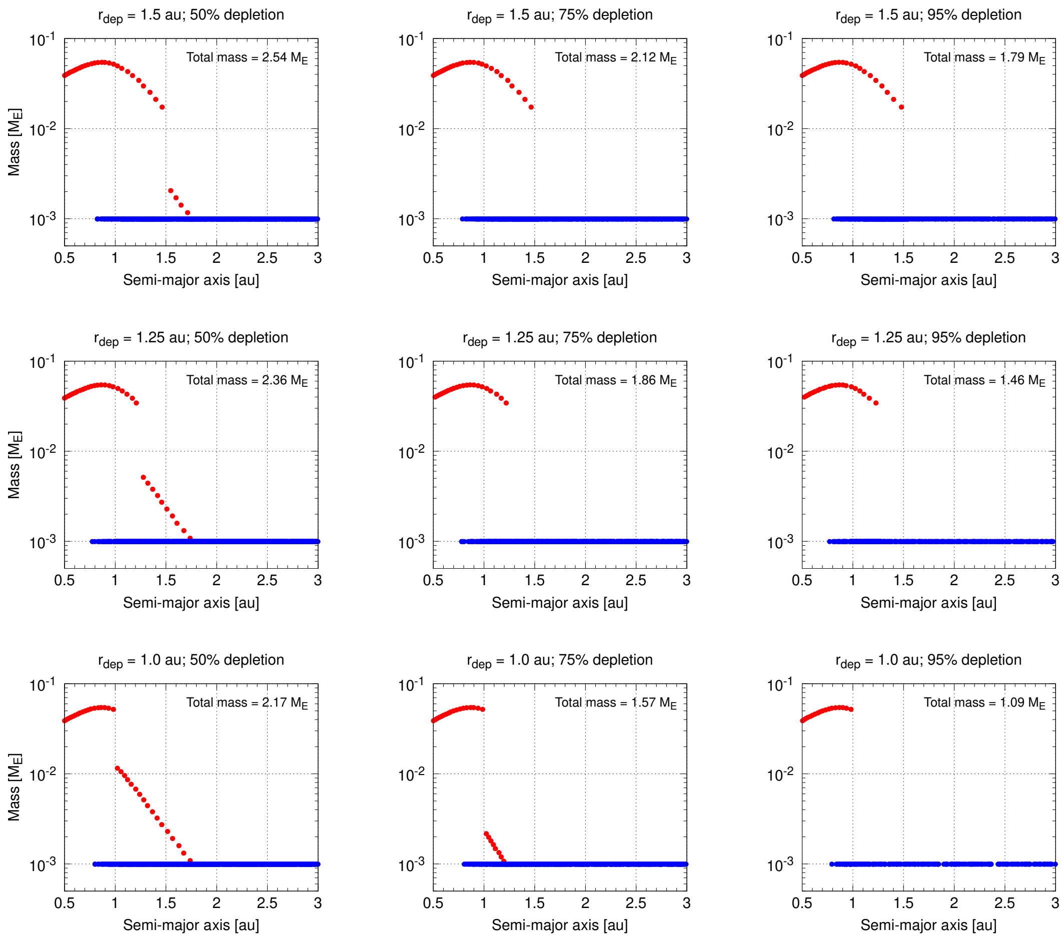

FIGURE 3.1: Initial mass and semi-major axis distribution of planetary embryos (red) and planetesimals (blue) for various values of depletion radius r_{dep} and scales of mass depletion.

mass in the solid disc was then distributed into a sequence of feeding annuli for embryos spaced 10 mutual Hill radii apart following the results of Kokubo and Ida (1998). The initial spacing of the embryos is close to a geometric progression $a_n = a_{n-1}[1+\beta(2M_{\text{iso}}/3M_{\odot})^{1/3}]$, where a is the semi-major axis, n is the index of the embryo, β is the mutual spacing between adjacent embryos, and $M_{\text{iso}} = 2\pi a \Sigma_s \beta$ is the embryo isolation mass. The isolation mass is the maximum mass that the embryos can attain depending on their location in the disc, their distance from adjacent embryos, and the disc's solid surface density.

Next, we computed the masses of the embryos M in their respective feeding annuli as a function of time according to (Chambers, 2006)

$$M(t) = M_{\text{iso}} \tanh^3\left(\frac{t}{\tau}\right). \tag{3.1}$$

In the equation above, τ is the embryo growth timescale introduced in Chambers (2006). It depends on the radii of the planetesimals R, in addition to a, β and Σ_s. We assumed $R = 10$ km when computing the embryos' growth timescales. The age of the solid disc when Jupiter has fully formed is denoted by t. We used $t = 1$ Myr in this work, based on the results of Kruijer et al. (2017). We chose to conduct this study with only one value of t to keep the number of simulations reasonable. At $t = 1$ Myr, the embryos would have attained only a fraction of their isolation masses. Finally, the remaining mass in the feeding annuli was subsequently allocated to planetesimals with masses equal to 0.001 Earth mass (M_E) each. The leftover mass in the disc at this stage is distributed to planetesimals so that the solid disc extends to the outer edge at 3.0 au.

The embryos and planetesimals were assigned orbital eccentricities e and orbital inclinations I from a Rayleigh distribution with scale parameters of the eccentricity distribution $\sigma_e = (M/3M_\odot)^{1/3}$, and the inclination distribution $\sigma_I = 0.5 \times \sigma_e$, respectively. The remaining orbital angles were chosen at random between 0° and 360° from a uniform distribution.

The evolution of systems of planetary embryos and planetesimals, including Jupiter and Saturn on their current orbits, were simulated using the SyMBA N-body integrator (Duncan et al., 1998) with a time step of 0.01 yr. In our simulations, the gas giants and the embryos were able to gravitationally interact with each other and the planetesimals. The planetesimals however, were unable to interact with themselves. Planetary bodies were removed from the simulations during collisions in which case they were assumed to have merged into a larger body perfectly, or when they ventured too close ($a < 0.3$ au) to or too far ($a > 100$ au) from the Sun.

The simulations were executed in two phases. In the first 5 Myr, we included the effect of a dissipating gas disc adopted from the prescriptions of Ida et al. (2016) which we detail in Appendix B.1. The temperature profile $T(r) \propto r^{-9/10}$ in the inner disc and $T(r) \propto r^{-3/7}$ in the outer disc. The gas disc exerts torques and tidal forces on the planetary bodies which result in a combined effect of radial migration and the damping of the orbital eccentricity and orbital inclination (Appendix B.2). We excluded the effects of gas-disc-induced migration (type-I migration) in all our simulations but retained the effects of eccentricity and inclination damping in an attempt to simplify the approach. This is because we want to focus on the isotopic composition of the terrestrial planets. We reserve studying the effects of type I migration for the future. After 5 Myr, we removed the gas disc artificially assuming that it has photoevaporated away completely; we then continued the simulations without the gas disc for another 150 Myr.

As the evolution of each system is chaotic, a slight difference in the initial orbital configuration of each embryo and planetesimal will give different results. It is therefore necessary to perform many simulations to understand the range of possible outcomes. For each set of initial condition, we ran 16 simulations for a total of 144. The simulations were ran on the computing cluster at the Earth Life Science Institute and on the PC cluster at the Center for Computational Astrophysics of the National Astronomical Observatory of Japan.

3.2.2 *N*-body simulation database of Grand Tack and classical models

In addition to the simulations for the depleted disc model, we also tap into our available database containing simulation output for the Grand Tack and classical models for a detailed comparison between the outcomes of the various models. The results of these simulations have already been published in Brasser et al. (2016) and Woo et al. (2018). We briefly summarise the initial conditions of these simulations below.

The simulations for the Grand Tack model started with Jupiter and Saturn migrating inwards through the asteroid belt in the first 0.1 Myr after the beginning of the solar system as given by the formation of the calcium-aluminium-rich inclusions (CAI). When Jupiter reaches 1.5 au, it reverses its migration direction and ushers Saturn along until they reach their proposed semi-major axis at ~5.4 au and ~7.5 au, respectively (Morbidelli et al., 2007) before the late giant planet instability. Within the orbits of Jupiter and Saturn, a solid disc composed of embryos and planetesimals having nearly circular and coplanar orbits was placed between 0.7 and 3 au. The surface density of embryos and planetesimals follows $\Sigma_s \propto r^{-3/2}$. The initial mass of the embryos are either (a) identical throughout the disc (Jacobson and Morbidelli, 2014) with the total mass ratio of embryos to planetesimals being 1:1, 4:1 or 8:1, or (b) computed using a semi-analytic oligarchic growth model (Chambers, 2006) where the mass and spacing between embryos are dependent on the embryos' isolation mass (Kokubo and Ida, 1998). The initial density of the planetesimals are assumed to be 3000 kg m^{-3}. The simulations were ran for 150 Myr using a time step of 0.02 yr. The gas disc model adopted was based on Bitsch et al. (2015), which features a higher surface gas density than the one employed by Walsh et al. (2011) in their first Grand Tack simulations. The initial gas surface density profile $\Sigma_g(r) \propto r^{-1/2}$, and the temperature profile $T(r) \propto r^{-6/7}$. Both the gas surface density and temperature profiles decay until $t = 5$ Myr in the simulation, after which the disc is artificially photoevaporated over the next 100 kyr.

The initial conditions for the classical model simulations are similar to those for the Grand Tack model, except that Jupiter and Saturn stayed on their current orbits throughout the simulations. Woo et al. (2018) only investigated the case where the embryos were assumed to have undergone oligarchic growth (Chambers, 2006).

There are several differences between the initial conditions of the numerical simulations described here and those for the depleted disc model: (1) the inner edge of the solid disc for the Grand Tack and classical model simulations are set at 0.7 au while it is at 0.5 au for the depleted disc model, and (2) the gas disc model adopted for the Grand Tack and classical model simulations is based on Bitsch et al. (2015) with a disc temperature profile of $T(r) \propto r^{-6/7}$ while we employ the gas disc model of Ida et al. (2016) with disc temperature profiles of $T(r) \propto r^{-9/10}$ in the inner disc and $T(r) \propto r^{-3/7}$ in the outer disc for the depleted disc model.

3.2.3 Selection criteria for terrestrial planet analogues and computation of feeding zones

At the end of the simulations, we tabulated the number of terrestrial planets produced. We considered all planetary bodies with masses larger than 0.01 $M_{\rm E}$ to be planets. These planets were further filtered to identify good terrestrial planet analogues. We followed the criteria of Brasser et al. (2016) for the masses M and final semi-major axes $a_{\rm f}$ that the planets must comply with to qualify as good terrestrial planet analogues.

- Venus: $0.4\ M_{\rm E} < M < 1.2\ M_{\rm E}$, $0.55\ \text{au} < a_{\rm f} < 0.85$ au
- Earth: $0.5\ M_{\rm E} < M < 1.5\ M_{\rm E}$, $0.85\ \text{au} < a_{\rm f} < 1.15$ au
- Mars: $0.05\ M_{\rm E} < M < 0.15\ M_{\rm E}$, $1.3\ \text{au} < a_{\rm f} < 1.7$ au

We did not attempt to place constraints for Mercury analogues as there remains many open questions about its formation history.

For each good terrestrial planet analogue, we tracked their accretion histories throughout the simulation to obtain the initial semi-major axis of all the planetary bodies they accreted. This information is then used to compute the feeding zones of the terrestrial planet analogues. The feeding zone of a planet provides us with information on the region in the disc where the terrestrial planets sample most of their building blocks from. It is quantified by the mass-weighted mean $a_{\rm weight}$ and width $\sigma_{a_{\rm weight}}$ of the distribution of the initial semi-major axes of all the solids accreted by the planet throughout its growth history (Kaib and

Cowan, 2015). These quantities are expressed mathematically as (Woo et al., 2018)

$$\begin{aligned} a_{\text{weight}} &= \frac{\sum_i^N M_i a_i}{\sum_i^N M_i}, \\ \sigma_{a_{\text{weight}}} &= \sqrt{\frac{\sum_i^N M_i \left(a_i - a_{\text{weight}}\right)^2}{\frac{N-1}{N}\sum_i^N M_i}}, \end{aligned} \tag{3.2}$$

where M_i and a_i are the mass and semi-major axis of the ith body accreted by the planet, and N is the total number of planetary bodies accreted. Together, $(a_{\text{weight}} \pm \sigma_{a_{\text{weight}}})$ define the feeding zone. The results are then compared with that obtained from the Grand Tack and classical models (Brasser et al., 2016; Woo et al., 2018).

3.2.4 Selection criteria for asteroid analogues and computation of formation location

In total, we analysed 336 simulations from Brasser et al. (2016) for the Grand Tack model and 64 simulations from Woo et al. (2018) for the classical model, in addition to the 144 simulations we have for the depleted disc model. We defined all the planetary bodies, regardless of their final mass, in our simulations as Hungaria, Vesta and Hebe analogues if their final semi-major axes a_{f} fulfil the following criteria:

- Hungaria: 1.7 au $< a_{\text{f}} <$ 2.1 au
- Vesta: 2.1 au $< a_{\text{f}} <$ 2.5 au
- Hebe: 2.2 au $< a_{\text{f}} <$ 2.6 au

We relax the constraint on the final masses of the asteroid analogues as we are more interested in the range of their initial semi-major axis. This does not affect the outcomes and the conclusions that we will draw for the study because the number of asteroid analogues larger than the mass of planetesimals ($= 0.001\ M_{\text{E}}$) in our Grand Tack model simulations only constitutes $\sim 21\%$ of the total while the fraction is a mere $0.6\% - 1\%$ for the classical model and $0.01 - 1.1\%$ for the depleted disc model.

The asteroid analogues had their accretion histories traced back in time to determine the initial semi-major axis of all the bodies that they accreted, or their initial semi-major axis in the case that they did not accrete anything throughout the simulation. We filtered out bodies with initial semi-major axis greater than 3 au because that is defined as the outer edge of the solid disc in our simulations. Finally, from the cumulative distribution of the initial semi-major axis for each asteroid analogue we computed the mass-weighted mean value, and the 5th and 95th percentile values.

3.3 Results

3.3.1 Depleted disc model: Terrestrial system architecture

In Fig. 3.2, we show the mass and semi-major axis distribution of the terrestrial planets formed at the end of our simulations with varying mass depletion scales at depletion radius 1.5 au, 1.25 au and 1.0 au. The peak of the mass distribution is located between 0.75 au and 1 au for $r_{\text{dep}} = 1.5$ au (top panels of Fig. 3.2), although the peak is not clear for the case of 50% mass depletion. The peak shifts inwards when the depletion radius r_{dep} is closer in. It is located at the current orbit of Venus for $r_{\text{dep}} = 1.0$ au (bottom panels of Fig. 3.2).

Most of the terrestrial planets produced in the simulations are generally less massive than the Earth and Venus, albeit with a few exceptions. Planet masses are also smaller

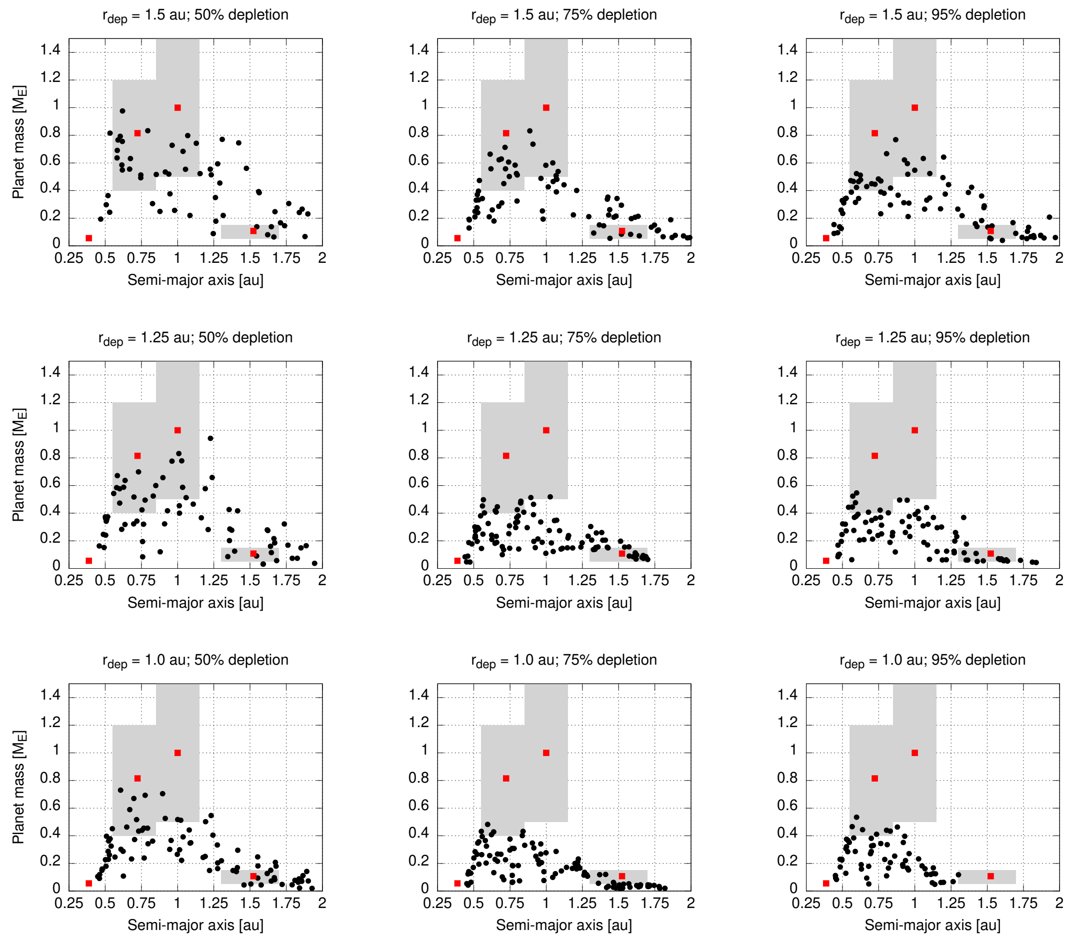

FIGURE 3.2: Mass and semi-major axis distribution of terrestrial planets formed at the end of our simulations for various scales of mass depletion at $r_{\text{dep}} = 1.5$ au (top row), 1.25 au (middle row) and 1.0 au (bottom row). Red squares are the current terrestrial planets, black circles are planets that formed in our simulations, and grey regions indicate the range within which planets are considered good terrestrial analogues. Plot taken from Mah and Brasser (2021).

when the depletion radius is closer to the Sun because the amount of mass available in the disc to form planets is smaller. This is an artefact of our initial conditions because we chose to keep the solid surface density fixed rather than increasing it in an attempt to reproduce the current masses of the terrestrial planets. Consequently, our simulations tend to produce more Venus analogues than Earth analogues (Table 3.1) because of the low total solid mass in the disc.

We ran additional simulations with increased initial solid surface density and find that increasing the surface density by a factor of 1.5 to 2 times the MMSN value will produce planet analogues with masses closer to those of the current terrestrial planets. The outcomes of these additional simulations are discussed in Appendix C.

Our simulations produce planetary systems with an average of 4 to 6 planets. However, as there usually are planets within Venus' present orbit that could be considered as Mercury analogues, the higher number of planets poses no severe problems for the depleted disc model. From our simulation results, we find 52 planetary systems, out of a total of 144, with Mars analogues. Among these, only 16 have planets with $a > 1.7$ au (upper limit of our criteria for Mars analogues) that could render them distinct from the Solar System.

TABLE 3.1: Total number of planets N, average number of planets in a system $\bar{n}$, probability of forming Venus, Earth, and Mars analogues for each initial condition, and probability of yielding both Earth and Mars analogues in the same planetary system.

r_{dep}	Mass depletion scale	N	$\bar{n}$	Venus analogues	Earth analogues	Mars analogues	Earth & Mars analogues
1.5 au	50%	57	3.6	23%	14%	7%	19%
	75%	78	4.8	15%	8%	8%	13%
	95%	80	5.0	18%	9%	8%	19%
1.25 au	50%	73	4.6	19%	8%	7%	19%
	75%	94	5.9	9%	2%	16%	6%
	95%	85	5.3	8%	0%	18%	0%
1.0 au	50%	86	5.4	12%	5%	9%	6%
	75%	104	6.5	6%	0%	6%	0%
	95%	63	3.9	10%	0%	2%	0%

3.3.2 Depleted disc model: Terrestrial system dynamical properties

We also examined the characteristics of final terrestrial systems produced from this model by employing several statistics introduced by Chambers (2001). The first of these is the angular momentum deficit (AMD), defined as

$$\mathrm{AMD} = \frac{\sum_k \mu_k \sqrt{a_k} \left[1 - \sqrt{\left(1 - e_k^2\right)} \cos I_k\right]}{\sum_k \mu_k \sqrt{a_k}}, \tag{3.3}$$

where $\mu_k = M_k / M_\odot$. The second is the mass concentration parameter S_c which measures the degree of mass concentration in one part of the planetary system, given by

$$S_\mathrm{c} = \max\left(\frac{\sum_k \mu_k}{\sum_k \mu_k \log(a/a_k)^2}\right). \tag{3.4}$$

The third is the fraction of total mass in the largest planet of the system S_m, and the last is the mean orbital spacing statistic S_H, given by

$$S_\mathrm{H} = \frac{2}{N-1} \sum_{k=1}^{N-1} \frac{a_{k+1} - a_k}{a_{k+1} + a_k} \left(\frac{\mu_{k+1} + \mu_k}{3}\right)^{-1/3}. \tag{3.5}$$

We use the mutual Hill sphere as the spacing unit for S_H, following Brasser et al. (2016).

The values of the aforementioned statistics for all of the planetary systems formed in our simulations are presented in Fig. 3.3. We also plot the current values of the Solar System and its 2σ range, obtained using a Monte Carlo method (Brasser et al., 2016), in grey shaded areas.

In the top panel of Fig. 3.3, we find that the majority of the planetary systems plot away and to the lower left part of the grey region, indicating that their S_m and S_H values are lower compared to the Solar System's current value. Their low S_m and S_H values mean that the mass difference between planets in the same planetary system are small and the planets are more closely-packed than the current terrestrial planets. Only 20 out of a total of 144 planetary systems have S_m and S_H values similar to the current terrestrial system and most

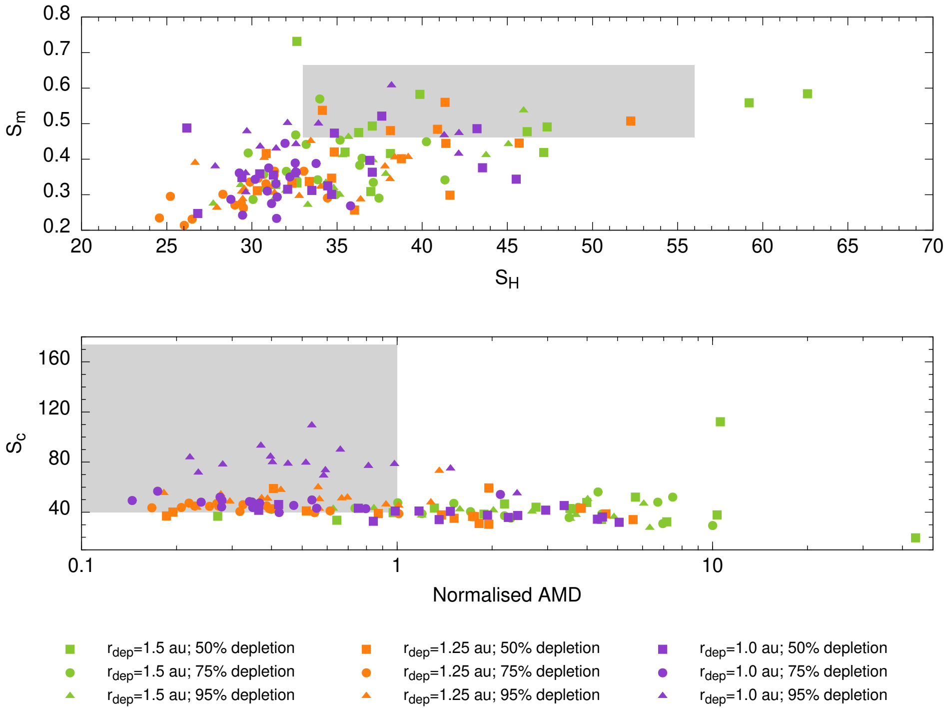

FIGURE 3.3: Top panel: Mass in largest planet as a fraction of the total mass of the planetary system S_m versus the mean spacing parameter S_H in units of the mutual Hill sphere. Bottom panel: Mass concentration parameter S_c versus the angular momentum deficit (AMD) normalised to the current Solar System value. The grey regions encompass the current values of the inner Solar System and the 2σ range. Plot taken from Mah and Brasser (2021).

of them correspond to the initial condition of 50% mass depletion (square symbols). Among these systems, 12 possess Earth analogues, 7 possess Mars analogues, and 6 possess both Earth and Mars analogues. There are 6 systems with neither Earth nor Mars analogues.

In terms of the concentration parameter S_c, the majority of the final planetary systems have low S_c values but the initial condition of $r_{dep} = 1.0$ au and 95% (purple triangles in the bottom panel of Fig. 3.3) is able to produce planetary systems with higher S_c values that are close to the Solar System's current value. However, these planetary systems failed to form any Earth analogues and barely succeed in forming Mars analogues. In terms of the AMD, the planetary systems have values that range widely from 10 times smaller to 10 times larger than the current value. We chose to define successful cases as planetary systems with AMD less than the current Solar System's value because the AMD is expected to increase in time due to chaotic diffusion (Laskar, 2008). It is thus likely that the AMD at 4.5 Ga ago was lower than what it is today. These results of the dynamical properties of planetary systems formed in the framework of the depleted disc model are expected due to the fixed surface density that we employed.

3.3.3 Depleted disc model: Terrestrial planet feeding zones

In Fig. 3.4, we present the feeding zones ($a_{\text{weight}} \pm \sigma_{a_{\text{weight}}}$) of the good terrestrial planet analogues, i.e., those that satisfy the criteria listed in Section 3.2.3. The feeding zones of the terrestrial analogues display a correlation with their final semi-major axis, indicating that the planets tend to accrete material mostly locally.

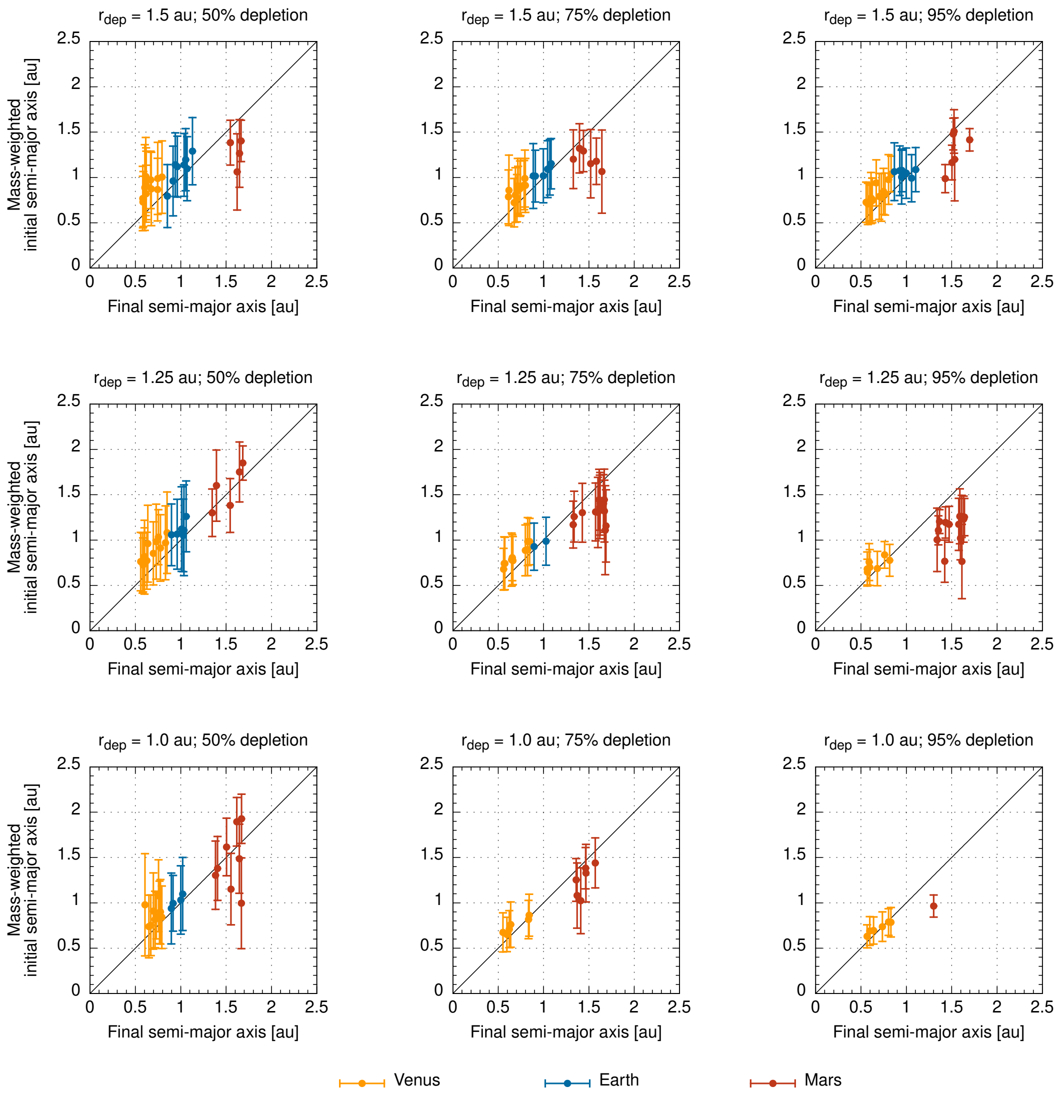

FIGURE 3.4: Feeding zones ($a_{\text{weight}} \pm \sigma a_{\text{weight}}$) of the Venus, Earth and Mars analogues versus their final semi-major axis from simulations of the depleted disc model with different initial conditions. The black line corresponds to the equation $y = x$.

The trend of the local feeding zones likely arose from the eccentricity damping effect exerted by the gas on the embryos and planetesimals in the first 5 Myr of the simulation. Planetesimals are kept at low eccentricity (nearly circular) orbits and as a result they tend to get accreted onto nearby embryos. Embryos are typically 0.1 M_{E} or smaller so the escape velocity at their surfaces is roughly 5 km s^{-1} and thus the maximum eccentricity the embryos can obtain from embryo-embryo scattering is about 0.1. Therefore, we expect the feeding zones for the final Earth and Venus analogues obtained from this mode to be narrow and distinct.

For some Mars analogues, however, the same feeding zone trend does not apply. We observe a spread in the feeding zones of our Mars analogues and some of them deviate from the trend. For example, the Mars analogues in the simulations with a 75% mass depletion beyond r_{dep} = 1.5 au have their feeding zones centered around 1.25 au (top middle panel of Fig. 3.4). We examined the evolution of these Mars analogues that deviate from the trend and found that they were formed closer in initially (a < 1.5 au) and was subsequently scattered

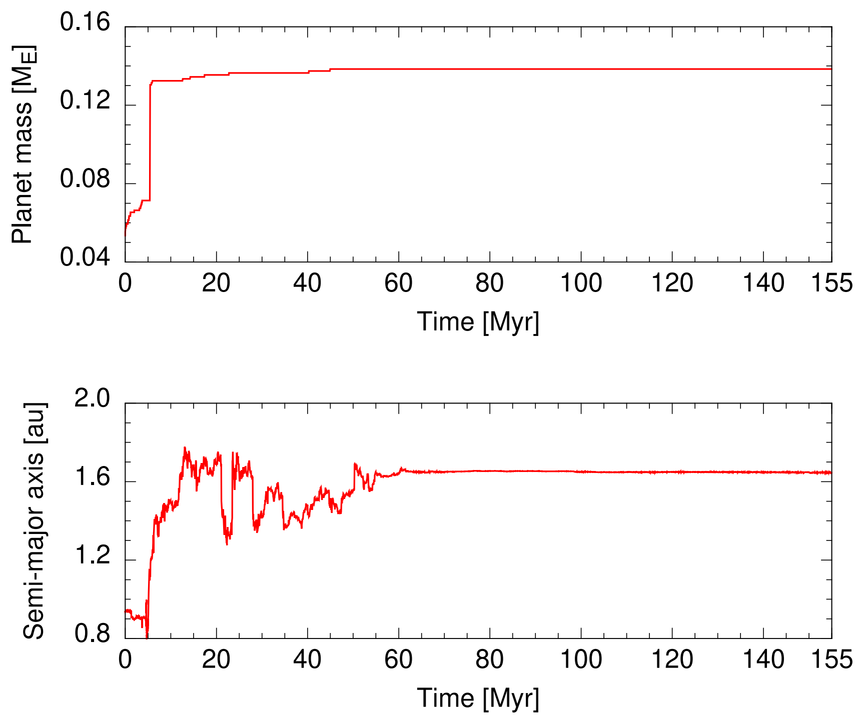

FIGURE 3.5: Time evolution of the mass and semi-major axis of a sample Mars analogue which feeding zone is centered at $a < 1.5$ au. Plot taken from Mah and Brasser (2021).

outwards to their final orbits (Fig. 3.5). As most of their building blocks comprise material from within 1.5 au, it is reflected in their feeding zones that are centred at $a \approx 1.25$ au.

3.3.4 Formation location of Vesta

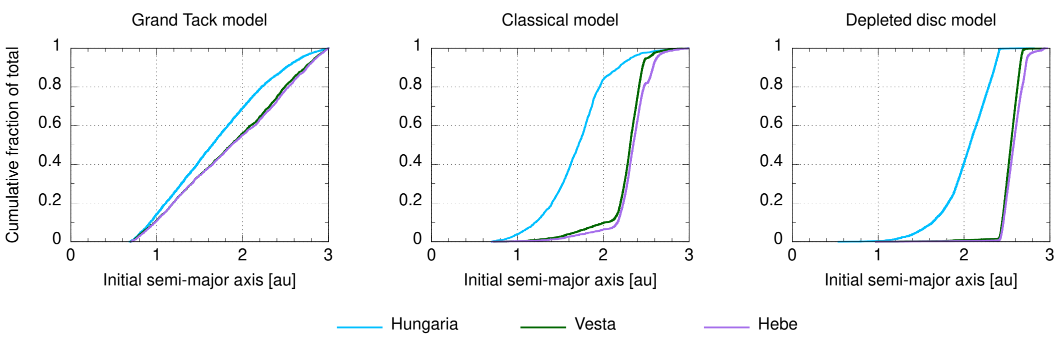

FIGURE 3.6: Cumulative distributions of the initial semi-major axis of Hungaria, Vesta and Hebe analogues in the Grand Tack (left panel), classical (middle panel), and depleted disc (right panel) models. The asteroids have equal probability of originating from anywhere in the disc for the Grand Tack model while their origin locations are more restricted in the classical model and the depleted disc model.

The formation location of asteroid analogues Hungaria, Vesta and Hebe in the Grand Tack, classical, and depleted disc models are shown in Fig. 3.6. In the Grand Tack model, Vesta analogues are equally likely to originate anywhere in the disc between 0.7 au and 3.0 au with a 20% probability of forming within 2.1 au to 2.5 au (left panel of Fig. 3.6). In contrast, in the classical model and the depleted disc model, the initial semi-major axes of the Vesta analogues are severely restricted (middle and right panels of Fig. 3.6). The probability of Vesta analogues originating from between 2.1 au to 2.5 au is 84% for the classical model and 30% for the depleted disc model. The reason for the lower probability in the depleted disc model is due to the gas drag exerted on the planetesimals by the gas disc in the first 5 Myr of the simulations. The eccentricity damping effect still causes the planetesimals to migrate inwards when the gas was present. Consequently, most of the Vesta analogues (68% of the total) in the depleted disc model originate from the region between 2.5 au and 2.7 au.

The trend of formation location for Hebe analogues are very similar to that for Vesta analogues across the three dynamical models. In particular, for the classical model and the depleted disc model, these asteroid analogues ($a_{\mathrm{f}} > 2$ au) have very restricted formation locations because there are no planetary embryos beyond 2 au in the disc to perturb the orbits of the planetesimals. The Hungaria analogues on the other hand have a wider distribution for their potential formation locations because they are located closer in (1.7 au $< a_{\mathrm{f}} <$ 2.1 au) and thus are more prone to perturbations by planetary embryos during the formation of the terrestrial planets.

It has been suggested in the literature that the asteroid belt was devoid of mass when the Solar System formed and was subsequently populated by planetary bodies deriving from other regions of the protoplanetary disc, in particular the terrestrial planet region (Raymond and Izidoro, 2017b). Vesta's origin in particular has been suggested to be in the terrestrial planet region (e.g., Bottke et al., 2006) or even in the outer Solar System (Raymond and Izidoro, 2017a). However, an origin in the outer disc is inconsistent with isotopic data as Vesta would thus be expected to be isotopically akin to (some of) the carbonaceous chondrite meteorites (e.g., Warren, 2011). In models where the gas giants remained on their current orbits, almost all of the Vesta analogues originated from within the asteroid belt. Therefore, Vesta's distinct isotopic composition compared to the terrestrial planets and the carbonaceous chondrites, its similarity to several other achondritic meteorite groups such as the brachinites and angrites in their oxygen isotopic compositions (Clayton and Mayeda, 1996), and the narrow range in initial semi-major axis from the dynamical models not involving the migration of the gas giants suggest an origin that is most likely in the asteroid belt and not in the inner solar system nor the outer solar system.

3.4 Discussion

3.4.1 Comparison with the Grand Tack and classical models

Comparing the feeding zone trend of the depleted disc model with that of the Grand Tack and classical models, we see that the correlation with semi-major axis is strongest for the depleted disc model and weakest for the Grand Tack model (Fig. 3.7). The feeding zones of the terrestrial planets for the Grand Tack model have a large width and a similar range (from 0.7 to 2.0 au) with the slope of the best-fit line = 0.06 indicating almost no correlation with semi-major axis. The feeding zone trend of the Grand Tack model is due to the gas-driven inward-then-outward migration of the gas giants that enhances the mixing of materials in the disc. By contrast, in the depleted disc model the feeding zone widths are more restricted and the feeding zone range for each planet is different with the slope of the best-fit line having a higher value of 0.52. This is because of the limited extent of material mixing in the solid disc in the depleted disc model. The mass in the region beyond the orbit of Mars is too low to cause sufficient perturbations to the orbits of solid material closer to the Sun. For the case of the classical model, the slope of the best-fit line is a combination of two factors: (1) the inner edge of the solid disc is set at 0.7 au causing Venus analogues to only accrete material from beyond 0.7 au, and (2) there are too few Mars analogues due to the large amount of mass in

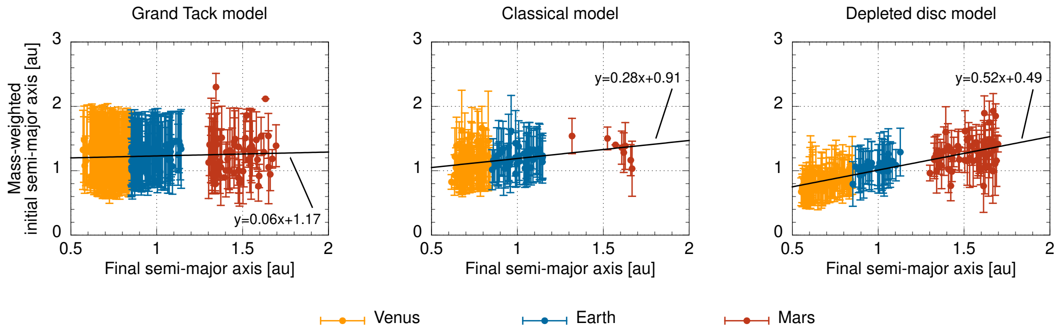

FIGURE 3.7: Comparison of all the Venus, Earth and Mars analogues' feeding zones for the Grand Tack model (left panel), classical model (middle panel), and depleted disc model (right panel). Feeding zone data for the Grand Tack and classical models are from our simulation database. The Grand Tack simulations used to compute the feeding zones include simulations with different tack locations for Jupiter (1.0 au and 1.5 au), simulations beginning with equal-mass planetary embryos, and simulations with embryos assumed to have underwent oligarchic growth. The results from all the aforementioned Grand Tack simulations are combined because there are no obvious differences between the outcomes from different initial conditions (Brasser et al., 2016).

this region of the disc. It is possible to obtain a steeper value for the slope if the solid disc's inner edge is extended to 0.5 au and/or if the initial orbital configuration of the gas giants is changed (Woo et al., 2021).

In the ideal case where the planets accrete all their building blocks locally, the feeding zones will display a 1:1 relation with semi-major axis. The slopes of the best-fit line for the three dynamical models examined here deviate from 1 because mixing is inevitably present in the disc in realistic cases due to the gravitational perturbation on the planetesimals by planetary embryos. The feeding zone trend is therefore a reflection of the degree of mixing in the disc. It is strongest for the Grand Tack model and weakest for the depleted disc model.

We next examine how big is the difference between the feeding zones of the Earth and Mars analogues for the depleted disc model and the Grand Tack model. We will not consider the results of the classical model here as it does not form many Mars analogues with the correct size to make good comparisons. From the depleted disc and Grand Tack models, we singled out the planetary systems which possess both Earth and Mars analogues (13 and 37 systems, respectively) and computed the difference between $a_{\mathrm{weight,Mars}}$ and $a_{\mathrm{weight,Earth}}$. For systems with multiple Mars analogues, we chose the planet analogue with semi-major axis closest to 1.5 au. The cumulative distribution is presented in Fig. 3.8. We find that the region in the disc where Mars analogues sourced most of their building blocks is generally more distant than the Earth in the depleted disc model, whereas it is closer to the Earth in the case of the Grand Tack model.

To further quantify the difference in the feeding zones of the Earth and Mars analogues produced in the depleted disc and Grand Tack models, we computed their overlapping coefficient (OVL). The OVL measures the similarity between the two distributions and is defined as the common area under two probability density functions. For planetary systems with both Earth and Mars analogues, we traced their respective accretion histories to obtain the mass-weighted initial semi-major axis of all the planetary embryos and planetesimals accreted onto these two planets. We then combined the mass-weighted initial semi-major axis Ma data for all the Earth and Mars analogues in each model (Fig. 3.9) to compute the OVL. This is done for better statistics as some of the Mars analogues only accreted a few planetesimals which results in a rather grainy probability function. The OVL is computed as

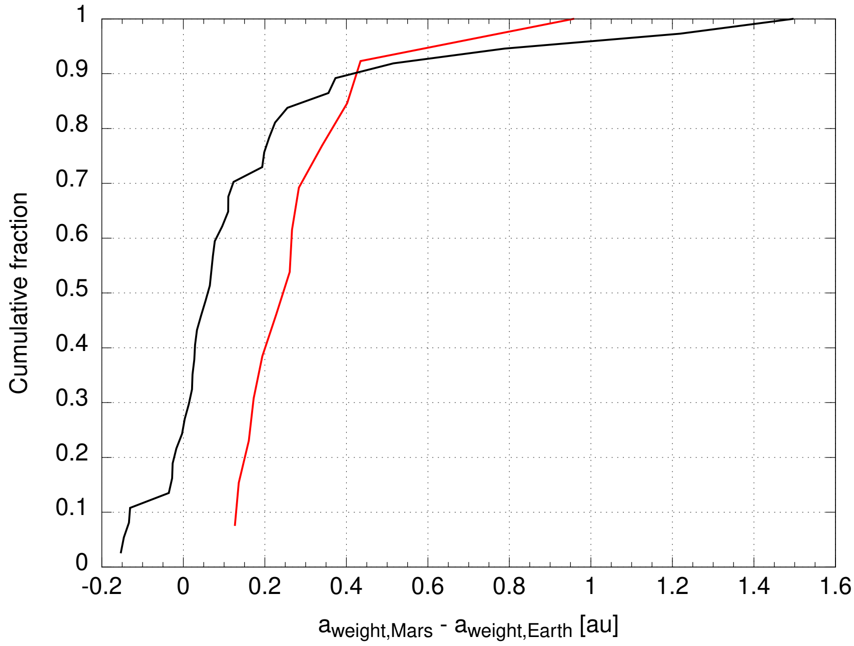

FIGURE 3.8: Cumulative distribution of the difference between the mass-weighted mean initial semi-major axis of all the planetary embryos and planetesimals accreted by both Mars and Earth analogues in the depleted disc model (red) and the Grand Tack model (black). Plot taken from Mah and Brasser (2021).

the sum of the lower value between the probability distribution functions of Earth and Mars over the whole range of values for Ma, expressed as

$$\mathrm{OVL} = \sum_{Ma} \min\left[f_{\mathrm{Mars}}\left(Ma\right), f_{\mathrm{Earth}}\left(Ma\right)\right]. \tag{3.6}$$

We find $\mathrm{OVL}_{\mathrm{DD}} = 0.79$ for the depleted disc model, and $\mathrm{OVL}_{\mathrm{GT}} = 0.89$ for the Grand Tack model.

The OVL results suggest that the difference in feeding zones between Earth and Mars is $\sim 20\%$ in the depleted disc model, and $\sim 10\%$ in the Grand Tack model. What does this difference actually mean? Naively, one would expect a 10% difference to imply that Mars' oxygen isotopes would result in a Δ^{17}O of either 0.10 or −0.10‰ ($\Delta^{17}\mathrm{O} = 0$ for Earth); instead the observed isotopic anomaly of 0.29‰ would suggest an OVL difference of $\sim 30\%$, which is closer to the depleted disc value rather than the Grand Tack value. The question then becomes: What did Mars accrete that the Earth did not?

One interpretation of the different OVL values could be in the fraction of ordinary chondrites accreted by Mars because it is the only quantity that is potentially significantly different when one considers the terrestrial planets to be mixtures of chondrites (e.g., Lodders and Fegley, 1997; Sanloup et al., 1999; Dauphas, 2017; Brasser et al., 2018). We applied the same technique to compute the OVL for the distributions from our improved mixing model simulation (shown earlier in Fig. 1.2). For the 20 different mixing model iterations, we computed the OVL by averaging over all possible permutations between the best-fit composition of Earth and Mars. We find $\mathrm{OVL}_{\mathrm{MCMC}} = 0.58 \pm 0.08$, which is clearly attributed to the increased H chondrite fraction in Mars versus a higher fraction of carbonaceous material in the Earth (Fig. 1.2). Taking the mixing model as our benchmark for the OVL, the depleted disc model does a better job than the Grand Tack.

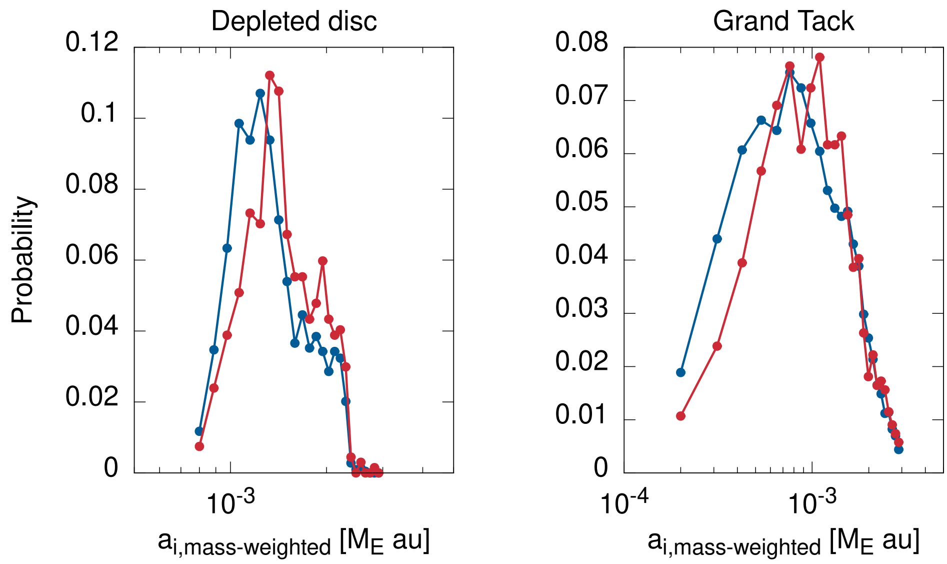

FIGURE 3.9: Probability distribution function of the mass-weighted initial semi-major axis of all the planetary embryos and planetesimals accreted by Earth (blue) and Mars (red) in the depleted disc model and the Grand Tack model. The distribution for Mars is systematically displaced to the right for the depleted disc model. Plot taken from Mah and Brasser (2021).

TABLE 3.2: K-S test results. Maximum difference between each pair of data points D, and the probability of agreement P in the cumulative distributions of each planet pair in the Grand Tack, classical and depleted disc models. Also listed is the number of data points N selected for the test.

	Grand Tack (N=1718)		Classical (N=323)		Depleted disc (N=2706)	
	D	P (%)	D	P (%)	D	P (%)
Venus-Earth	0.014	99.6	0.071	37.7	0.110	0.0
Earth-Mars	0.035	22.5	0.200	0.0	0.086	0.0
Venus-Mars	0.035	24.2	0.258	0.0	0.175	0.0

Finally we conduct a Kolmogorov-Smirnov (K-S) similarity test on the cumulative distributions of the initial semi-major axis of all the planetary bodies accreted onto all of the Venus, Earth and Mars analogues in the Grand Tack, classical, and depleted disc models. We selected $N = 1718,\ 323$ and 2706 equally-spaced data points from the cumulative distributions of the Grand Tack, classical, and depleted disc models for the test. For each planet pair (Venus-Earth, Earth-Mars, Venus-Mars) in each model, we computed the maximum difference between each pair of data points D and the corresponding probability of agreement P. If the value of P is greater than 5%, then the two distributions are said to be statistically identical. Table 3.2 shows the results of the test for the three dynamical models. The results suggest that the accretion regions of the terrestrial planets in the Grand Tack model are identical ($P > 5\%$) while the accretion regions are distinct in the depleted disc model. For the classical model, the similarity between the accretion regions of Venus and Earth is likely due to the inner edge of the solid disc being set to 0.7 au in the simulations, which results in Venus analogues only sampling material from > 0.7 au in the disc (Woo et al., 2018).

Given the results of the two statistical tests we conducted (OVL, K-S test), we conclude that the predictions of the depleted disc model comports best with the isotopic compositions measured for the Earth and Mars. In this model, the feeding zones of the terrestrial planets show a clear correlation with semi-major axis. Earth and Mars would accrete material from different regions in the protoplanetary disc and they can end up with different final mixtures of building material with the presence of isotopic gradients in the disc. This is in stark contrast with the the Grand Tack model which predicts identical isotopic compositions for Earth and Mars.

3.4.2 Implications for Venus' isotopic composition

Our simulation results for the depleted disc model show that Venus, Earth and Mars accreted from different, localised regions of the protoplanetary disc. Thus, a direct implication of the model is that Venus should be isotopically distinct from the Earth and Mars. A prediction of its isotopic composition for Δ^{17}O–ε^{50}Ti–ε^{54}Cr can be obtained by making use of the correlation between the feeding zones of the terrestrial planets shown in Fig. 3.7 and the corresponding isotopic anomalies for Earth and Mars. This assumes a linear relationship between the disc's isotopic composition and semi-major axis (Pahlevan and Stevenson, 2007). The predicted isotopic anomalies for Venus ε_V can be computed using the relation

$$\varepsilon_V = \frac{a_V - a_E}{a_M - a_E} \times \varepsilon_M, \tag{3.7}$$

where the subscripts V, E and M refer to Venus, Earth and Mars, respectively. We computed the nominal values of the isotopic anomalies of Venus using the current semi-major axes of the terrestrial planets and plotted them as open squares in Fig. 3.10.

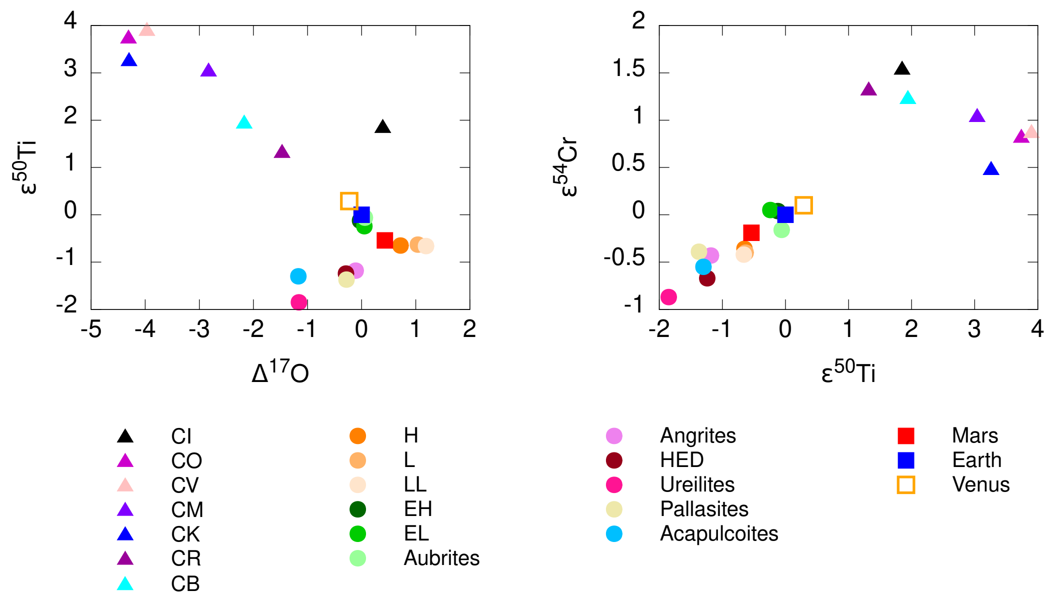

FIGURE 3.10: Predicted isotopic anomalies in chromium, oxygen and titanium for Venus (orange open square) based on terrestrial planet feeding zone trend observed for the depleted disc model. Meteorite isotope anomalies data for Δ^{17}O sourced from Clayton and Mayeda (1983, 1996); Franchi et al. (1999); Rubin et al. (2000); Mittlefehldt et al. (2008); Agee et al. (2013); Wittmann et al. (2015), ε^{50}Ti from Trinquier et al. (2009); Zhang et al. (2011, 2012), and ε^{54}Cr from Shukolyukov and Lugmair (2006); Trinquier et al. (2007, 2008); Qin et al. (2010a,b); Yamashita et al. (2010); Larsen et al. (2011); Petitat et al. (2011); Yamakawa and Yin (2014). Martian meteorites used to compute the average value for Mars are ALH 84001, DaG 476, Chassigny, Lafayette, Nakhla, NWA 856, NWA 2737, NWA 7034, Shergotty and Zagami. Plot taken from Mah and Brasser (2021).

In computing the nominal isotopic composition for Venus, we used the Earth-Mars correlation instead of Earth-Mars-Vesta. Although the Earth-Mars-Vesta trend is present for

TABLE 3.3: Predicted values for the isotopic anomalies of Venus computed using a linear extrapolation of the Earth-Mars trend and using a Monte Carlo method, and the fraction of Venus analogues generated by the Monte Carlo method that is more isotopically distinct from the Earth than Mars is.

	Nominal	Monte Carlo	$\lvert\varepsilon_V - \varepsilon_E\rvert > \lvert\varepsilon_E - \varepsilon_M\rvert$
$\Delta^{17}O$	-0.23	$-0.12^{+2.69}_{-2.74}$	50%
$\varepsilon^{50}Ti$	0.29	$0.26^{+3.37}_{-3.43}$	48%
$\varepsilon^{54}Cr$	0.10	$0.07^{+1.20}_{-1.19}$	49%

ε^{50}Ti and ε^{54}Cr, it is not the case for Δ^{17}O where Vesta has a negative value, in contrast to the positive values of the Earth and Mars. The uncertainties in the isotopic anomalies were computed using a Monte Carlo method. We employed the Box-Mueller transform to generate values for the semi-major axes of Venus, Earth, and Mars, as well as the isotopic anomalies in Δ^{17}O, ε^{50}Ti and ε^{54}Cr for Mars according to a normal distribution with mean equal to the mean semi-major axes of the feeding zones of the planets, and the standard deviation being a quarter of the feeding zones' width. We then computed the isotopic anomalies of Venus using Eq. 3.7. After 10^5 iterations, we obtain the isotopic anomalies and their corresponding uncertainties by computing the mean, 5th percentile and 95th percentile values. We report the values in Table 3.3. There is a huge spread in the predicted isotopic anomalies of Venus, and this is due to the fact that (1) the value of $(a_V - a_E)/(a_M - a_E)$ can be very small, which results in large variations, and (2) some Mars analogues do not follow the same trend as the Earth and Venus, which skews the values. We also find that about half of the Venus analogues generated by the Monte Carlo method are predicted to have isotopic compositions that are more distinct from the Earth compared to Mars.

Interestingly enough, using the extrapolation from the Earth and Mars trend implies that Venus plots in between the Earth and the carbonaceous/jovian material, which could naively be interpreted as Venus having accreted a higher fraction of carbonaceous/jovian material than the Earth, although this interpretation makes little sense dynamically. The Earth-Mars-Vesta trend in ε^{50}Ti and ε^{54}Cr is continued to Venus, but since Vesta is negative in Δ^{17}O there is no such trend for the O isotopes. Our predicted isotopic compositions for Venus also suggest that the angrite meteorites could not have originated from Venus.

Isotope measurements for meteorites or rock samples from Venus will therefore be crucial to know its O isotopic composition (Greenwood and Anand, 2020), and provide evidence for or against the presence of a reservoir enriched in *s*-process elements that the Earth is said to have accreted some of its building blocks from (Render et al., 2017). Venus should have accreted a larger fraction of its building blocks from this *s*-process nuclides enriched reservoir given the presence of a potential isotopic gradient in the protoplanetary disc and that it is located closer to the Sun as compared to the Earth.

3.5 Conclusions

We examined the masses, orbital configurations, and feeding zones of the terrestrial planets formed in the framework of the depleted disc model by running a large number of *N*-body simulations with different initial conditions and including the effects of a dissipating gas disc during the first few Myr of the simulations. We found that the model outputs planets that are less massive than the current terrestrial planets if we assume a MMSN surface density for the solids in the protoplanetary disc, but the model is successful nevertheless in producing planets with low mass in the region near Mars' orbit. Increasing the initial surface density of the solids in the protoplanetary disc by 1.5 to 2 times the MMSN value will resolve the deficit in the terrestrial planets' mass.

Despite the mass depletion in the protoplanetary disc being an ad-hoc assumption, the depleted disc model provides a promising initial condition to form Mars with the correct mass, a problem that has plagued the classical model and inspired the development of subsequent models. The origins of such a concentration of mass in the terrestrial planet region of the protoplanetary disc is not yet known. Several suggestions include a difference in viscosity in different parts of the disc causing material to preferentially flow towards the high-viscosity region (Jin et al., 2008), the growth and inward drift of dust causing the solids in the whole disc to redistribute themselves and preferentially pile-up near the inner edge of the disc (Drążkowska et al., 2016), and the presence of a potential pressure bump in the disc near 5 au causing the outward migration of material originally located in the asteroid belt (Brasser and Mojzsis, 2020). However, these scenarios remain speculative as there has not yet been any investigation to determine an origin for the depleted disc model to this date. We will leave this for future work.

Perhaps more importantly, this model predicts distinct isotopic compositions for the Earth, Mars and Vesta, consistent with cosmochemistry data. This is in contrast to the Grand Tack model where the most likely outcome for the isotopic compositions of Earth, Mars and Vesta is that they are identical. Our results therefore suggest that the early gas-driven migration of Jupiter and Saturn into the inner solar system was unlikely to have occurred but it could have happened at a later time instead (e.g., Clement et al., 2018). Its effect on the degree of mixing in the inner disc deserves detailed investigation in the future.

4 Summary and future work

4.1 The thesis in brief

We presented two studies in this thesis aiming to shed light on the formation pathway of the terrestrial planets, guided by the cosmochemistry observations that the Earth, Mars and Vesta all are distinct in their isotopic compositions and that their isotopic compositions show a correlation with their semi-major axis.

The first study examines the role of pebble accretion in the inner Solar System during the lifetime of the gas disc. This study is motivated by the work of Levison et al. (2015b) who showed that pebble accretion could help inner disc planetesimals gain enough mass before the gas dissipates, thus preparing them to form the terrestrial planets in the subsequent stages of planetesimal collision and giant impact, and more recently the work of Johansen et al. (2021) who showed that pebble accretion could perhaps contribute a large fraction to the masses of the terrestrial planets. Furthermore, Schiller et al. (2018) proposed that the accretion of outer Solar System material, possibly in the form of pebbles, onto a disc of planetesimals with ureilite-like isotopic compositions could be a possible generating mechanism behind the observed mass-isotopic-composition correlation for Earth, Mars and Vesta.

We simulated the growth of a disc of planetesimals (with a range of diameters) in the terrestrial planet region when they are subjected to a flux of pebbles originating in the outer Solar System. At the end of the simulations ($t = 4$ Myr), we find that planetesimal discs made up of many planetesimals with diameters ≥ 300 km ($0.05\ M_\mathrm{E} \leq M_\mathrm{disc,i} \leq 0.25\ M_\mathrm{E}$) will increase their mass by at least few times their initial mass, depending on the temperature of the gas disc and if gas-induced migration effects are included. This is despite Jupiter almost halting the pebble flux when it reaches its isolation mass. Such a large amount of mass increase contributed by outer Solar System pebbles would imply that the isotopic composition of the planetesimals will be replaced by the isotopic signatures of the pebbles. Planetary bodies formed by the subsequent collisions among these planetesimals are expected to have isotopic compositions similar to the outer Solar System bodies, which is inconsistent with the isotopic dichotomy revealed by currently available meteorite samples.

On the other hand, if the planetesimals in the inner Solar System are mostly bodies with diameters < 300 km ($M_\mathrm{disc,i} \leq 10^{-3}\ M_\mathrm{E}$) then the amount of mass increase in the disc is limited. The mass increase in the disc ranges from 15% to about 300%, depending on the initial mass of the planetesimal disc and assuming that the pebbles sublimate into smaller-sized grains at the snow line. The amount of mass accreted in the form of pebbles is however, still considered to be quite high based on the results of chondritic mixing models (e.g., Dauphas, 2017) that the maximum contribution of outer Solar System material to the mass of the Earth is about 10%. In the case where we disregard the fragmentation effects, the mass increase in the disc can be less than 10% the initial disc mass. However, the more important problem for these discs with small planetesimals is that the final mass in the disc by the time the gas disc dissipates is insufficient to form the terrestrial planets.

It is more likely that the solid disc in the inner Solar System was more massive than 10^{-3} $M_{\rm E}$ and thus should contain more planetesimals larger than 300 km in diameter. Since the growth of these planetesimals proceed at a faster rate (due to their higher accretion efficiency), it is expected that the contribution by pebbles to the mass in the terrestrial planet region is very large and that such a large contribution can replace the initial isotopic signature of the planetesimals. Based on our simulation results, we suggest that it is rather unlikely for pebble accretion to play a major role in the formation of the terrestrial planets. Our results are in contrast with those of previous studies (Levison et al., 2015b; Johansen et al., 2021) mainly because of the different assumptions made. We assumed that the pebbles formed in the outer Solar System beyond the orbit of Jupiter whereas the previous studies assume for example, that (a) the pebbles form in the inner Solar System (Levison et al., 2015b), or that (b) there was a change in the isotopic composition of the pebbles from non-carbonaceous-chondrite-like to carbonaceous-chondrite-like within the lifetime of the gas disc (Johansen et al., 2021). As the pebble accretion mechanism is widely studied in the community, our understanding of it is gradually improving. This leaves room for further examinations of the plausibility and validity of the assumptions used by current works.

The second study investigates the predictions of the depleted disc model for the isotopic compositions of the terrestrial planets and the formation location of asteroid Vesta. In this study, we modelled the growth of a solid disc containing planetesimals and planetary embryos when Jupiter has reached its full size and there are no influx of pebbles. We find that the terrestrial planet analogues have feeding zones that display a trend with semi-major axis, suggesting that the planets accrete mostly local material and there is very little mixing in the disc. In addition, the Vesta analogues originate from the asteroid belt in the region close to Vesta's current orbit. The distinct feeding zones of the terrestrial planet analogues and the formation region of Vesta analogues in the asteroid belt is encouraging because it means that the Earth, Mars and Vesta can be distinct in their isotopic compositions — consistent with isotopic data — if the solids in the inner Solar System are isotopically heterogeneous. We further suggest that (1) isotopic gradients should have been present in the inner Solar System before the formation of the planetesimals, and (2) the inner Solar System bodies should have formed via local accretion, such that the isotopic heterogeneity is preserved and is reflected in the distinct isotopic compositions of Earth, Mars and Vesta.

4.2 Future directions

Finally, we list several potential directions that future research could undertake to further our understanding of planet formation in our Solar System as well as other exoplanet systems.

- Protoplanetary disc models: Since the construction of plausible planet formation models is dependent on the current understanding of protoplanetary disc models, it would be useful to delve into the study of protoplanetary discs. A good understanding of protoplanetary discs could for example aid in understanding how, when and where planetesimals form in the disc and the expected size-frequency distribution of the planetesimals (e.g., Chambers, 2010; Johansen et al., 2014).
- High-resolution simulations: *N*-body simulations run on graphics processing units (GPU) could achieve higher resolution with shorter computing time. Re-examining the current terrestrial planet formation models with *N*-body codes written for GPUs (e.g., GENGA; Grimm and Stadel, 2014) could push the current limits and perhaps reveal new information (e.g., Woo et al., 2021).

- Cosmochemistry data: The building blocks of the Earth remain an unresolved puzzle. Accurate determination of isotopic anomalies and elemental abundances of a wide variety of meteorite samples with high-precision equipment coupled with modelling of geochemical and geophysical processes could help in cracking the code.
- Stellar/Galaxy cluster evolution: On a larger scale, the abundances of short-lived radionuclides (SLR) in our Solar System obtained from models of the evolution of the Sun's birth cluster (e.g., Fujimoto et al., 2018; Portegies Zwart et al., 2018) can be compared to the measured abundances of the daughter isotopes that are radioactive decay products of the SLRs. These models could perhaps be employed to study the distribution of nucleosynthetic isotopes in different regions of the protoplanetary disc.

A Monte Carlo mixing model

Here we describe how we computed the composition of the Earth and Mars as a mixture of chondrites (and angrite meteorites; Fitoussi et al., 2016) using a Monte Carlo mixing model based on the work of Dauphas (2017). The goal of the mixing model is to derive the best-fit compositions of the Earth and Mars that is consistent with the isotopic anomalies measured for Δ^{17}O, ε^{50}Ti, ε^{54}Cr, ε^{62}Ni and ε^{92}Mo. Our model differs from the original model of Dauphas (2017) in the following ways: (1) we expanded the list of carbonaceous chondrites used in the model to include CM and CR chondrites, (2) we split the enstatite chondrites group into its two components: EL and EH, and (3) we use the ε^{62}Ni isotope instead of ε^{64}Ni.

A.1 Model inputs

Table A.1: Measured Δ^{17}O, ε^{50}Ti, ε^{54}Cr, ε^{62}Ni and ε^{92}Mo isotopic anomalies of Mars and various meteorite types considered in our Monte Carlo mixing model. The isotopic anomalies for the Earth is 0. All values taken from the compilation of Dauphas (2017) except for ε^{62}Ni which we source from the compilation of Burkhardt et al. (2017).

	Δ^{17}O	ε^{50}Ti	ε^{54}Cr	ε^{62}Ni	ε^{92}Mo
Mars	0.27 ± 0.03	−0.54 ± 0.17	−0.19 ± 0.04	0.040 ± 0.022	0.20 ± 0.53
EL	−0.01 ± 0.07	−0.28 ± 0.06	0.06 ± 0.04	−0.025 ± 0.044	0.30 ± 0.74
EH	−0.03 ± 0.10	−0.10 ± 0.02	0.04 ± 0.08	0.026 ± 0.021	0.36 ± 0.43
H	0.72 ± 0.05	−0.61 ± 0.17	−0.38 ± 0.03	−0.065 ± 0.044	0.78 ± 0.26
L	1.03 ± 0.04	−0.63 ± 0.02	−0.39 ± 0.07	−0.051 ± 0.020	0.61 ± 0.62
LL	1.19 ± 0.06	−0.65 ± 0.04	−0.43 ± 0.04	−0.076 ± 0.013	0.87 ± 1.13
CI	0.39 ± 0.10	1.83 ± 0.09	1.57 ± 0.03	0.198 ± 0.057	0.82 ± 0.41
CO	−4.32 ± 0.26	3.76 ± 0.66	0.75 ± 0.21	0.113 ± 0.018	2.00 ± 1.40
CV	−3.62 ± 0.48	3.64 ± 0.29	0.87 ± 0.04	0.103 ± 0.038	2.59 ± 0.67
CM	−2.92 ± 0.04	3.01 ± 0.09	1.10 ± 0.18	0.095 ± 0.030	5.71 ± 0.94
CR	−1.48 ± 0.55	2.35 ± 0.04	1.32 ± 0.08	0.095 ± 0.035	3.00 ± 1.80
Angrites	−0.11 ± 0.11	−1.15 ± 0.02	−0.41 ± 0.09	0.028 ± 0.082	−0.14 ± 0.75

The reservoirs we include in our model are the EL, EH, CI, CO, CV, CM, CR, H, L and LL chondrites, and the angrite meteorite (a type of achondrite). Other than the Δ^{17}O, ε^{50}Ti, ε^{54}Cr, ε^{62}Ni and ε^{92}Mo values for these meteorites, the model also requires the respective uncertainties of these isotopic anomalies and the concentration of these elements in the meteorites. In addition, the model also takes in the mass fraction of the five elements O, Ti, Cr, Ni and Mo in the mantle of the Earth and Mars that was delivered at each stage of the accretion process. We follow Dauphas (2017) and assume that the accretion process comprises

TABLE A.2: Measured O, Ti, Cr, Ni and Mo elemental concentrations of the meteorites considered in our Monte Carlo mixing model. The values for chondritic meteorites are from Wasson and Kallemeyn (1988) while the values for angrites are from Fitoussi et al. (2016).

	O (mg/g)	Ti (μg/g)	Cr (mg/g)	Ni (mg/g)	Mo (ng/g)
EL	310	580	3.05	13.0	1131
EH	280	450	3.15	17.5	1131
CI	460	420	2.65	10.7	920
CO	370	780	3.55	14.0	1900
CV	370	980	3.60	13.4	2100
CM	432	580	3.05	12.0	1500
CR	420	647	3.75	13.6	1210
H	357	600	3.66	16.0	1700
L	377	630	3.88	12.0	1300
LL	400	620	3.74	10.2	1100
Angrites	359	867	3.78	14.9	1523

TABLE A.3: Mass fractions of elements O, Ti, Cr, Ni and Mo present in the mantle of the Earth and Mars at various accretion stages. The values are from Dauphas (2017).

	O		Ti		Cr		Ni		Mo	
	Earth	Mars	Earth	Mars	Earth	Mars	Earth	Mars	Earth	Mars
Stage 1	0.6	0.6	0.6	0.6	0.447	0.365	0.046	0	0	0
Stage 2	0.395	0.392	0.395	0.392	0.546	0.632	0.916	0.849	0.873	0.985
Stage 3	0.005	0.008	0.005	0.008	0.007	0.003	0.038	0.151	0.127	0.015

three distinct stages. The inputs for our mixing model are summarised in Tables A.1, A.2 and A.3.

A.2 Governing equations

The isotopic composition (Δ^{17}O, ε^{50}Ti, ε^{54}Cr, ε^{62}Ni and ε^{92}Mo) of the Earth and Mars, a quantity to be computed in our model, is given by (Dauphas, 2017)

$$\varepsilon_{\text{mantle,comp}} = \sum_j X_j \frac{\sum_i f_{i,j} C_i \varepsilon_i}{\sum_i f_{i,j} C_i}, \tag{A.1}$$

where X_j is the mass fraction of the element that was accreted onto the planet in stage j ($\sum_j X_j = 1$), $f_{i,j}$ is the mass fraction of meteorite reservoir i that was accreted onto the planet in stage j ($\sum_i f_{i,j} = 1$), C_i is the concentration of the element in reservoir i, and ε_i is the measured isotopic composition of reservoir i. All quantities are fixed and given in Tables A.1, A.2 and A.3 except for $f_{i,j}$ which we leave as a free parameter.

In our model, Eq. A.2 is decomposed into two parts, representing the contribution by EL chondrites, and all reservoirs other than EL chondrites. The corresponding equations are

$$
\begin{aligned}
\varepsilon_{\mathrm{EL}} &= \sum_j X_j \frac{f_{j,\mathrm{EL}} C_{\mathrm{EL}} \varepsilon_{\mathrm{EL}}}{f_{j,\mathrm{EL}} C_{\mathrm{EL}} + (1 - f_{j,\mathrm{EL}}) \sum_i f_{i,j,\mathrm{nEL}} C_{i,\mathrm{nEL}}}, \\
\varepsilon_{\mathrm{nEL}} &= \sum_j X_j \frac{(1 - f_{j,\mathrm{EL}}) \sum_i f_{i,j,\mathrm{nEL}} C_{i,\mathrm{nEL}} \varepsilon_{i,\mathrm{nEL}}}{f_{j,\mathrm{EL}} C_{\mathrm{EL}} + (1 - f_{j,\mathrm{EL}}) \sum_i f_{i,j,\mathrm{nEL}} C_{i,\mathrm{nEL}}},
\end{aligned} \tag{A.2}
$$

where $\varepsilon_{\mathrm{EL}} + \varepsilon_{\mathrm{nEL}} = \varepsilon_{\mathrm{mantle,comp}}$. The uncertainties for $\varepsilon_{\mathrm{EL}}$ and $\varepsilon_{\mathrm{nEL}}$ are computed as

$$
\begin{aligned}
\sigma_{\varepsilon_{\mathrm{EL}}} &= \sum_j X_j \frac{f_{j,\mathrm{EL}} C_{\mathrm{EL}}}{f_{j,\mathrm{EL}} C_{\mathrm{EL}} + (1 - f_{j,\mathrm{EL}}) \sum_i f_{i,j,\mathrm{nEL}} C_{i,\mathrm{nEL}}}, \\
\sigma_{\varepsilon_{\mathrm{nEL}}} &= \sum_j X_j \frac{(1 - f_{j,\mathrm{EL}}) \sum_i f_{i,j,\mathrm{nEL}} C_{\mathrm{EL}}}{f_{j,\mathrm{EL}} C_{\mathrm{EL}} + (1 - f_{j,\mathrm{EL}}) \sum_i f_{i,j,\mathrm{nEL}} C_{i,\mathrm{nEL}}},
\end{aligned} \tag{A.3}
$$

Combining the uncertainties for the EL and non-EL reservoirs gives the total uncertainty in $\varepsilon_{\mathrm{mantle,comp}}$:

$$
\sigma_{\varepsilon_{\mathrm{mantle,comp}}} = \sqrt{\left(\frac{\sqrt{\sum_i f_{i,j,\mathrm{nEL}} C_{i,\mathrm{nEL}} \sigma^2_{i,\mathrm{nEL}}}}{\sum_i f_{i,j,\mathrm{nEL}} C_{i,\mathrm{nEL}}} \right)^2 \sigma^2_{\varepsilon_{\mathrm{nEL}}} + \sigma^2_{\mathrm{EL}} \sigma^2_{\varepsilon_{\mathrm{EL}}}}. \tag{A.4}
$$

Here, $\sigma_{i,\mathrm{nEL}}$ and σ_{EL} are the uncertainties in the isotopic compositions of the meteoritic reservoirs listed in Table A.1.

Finally, the chi-square statistic χ^2 is computed as

$$
\chi^2 = \frac{\left(\varepsilon_{\mathrm{mantle,comp}} - \varepsilon_{\mathrm{mantle,meas}}\right)^2}{\left(\frac{1}{2}\sigma_{\varepsilon_{\mathrm{mantle,comp}}}\right)^2 + \left(\frac{1}{2}\sigma_{\varepsilon_{\mathrm{mantle,meas}}}\right)^2}, \tag{A.5}
$$

where $\varepsilon_{\mathrm{mantle,meas}}$ are the measured isotopic compositions of the Earth (or Mars) and $\sigma_{\varepsilon_{\mathrm{mantle,meas}}}$ are the corresponding uncertainties (Table A.1).

A.3 Model algorithm

The first step of the computation concerns the initialisation of the isotopic compositions (Eq. A.2), their corresponding uncertainties (Eq. A.3 and A.4) and the chi-square values (Eq. A.5). For the free parameter $f_{i,j}$, we chose at random $f_{1,\mathrm{EL}} = 1$, $f_{2,\mathrm{EL}} = 0.2$, $f_{3,\mathrm{EL}} = 1$, and $f_{i,j,\mathrm{nEL}} = 0$. With these initial values we compute $\varepsilon_{\mathrm{mantle,comp}}$, $\sigma_{\varepsilon_{\mathrm{mantle,comp}}}$ and χ^2_{old}.

We next proceed to compute new values of $f_{i,j}$ using a Box-Muller transform. We made the assumption that $f_{i,j}$ are distributed normally with a standard deviation of 0.005. As the Box-Muller transform generates two variables at once, we compute the new values of $f_{i,j}$ in pairs, according to

$$
\begin{aligned}
f_{i,j,\mathrm{new}} &= f_{i,j,\mathrm{old}} + 0.005 z_1, \\
f_{i,j,\mathrm{new}} &= f_{i,j,\mathrm{old}} + 0.005 z_2,
\end{aligned} \tag{A.6}
$$

where z_1 and z_2 are given by

$$
\begin{aligned}
z_1 &= \sqrt{-2 \log u} \sin(2\pi v), \\
z_2 &= \sqrt{-2 \log u} \cos(2\pi v).
\end{aligned} \tag{A.7}
$$

Here, u and v are selected at random from a uniform distribution with interval [0,1). We also imposed the following constraints for the values of $f_{i,j}$ generated by the Box-Muller transform:

$$\begin{aligned} 0 \le f_{j,\mathrm{EL}} &\le 1, \\ 0 \le f_{i,j,\mathrm{nEL}} &\le 1, \\ \sum_i f_{i,j,\mathrm{nEL}} &\le 1. \end{aligned} \tag{A.8}$$

With the new values of $f_{i,j}$ we compute $\varepsilon_{\mathrm{mantle,comp}}$, $\sigma_{\varepsilon_{\mathrm{mantle,comp}}}$ and the corresponding value of χ^2_{new}. This is then followed by an acceptance test according to the Metropolis-Hastings algorithm (Metropolis et al., 1953) with the acceptance ratio computed as

$$\alpha' = \exp\left(-0.5\chi^2_{\mathrm{new}} + 0.5\chi^2_{\mathrm{old}}\right). \tag{A.9}$$

We accept the new $f_{i,j}$ values and update χ^2_{old} with χ^2_{new} if the value of y selected at random from a uniform distribution ranging from [0,1) fulfils the condition $y < \alpha'$.

Finally, we repeat the algorithm described in the previous paragraph over 10^6 iterations for Earth and 2×10^6 iterations for Mars. We excluded the output from the first 2×10^4 iterations for the Earth and 2×10^5 iterations for Mars when the system has yet to reach equilibrium before searching for the best-fit combination of $f_{i,j}$ which gives the lowest value of χ^2. We also repeated the same Monte Carlo simulation 20 times to obtain other best-fit combinations of $f_{i,j}$.

A.4 Model output

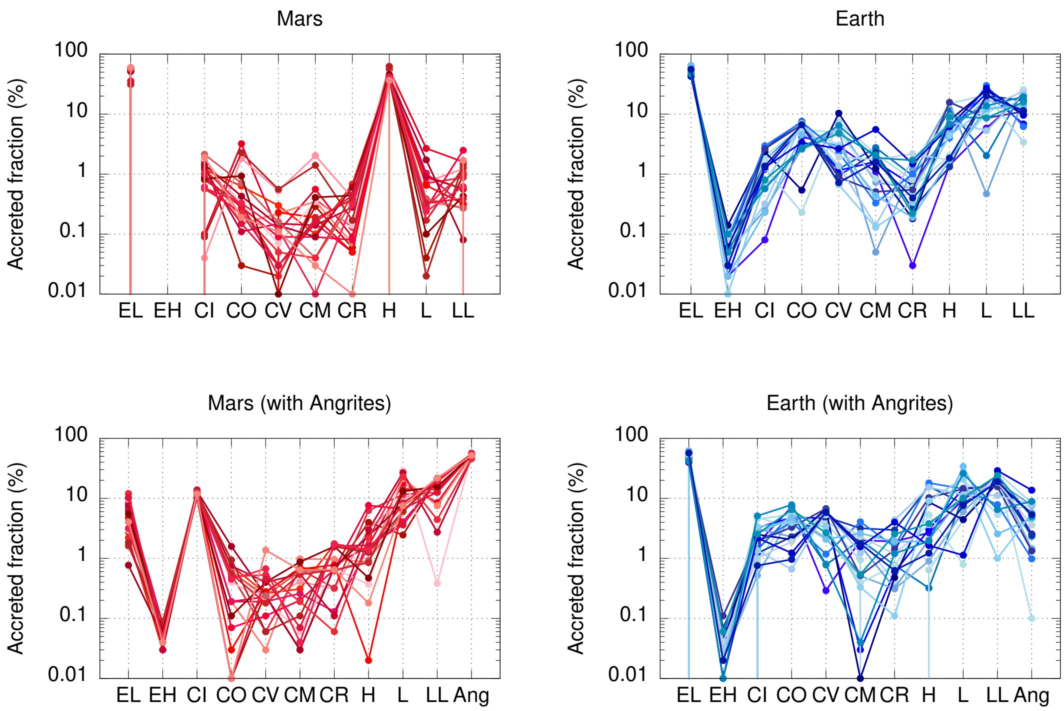

FIGURE A.1: Contribution of various meteorite types to the composition of Earth and Mars computed from our mixing model. Shown here are the best-fit compositions obtained from 20 simulations. The top panels shows the results for the simulations where only chondrites are considered while the bottom panels shows the results when we include angrites into the list of potential building blocks.

Fig. A.1 shows the best-fit compositions of the Earth and Mars obtained from our mixing model. If we only consider chondritic reservoirs, the mixing model outputs the following combination for the Earth and Mars:

- Earth = (52 ± 6)% EC + (36 ± 4)% OC + (12 ± 2)% CC
- Mars = (53 ± 9)% EC + (45 ± 8)% OC + (2 ± 1)% CC

The major contributors to the composition of Earth are EL (52%), CO (5%), CV (3%), H (7%), L (15%) and LL (15%) chondrites. For Mars, the major contributors are EL (53%) and H (43%) chondrites. In computing these numbers, we have taken the average and the standard deviation from the outputs of 20 Monte Carlo simulations. Our results are consistent with those from previous studies (e.g., Sanloup et al., 1999; Tang and Dauphas, 2014; Dauphas, 2017; Brasser et al., 2018).

If we include angrites to the mix, the model gives the following results instead:

- Earth = (48 ± 7)% EC + (34 ± 4)% OC + (13 ± 2)% CC + (5 ± 3)% angrites
- Mars = (5 ± 3)% EC + (29 ± 2)% OC + (14 ± 1)% CC + (52 ± 3)% angrites

In this case the major contributors are EL (48%), CO (4%), CV (4%), H (6%), L (12%), LL (16%) and angrites (5%) for the Earth, and EL (5%), CI (12%), L (12%), LL (15%) and angrites (52%) for Mars. The model gives a very different composition for Mars when angrites are considered: Angrites are now the favoured major contributor, the contribution of EC is drastically reduced and the contribution of CC is increased. This outcome is also consistent with the results of Fitoussi et al. (2016). However, this result should not be overinterpreted mainly because the bulk chemical composition of the angrite parent body is not well constrained (as is also the case with other achondrites) and thus it is unclear if the measured isotopic anomalies of the angrites that we use in our mixing model is truly representative of that of its parent body.

From our mixing model study, we show that it is always possible to find a combination of chondrites (and achondrites) which, when mixed in the correct proportion, can reproduce the isotopic compositions of the Earth and Mars. The large uncertainties in the measurement of some isotopic anomalies (e.g., ε^{92}Mo) can affect the mixing model output for the contribution of each chondritic (and achondritic) reservoir. It is therefore imperative to identify new constraints (e.g., major element abundance ratio) to be incorporated into the model in order to obtain more conclusive results.

B Numerical methods

B.1 Gas disc model

The gas disc model employed in our simulations is based on the model of Ida et al. (2016). The accretion rate of the gas onto the central star (the Sun in our case) is assumed to occur at a steady rate given by

$$\dot{M}_* = 3\pi\alpha\Sigma_\mathrm{g} H_\mathrm{g}^2 \Omega_\mathrm{K}, \tag{B.1}$$

where Σ_g is the gas surface density, H_g is the disc scale height and Ω_K is the Keplerian frequency. The disc α-viscosity α was set to 10^{-3} and assumed to be constant throughout (Shakura and Sunyaev, 1973). It is given by

$$\alpha = \nu/(c_\mathrm{s}^2\Omega_\mathrm{K}), \tag{B.2}$$

where ν is the gas viscosity and c_s is the sound speed. As a result, the gas surface density is comparable to that of the MMSN. The scale height of the disc H_g is a function of the temperature T and the sound speed c_s via $H_\mathrm{g} = c_\mathrm{s}/\Omega_\mathrm{K}$, where $c_\mathrm{s} = (\gamma k_\mathrm{B} T/\mu m_\mathrm{p})$. The heat capacity ratio γ is set to 7/5, k_B is the Boltzmann constant, $\mu = 2.3$ is the mean atomic mass of the gas and m_p is the mass of the proton. In the simulations, the gas accretion rate varies with time according to Hartmann et al. (1998)

$$\log\left(\frac{\dot{M}_*}{M_\odot\ \mathrm{yr}^{-1}}\right) = -8 - \frac{7}{5}\log\left(\frac{t}{1\ \mathrm{Myr}} + 0.1\right) \tag{B.3}$$

where the extra 0.1 Myr was added to avoid the logarithmic singularity (Bitsch et al., 2015).

The temperature in different regions of the disc is predominantly dictated by the heating source. In general, viscous heating dominates the inner region close to the star while stellar irradiation has a stronger influence in the far away regions. At the midplane, the disc temperature is given by $T = \max(T_\mathrm{vis}, T_\mathrm{irr})$, where T_vis and T_irr are temperatures in the viscous region and irradiative region, respectively. The empirically fitted expressions for T_vis and T_irr based on the constant-opacity disc model of Garaud and Lin (2007) are

$$\begin{aligned} T_\mathrm{vis} &= T_{0\nu}\alpha_3^{-1/5}\dot{M}_{*8}^{2/5}\left(\frac{r}{1\ \mathrm{au}}\right)^{-9/10}\ \mathrm{K}, \\ T_\mathrm{irr} &= 150\left(\frac{r}{1\ \mathrm{au}}\right)^{-3/7}\ \mathrm{K}, \end{aligned} \tag{B.4}$$

where $T_{0\nu}$ is the initial temperature at 1 au and r is the distance to the Sun. The power exponents in the equation are derived analytically. We additionally defined the following normalised parameters

$$\alpha_3 \equiv \frac{\alpha}{10^{-3}}, \tag{B.5}$$

$$\dot{M}_{*8} \equiv \frac{\dot{M}_*}{10^{-8}\ M_\odot\ \mathrm{yr}^{-1}}. \tag{B.6}$$

With the disc temperature profiles defined, the reduced disc scale height $h_\mathrm{g} = H_\mathrm{g}/r$ can thus be computed as

$$\begin{aligned} h_\mathrm{g,vis} &= 0.034 \left(\frac{T_{0v}}{200\ \mathrm{K}}\right)^{1/2} \alpha_3^{-1/10} \dot{M}_{*8}^{1/5} \left(\frac{r}{1\ \mathrm{au}}\right)^{1/20}, \\ h_\mathrm{g,irr} &= 0.029 \left(\frac{r}{1\ \mathrm{au}}\right)^{2/7}. \end{aligned} \tag{B.7}$$

The actual reduced scale height of the disc is $h_\mathrm{g} = \max(h_\mathrm{g,vis}, h_\mathrm{g,irr})$. This gives the disc a flaring shape in the irradiative region and a constant scale height in the viscous region. Equations (B.1), (B.4) and (B.7) are then combined to compute the gas surface density in the viscous and irradiative regions

$$\begin{aligned} \Sigma_\mathrm{g,vis} &= 1320 \left(\frac{T_{0v}}{200\ \mathrm{K}}\right)^{-1} \alpha_3^{-4/5} \dot{M}_{*8}^{3/5} \left(\frac{r}{1\ \mathrm{au}}\right)^{-3/5} \mathrm{g\ cm^{-2}}, \\ \Sigma_\mathrm{g,irr} &= 1785 \alpha_3^{-1} \dot{M}_{*8} \left(\frac{r}{1\ \mathrm{au}}\right)^{-15/14} \mathrm{g\ cm^{-2}}. \end{aligned} \tag{B.8}$$

The corresponding pressure gradient $\mathrm{d}\ln P/\mathrm{d}\ln r$ in the viscous and irradiative regimes are

$$\begin{aligned} \left(\frac{\mathrm{d}\ln P}{\mathrm{d}\ln r}\right)_\mathrm{vis} &= \frac{51}{20}, \\ \left(\frac{\mathrm{d}\ln P}{\mathrm{d}\ln r}\right)_\mathrm{irr} &= \frac{39}{14}. \end{aligned} \tag{B.9}$$

Finally, the boundary between the viscous and irradiative region, determined by $T_\mathrm{vis} = T_\mathrm{irr}$, occurs at

$$\begin{aligned} r_\mathrm{vis/irr} &= \left(\frac{T_{0v}}{150\ \mathrm{K}}\right)^{70/33} \alpha_3^{-14/33} \dot{M}_{*8}^{28/33} \\ &\approx 1.84\ \alpha_3^{-14/33} \dot{M}_{*8}^{28/33}\ \mathrm{au}. \end{aligned} \tag{B.10}$$

B.2 Disc-induced orbital evolution

The gas disc exerts torques and tidal forces on all the planetary bodies (with mass M and radius R) embedded in the disc which result in a combined effect of radial migration and the damping of the orbital eccentricity e and orbital inclination I. Low-mass planetary bodies, i.e., those that are unable to clear the surrounding gas, experience type I migration (Tanaka et al., 2002) while massive bodies experience type II migration (Lin and Papaloizou, 1986). The computation of the torques and the direction of migration is based on the prescriptions of Coleman and Nelson (2014). The normalised torque is given by

$$\frac{\gamma\Gamma}{\Gamma_0} = \frac{\Gamma_\mathrm{C}}{\Gamma_0} F_\mathrm{C} + \frac{\Gamma_\mathrm{L}}{\Gamma_0} F_\mathrm{L} \tag{B.11}$$

where Γ_C and Γ_L are the corotation and Lindblad torques respectively (Paardekooper et al., 2011) and

$$\Gamma_0 = \left(\frac{M}{M_*}\right)^2 h_\mathrm{g}^{-2} \Sigma_\mathrm{g} \Omega_\mathrm{K}^2 \tag{B.12}$$

is a normalisation constant. The factors F_L and F_C are defined as (Cresswell and Nelson, 2008; Fendyke and Nelson, 2014)

$$\begin{aligned} \ln F_\mathrm{C} &= -\frac{e}{e_\mathrm{f}}, \\ \frac{1}{F_\mathrm{L}} &= P_e + \mathrm{sign}(P_e)(0.07\hat{I} + 0.085\hat{I}^4 - 0.08\hat{e}^2\hat{I}^2), \end{aligned} \tag{B.13}$$

where $e_\mathrm{f} = 0.01 + \frac{1}{2}h_\mathrm{g}$, $\hat{e} = e/h_\mathrm{g}$, $\hat{I} = \sin(I)/h_\mathrm{g}$ and

$$P_\mathrm{e} = \frac{1 + (0.444\hat{e})^{1/2} + (0.352\hat{e})^6}{1 - (0.495\hat{e})^4}.$$

The eccentricity damping timescale $\tau_e = -e/\dot{e}$ is

$$\tau_e = 1.282 t_\mathrm{wav}\left(1 - 0.14\hat{e}^2 + 0.06\hat{e}^3 + 0.18\hat{e}^2\hat{I}^2\right), \tag{B.14}$$

where the wave timescale is (Tanaka and Ward, 2004)

$$t_\mathrm{wav} = \left(\frac{M_*}{M}\right)\left(\frac{M_*}{\Sigma_\mathrm{g}R^2}\right)h_\mathrm{g}^4\Omega_K^{-1}. \tag{B.15}$$

The inclination damping time scale $\tau_I = -I/(dI/dt)$ is

$$\tau_I = 1.838 t_\mathrm{wav}(1 - 0.30\hat{I}^2 + 0.24\hat{I}^3 + 0.14\hat{e}^2\hat{I}^2). \tag{B.16}$$

For planetary bodies in the type I migration regime, the migration timescale is defined as $\tau_m = -L/\Gamma$ where L and Γ are the angular momentum and the torque. We compute the migration timescale as

$$\tau_\mathrm{mig,1} = -\frac{t_\mathrm{wav}\Gamma_0}{h_\mathrm{g}^2\Gamma}, \tag{B.17}$$

in the simulations. For bodies in the type II regime, the migration timescale is computed as

$$\tau_\mathrm{mig,2} = \frac{2R^2}{3\nu}\max\left(1, \frac{M}{2\pi\Sigma_\mathrm{g}R^2}\right). \tag{B.18}$$

The first term in the parentheses corresponds to the case when the planet is less massive than the disc interior to its orbit and the migration occurs on the disc's viscous evolution timescale of $\tau_\mathrm{mig,2} \simeq (2/3)(R^2/\nu)$ (Lin and Papaloizou, 1986), whereas the second term corresponds to the opposite case where the planet is more massive and thus the migration occurs on a longer timescale $\tau_\mathrm{mig,2} \simeq M/\dot{M}_*$ (Hasegawa and Ida, 2013).

B.3 Gas envelope accretion for massive planets

Gas accretion commences for planetary bodies that fulfil two criteria: (1) they have reached a critical core mass, and (2) the accretion rate of solids onto said planetary core is sufficiently low that it does not affect the cooling and contraction of the gas envelope. The critical core mass of a planetary body is given by (Ikoma et al., 2000)

$$M_\mathrm{crit} = 10\left(\frac{\dot{M}_\mathrm{core}}{10^{-6}M_\mathrm{E}\ \mathrm{yr}^{-1}}\right)^{1/4} M_\mathrm{E}, \tag{B.19}$$

where the core accretion rate is equal to the pebble accretion rate of the planetary body $\dot{M}_\mathrm{core} = \dot{M}$ (see Eq. 2.1). The collapse and accretion of the gas envelope then proceeds on the Kelvin-Helmholtz timescale (Ikoma et al., 2000) according to

$$\tau_\mathrm{KH} = 10^9\left(\frac{M}{M_\mathrm{E}}\right)^{-3}\ \mathrm{yr}. \tag{B.20}$$

This process of runaway gas accretion is bounded by the gas accretion rate throughout the disc $\dot{M}_*$. Gas accretion ceases when the Hill radius of the planet is approximately equal to that of the disc scale height. Taking all these effects into account, the gas accretion rate onto the planetary core is written as

$$\dot{M}_{\mathrm{g}} = \min\left[\frac{M}{\tau_{\mathrm{KH}}}, \dot{M}_{*}\exp\left(-\frac{M}{M_{\mathrm{H}}}\right)\right], \tag{B.21}$$

where $M_{\mathrm{H}} = 3(h_{\mathrm{g}}/R)^3 M_*$ is the required planetary mass for its Hill radius to be comparable to the disc scale height. The gas accretion rate is limited to the Bondi accretion rate of

$$\dot{M}_{\mathrm{g,B}} = \frac{4\pi\rho_{\mathrm{g}} G^2 M^2}{c_{\mathrm{s}}^3}, \tag{B.22}$$

where $\rho_g \sim \Sigma_g/(\sqrt{2\pi}h_g)$ is the gas disc's density and G is the gravitational constant. We keep track of the amount of mass in solids and in gas accreted by the planet.

C Depleted disc model simulations with higher solid surface density

In our depleted disc model simulations adopting a fixed value (MMSN) for the solid surface density (Chapter 3) we find that the planets that formed in the terrestrial region have masses that are lower than the current terrestrial planets. This issue could be resolved by increasing the surface density of the disc so that there is more mass in the disc to form more massive planets. We carried out additional simulations with a higher solid surface density (1.5 and/or 2 times the MMSN value) for the cases where the initial mass in the solid disc is less than $\sim 2\ M_{\mathrm{E}}$. Fig. C.1 shows the initial conditions of our additional simulations. In most cases, the initial mass of solids in the disc is now well over $\sim 2\ M_{\mathrm{E}}$, sufficient to form the terrestrial planets.

With the disc's solid surface density increased, the final mass of planets in the terrestrial region are now closer to the current mass of the terrestrial planets (Fig. C.2). In particular, planets at around 1 au now have masses comparable to that of the Earth. However, planets that formed in the region around 1.5 au tend to be more massive than Mars. From the initial conditions that we investigated here, we find that increasing the solid surface density produces more Venus and Earth analogues but less Mars analogues. A larger degree of mass depletion is thus required to form planets around 1.5 au with masses equivalent to that of Mars. For example, a mass depletion of $> 95\%$ is needed for the case of $r_{\mathrm{dep}} = 1.5$ au and a mass depletion of $> 75\%$ up to about 95% is needed for the case of $r_{\mathrm{dep}} = 1.0$ au.

As the planets are now more massive on average, we observe an increase in the values of S_{m} and S_{H} (top panel of Fig. C.3). The results for the concentration parameter S_{c} and AMD of the terrestrial planet systems are, however, similar to the outcomes for simulations with MMSN surface density (bottom panel of Fig. C.3).

We also find the same trend of correlated feeding zones with semi-major axis for the Venus and Earth analogues and a large variation in the feeding zones of Mars analogues (Fig. C.4).

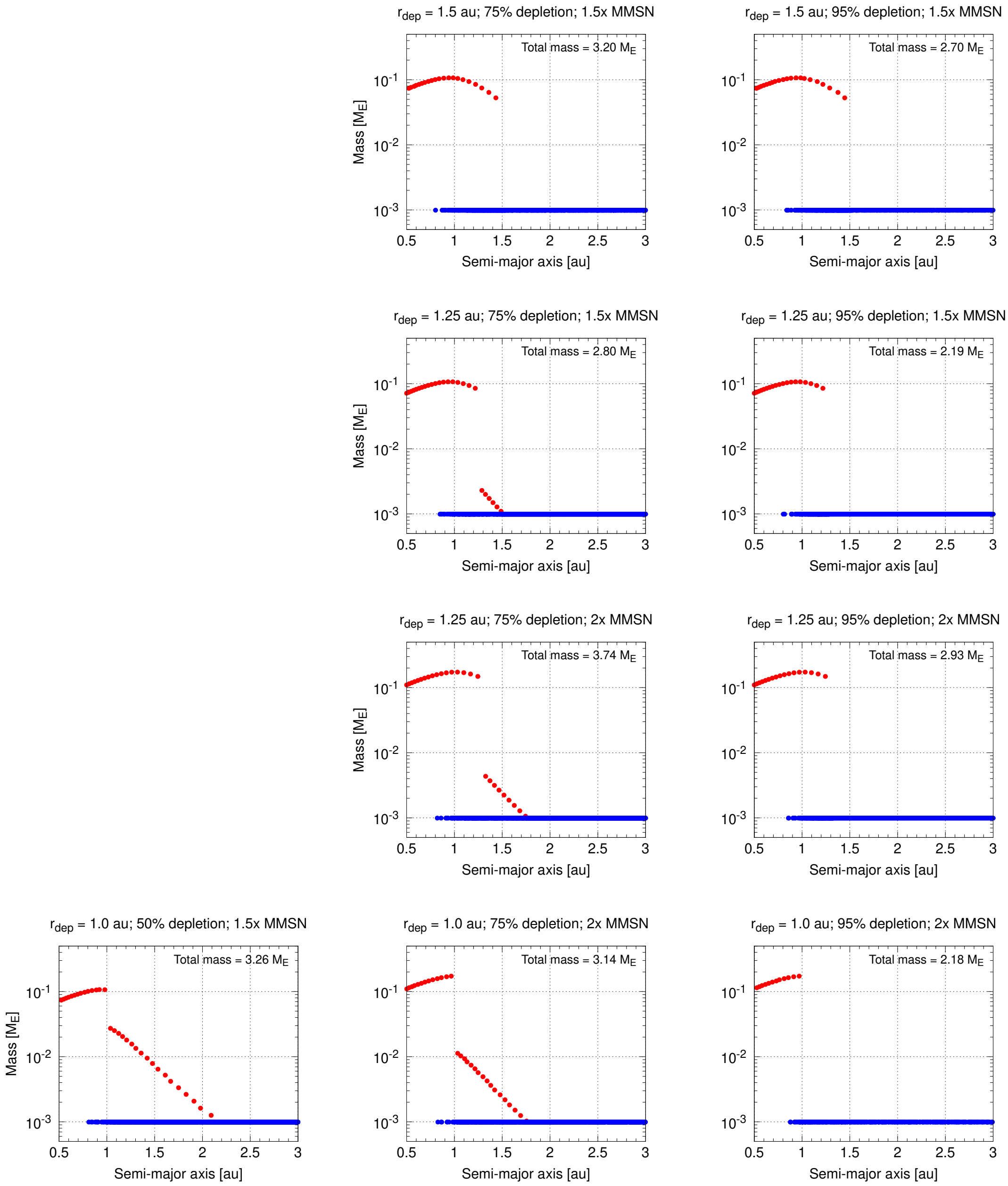

FIGURE C.1: Initial mass and semi-major axis distribution of planetary embryos (red) and planetesimals (blue) for additional depleted disc model simulations starting with higher solid surface density.

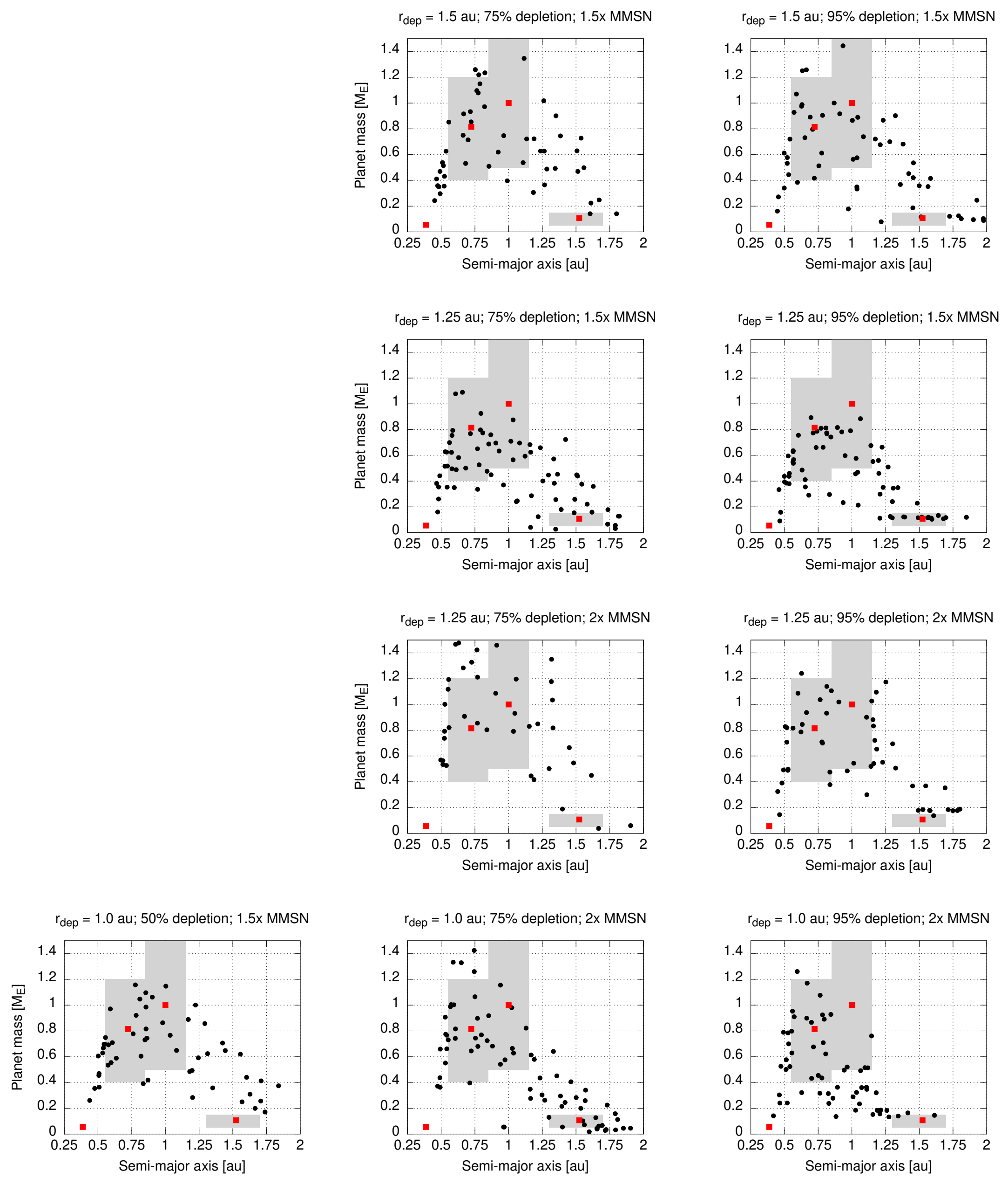

FIGURE C.2: Distribution of final planet mass versus semi-major axis for simulations starting with higher solid surface density. Red squares are the current terrestrial planets, black circles are planets that formed in the simulations, and grey regions indicate the range within which planets are considered good terrestrial planet analogues.

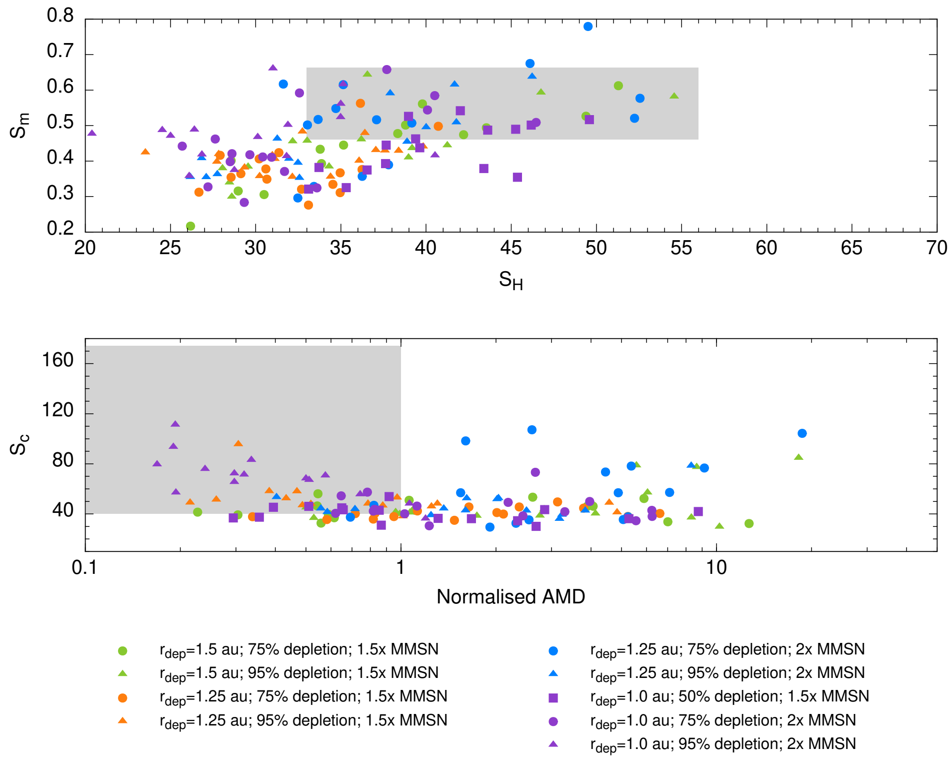

FIGURE C.3: Top panel: Mass in largest planet as a fraction of the total mass of the planetary system S_m versus the mean spacing parameter S_H in units of the mutual Hill sphere. Bottom panel: Mass concentration parameter S_c versus the angular momentum deficit (AMD) normalised to the current Solar System value. Grey regions encompass the current values of the inner Solar System and the 2σ range.

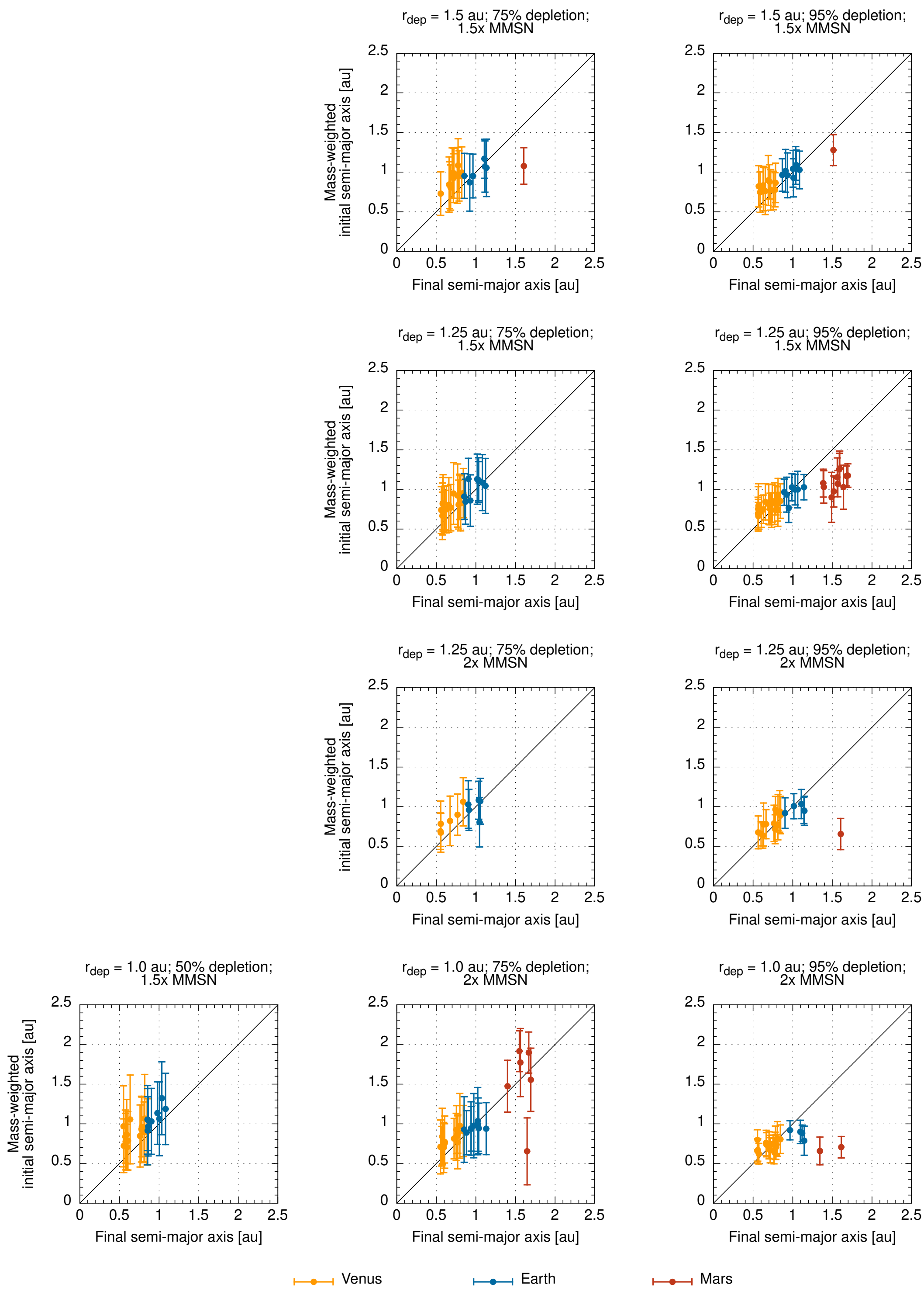

FIGURE C.4: Feeding zones of the Venus, Earth an Mars analogues versus their final semi-major axis from additional depleted disc model simulations starting with higher solid surface density. Black lines correspond to the equation $y = x$.

Bibliography

Abod, C.P., Simon, J.B., Li, R., Armitage, P.J., Youdin, A.N., Kretke, K.A., 2019. The mass and size distribution of planetesimals formed by the streaming instability. II. The effect of the radial gas pressure gradient. Astrophys. J. 883, 192. doi: 10.3847/1538-4357/ab40a3.

Agee, C.B., Wilson, N.V., McCubbin, F.M., Ziegler, K., Polyak, V.J., Sharp, Z.D., Asmerom, Y., Nunn, M.H., Shaheen, R., Thiemens, M.H., Steele, A., Fogel, M.L., Bowden, R., Glamoclija, M., Zhang, Z., Elardo, S.M., 2013. Unique meteorite from early Amazonian Mars: Water-rich basaltic breccia Northwest Africa 7034. Science 339, 780–785. doi: 10.1126/science.1228858.

Ahrens, L.H., Willis, J.P., Erlank, A.J., 1973. The chemical composition of Kainsaz and Efremovka. Meteoritics 8, 133–139. doi: 10.1111/j.1945-5100.1973.tb00148.x.

Alexander, C.M.O.D., 2019. Quantitative models for the elemental and isotopic fractionations in the chondrites: The non-carbonaceous chondrites. Geochim. Cosmochim. Acta 254, 246–276. doi: 10.1016/j.gca.2019.01.026.

Amelin, Y., Kaltenbach, A., Iizuka, T., Stirling, C.H., Ireland, T.R., Petaev, M., Jacobsen, S.B., 2010. U-Pb chronology of the solar system's oldest solids with variable 238U/235U. Earth Planet. Sci. Lett. 300, 343–350. doi: 10.1016/j.epsl.2010.10.015.

Anders, E., Grevesse, N., 1989. Abundances of the elements: Meteoritic and solar. Geochim. Cosmochim. Acta 53, 197–214. doi: 10.1016/0016-7037(89)90286-X.

Andreasen, R., Sharma, M., 2007. Mixing and homogenization in the early Solar System: Clues from Sr, Ba, Nd and Sm isotopes in meteorites. Astrophys. J. 665, 874. doi: 10.1086/518819.

Badro, J., Fiquet, G., Guyot, F., Gregoryanz, E., Occelli, F., Antonangeli, D., d'Astuto, M., 2007. Effect of light elements on the sound velocities in solid iron: Implications for the composition of Earth's core. Earth Planet. Sci. Lett. 254, 233–238. doi: 10.1016/j.epsl.2006.11.025.

Bermingham, K.R., Walker, R.J., 2017. The ruthenium isotopic composition of the oceanic mantle. Earth Planet. Sci. Lett. 474, 466–476. doi: 10.1016/j.epsl.2017.06.052.

Bermingham, K.R., Worsham, E.A., Walker, R.J., 2018. New insights into Mo and Ru isotope variation in the nebula and terrestrial planet accretionary genetics. Earth Planet. Sci. Lett. 487, 221–229. doi: 10.1016/j.epsl.2018.01.017.

Binzel, R.P., DeMeo, F.E., Turtelboom, E.V., Bus, S.J., Tokunaga, A., Burbine, T.H., Lantz, C., Polishook, D., Carry, B., Morbidelli, A., Birlan, M., Vernazza, P., Burt, B.J., Moskovitz, N., Slivan, S.M., Thomas, C.A., Rivkin, A.S., Hicks, M.D., Dunn, T., Reddy, V., Sanchez, J.A., Granvik, M., Kohout, T., 2019. Compositional distributions and evolutionary processes for the near-Earth object population: Results from the MIT-Hawaii Near-Earth Object Spectroscopic Survey (MITHNEOS). Icarus 324, 41–76. doi: 10.1016/j.icarus.2018.12.035.

Binzel, R.P., Rivkin, A.S., Stuart, J.S., Harris, A.W., Bus, S.J., Burbine, T.H., 2004. Observed spectral properties of near-Earth objects: Results for population distribution, source regions, and space weathering processes. Icarus 170, 259–294. doi: 10.1016/j.icarus.2004.04.004.

Binzel, R.P., Xu, S., 1993. Chips off of asteroid 4 Vesta: Evidence for the parent body of basaltic achondrite meteorites. Science 260, 186–191. doi: 10.1126/science.260.5105.186.

Birck, J.L., 2004. An overview of isotopic anomalies in extraterrestrial materials and their nucleosynthetic heritage. Rev. Mineral. Geochem. 55, 25. doi: 10.2138/gsrmg.55.1.25.

Birnstiel, T., Klahr, H., Ercolano, B., 2012. A simple model for the evolution of the dust population in protoplanetary disks. Astron. Astrophys. 539, A148. doi: 10.1051/0004-6361/201118136.

Bischoff, A., Vogel, N., Roszjar, J., 2011. The Rumuruti chondrite group. Chemie der Erde 71, 101–133. doi: 10.1016/j.chemer.2011.02.005.

Bitsch, B., Johansen, A., Lambrechts, M., Morbidelli, A., 2015. The structure of protoplanetary discs around evolving young stars. Astron. Astrophys. 575, A28. doi: 10.1051/0004-6361/201424964.

Blinova, A.I., Herd, C.D.K., Duke, M.J.M., 2014. Testing variations within the Tagish Lake meteorite—II: Whole-rock geochemistry of pristine samples. Meteorit. Planet. Sci. 49, 1100–1118. doi: 10.1111/maps.12303.

Bottke, W.F., Nesvorný, D., Grimm, R.E., Morbidelli, A., O'Brien, D.P., 2006. Iron meteorites as remnants of planetesimals formed in the terrestrial planet region. Nature 439, 821–824. doi: 10.1038/nature04536.

Bouvier, A., Wadhwa, M., 2010. The age of the Solar System redefined by the oldest Pb–Pb age of a meteoritic inclusion. Nat. Geosci. 3, 637–641. doi: 10.1038/ngeo941.

Brasser, R., Dauphas, N., Mojzsis, S.J., 2018. Jupiter's influence on the building blocks of Mars and Earth. Geophys. Res. Lett. 45, 5908–5917. doi: 10.1029/2018GL078011.

Brasser, R., Matsumura, S., Ida, S., Mojzsis, S.J., Werner, S.C., 2016. Analysis of terrestrial planet formation by the Grand Tack model: System architecture and tack location. Astrophys. J. 821, 75. doi: 10.3847/0004-637X/821/2/75.

Brasser, R., Mojzsis, S.J., 2020. The partitioning of the inner and outer Solar System by a structured protoplanetary disk. Nat. Astron. 4, 492–499. doi: 10.1038/s41550-019-0978-6.

Brasser, R., Mojzsis, S.J., Matsumura, S., Ida, S., 2017. The cool and distant formation of Mars. Earth Planet. Sci. Lett. 468, 85–93. doi: 10.1016/j.epsl.2017.04.005.

Brennecka, G.A., Borg, L.E., Wadhwa, M., 2013. Evidence for supernova injection into the solar nebula and the decoupling of *r*-process nucleosynthesis. Proc. Natl. Acad. Sci. 110, 17241–17246. doi: 10.1073/pnas.1307759110.

Brown, P.G., Hildebrand, A.R., Zolensky, M.E., Grady, M., Clayton, R.N., Mayeda, T.K., Tagliaferri, E., Spalding, R., MacRae, N.D., Hoffman, E.L., Mittlefehldt, D.W., Wacker, J.F., Bird, J.A., Campbell, M.D., Carpenter, R., Gingerich, H., Glatiotis, M., Greiner, E., Mazur, M.J., McCausland, P.J., Plotkin, H., Mazur, T.R., 2000. The fall, recovery, orbit and composition of the Tagish Lake meteorite: A new type of carbonaceous chondrite. Science 290, 320–325. doi: 10.1126/science.290.5490.320.

Budde, G., Burkhardt, C., Brennecka, G.A., Fischer-Gödde, M., Kruijer, T.S., Kleine, T., 2016. Molybdenum isotopic evidence for the origin of chondrules and a distinct genetic heritage of carbonaceous and non-carbonaceous meteorites. Earth Planet. Sci. Lett. 454, 293–303. doi: 10.1016/j.epsl.2016.09.020.

Budde, G., Burkhardt, C., Kleine, T., 2019. Molybdenum isotopic evidence for the late accretion of outer Solar System material to Earth. Nat. Astron. 3, 736–741. doi: 10.1038/s41550-019-0779-y.

Budde, G., Kruijer, T.S., Kleine, T., 2018. Hf-W chronology of CR chondrites: Implications for the timescales of chondrule formation and the distribution of 26Al in the solar nebula. Geochim. Cosmochim. Acta 222, 284–304. doi: 10.1016/j.gca.2017.10.014.

Burkhardt, C., Borg, L.E., Brennecka, G.A., Shollenberger, Q.R., Dauphas, N., Kleine, T., 2016. A nucleosynthetic origin for the Earth's anomalous ^{142}Nd composition. Nature 537, 394–398. doi: 10.1038/nature18956.

Burkhardt, C., Dauphas, N., Tang, H., Fischer-Gödde, M., Qin, L., Chen, J.H., Rout, S.S., Pack, A., Heck, P.R., Papanastassiou, D.A., 2017. In search of the Earth-forming reservoir: Mineralogical, chemical, and isotopic characterizations of the ungrouped achondrite NWA 5363/NWA 5400 and selected chondrites. Meteorit. Planet. Sci. 52, 807–826. doi: 10.1111/maps.12834.

Burkhardt, C., Hin, R.C., Kleine, T., Bourdon, B., 2014. Evidence for Mo isotope fractionation in the solar nebula and during planetary differentiation. Earth Planet. Sci. Lett. 391, 201–211. doi: 10.1016/j.epsl.2014.01.037.

Burkhardt, C., Kleine, T., Dauphas, N., Wieler, R., 2012. Origin of isotopic heterogeneity in the solar nebula by thermal processing and mixing of nebular dust. Earth Planet. Sci. Lett. 357, 298–307. doi: 10.1016/j.epsl.2012.09.048.

Burkhardt, C., Kleine, T., Oberli, F., Pack, A., Bourdon, B., Wieler, R., 2011. Molybdenum isotope anomalies in meteorites: Constraints on solar nebula evolution and origin of the Earth. Earth Planet. Sci. Lett. 312, 390–400. doi: 0.1016/j.epsl.2011.10.010.

Carlson, R.W., Brasser, R., Yin, Q.Z., Fischer-Gödde, M., Qin, L., 2018. Feedstocks of the terrestrial planets. Space Sci. Rev. 214, 121. doi: 10.1007/s11214-018-0554-x.

Chambers, J., 2006. A semi-analytic model for oligarchic growth. Icarus 180, 496–513. doi: 10.1016/j.icarus.2005.10.017.

Chambers, J.E., 2001. Making more terrestrial planets. Icarus 152, 205–224. doi: 10.1006/icar.2001.6639.

Chambers, J.E., 2010. Planetesimal formation by turbulent concentration. Icarus 208, 505–517. doi: 10.1016/j.icarus.2010.03.004.

Chambers, J.E., 2016. Pebble accretion and the diversity of planetary systems. Astrophys. J. 825, 63. doi: 10.3847/0004-637X/825/1/63.

Chen, J.H., Papanastassiou, D.A., Wasserburg, G.J., 2010. Ruthenium endemic isotope effects in chondrites and differentiated meteorites. Geochim. Cosmochim. Acta 74, 3851–3862. doi: 10.1016/j.gca.2010.04.013.

Chiang, E.I., Goldreich, P., 1997. Spectral energy distributions of T Tauri stars with passive circumstellar disks. Astrophys. J. 490, 368. doi: 10.1086/304869.

Clark, B.E., Bus, S.J., Rivkin, A.S., McConnochie, T., Sanders, J., Shah, S., Hiroi, T., Shepard, M., 2004. E-type asteroid spectroscopy and compositional modeling. J. Geophys. Res. 109, E02001. doi: 10.1029/2003JE002200.

Clayton, D.D., 1982. Cosmic chemical memory: A new astronomy. Q. J. R. Astron. Soc. 23, 174–212.

Clayton, R.N., Mayeda, T.K., 1983. Oxygen isotopes in eucrites, shergottites, nakhlites, and chassignites. Earth Planet. Sci. Lett. 62, 1–6. doi: 10.1016/0012-821X(83)90066-3.

Clayton, R.N., Mayeda, T.K., 1996. Oxygen isotope studies of achondrites. Geochim. Cosmochim. Acta 60, 1999–2017. doi: 10.1016/0016-7037(96)00074-9.

Clement, M.S., Kaib, N.A., Raymond, S.N., Chambers, J.E., Walsh, K.J., 2019. The early instability scenario: Terrestrial planet formation during the giant planet instability, and the effect of collisional fragmentation. Icarus 321, 778–790. doi: 10.1016/j.icarus.2018.12.033.

Clement, M.S., Kaib, N.A., Raymond, S.N., Walsh, K.J., 2018. Mars' growth stunted by an early giant planet instability. Icarus 311, 340–356. doi: 10.1016/j.icarus.2018.04.008.

Clement, M.S., Raymond, S.N., Kaib, N.A., Deienno, R., Chambers, J.E., Izidoro, A., 2021. Born eccentric: Constraints on Jupiter and Saturn's pre-instability orbits. Icarus 355, 114122. doi: 10.1016/j.icarus.2020.114122.

Coleman, G.A., Nelson, R.P., 2014. On the formation of planetary systems via oligarchic growth in thermally evolving viscous discs. Mon. Not. R. Astron. Soc. 445, 479–499. doi: 10.1093/mnras/stu1715.

Collinet, M., Grove, T.L., 2020. Incremental melting in the ureilite parent body: Initial composition, melting temperatures, and melt compositions. Meteorit. Planet. Sci. 55, 832–856. doi: 10.1111/maps.13471.

Connelly, J.N., Bizzarro, M., Krot, A.N., Nordlund, Å., Wielandt, D., Ivanova, M.A., 2012. The Absolute Chronology and Thermal Processing of Solids in the Solar Protoplanetary Disk. Science 338, 651–655. doi: 10.1126/science.1226919.

Consolmagno, G.J., Drake, M.J., 1977. Composition and evolution of the eucrite parent body: Evidence from rare earth elements. Geochim. Cosmochim. Acta 41, 1271–1282. doi: 10.1016/0016-7037(77)90072--2.

Cresswell, P., Nelson, R.P., 2008. Three-dimensional simulations of multiple protoplanets embedded in a protostellar disc. Astron. Astrophys. 482, 677. doi: 10.1051/0004-6361:20079178.

Ćuk, M., Gladman, B.J., Nesvorný, D., 2014. Hungaria asteroid family as the source of aubrite meteorites. Icarus 239, 154–159. doi: 10.1016/j.icarus.2014.05.048.

D'Angelo, G., Marzari, F., 2012. Outward migration of Jupiter and Saturn in evolved gaseous disks. Astrophys. J. 757, 50. doi: 10.1088/0004-637X/757/1/50.

Dauphas, N., 2017. The isotopic nature of the Earth's accreting material through time. Nature 541, 521–524. doi: 10.1038/nature20830.

Dauphas, N., Burkhardt, C., Warren, P., Teng, F.Z., 2014a. Geochemical arguments for an Earth-like Moon-forming impactor. Phil. Trans. R. Soc. A 372, 20130244. doi: 10.1098/rsta.2013.0244.

Dauphas, N., Chen, J.H., Zhang, J., Papanastassiou, D.A., Davis, A.M., Travaglio, C., 2014b. Calcium-48 isotopic anomalies in bulk chondrites and achondrites: Evidence for a uniform isotopic reservoir in the inner protoplanetary disk. Earth Planet. Sci. Lett. 407, 96–108. doi: 10.1016/j.epsl.2014.09.015.

Dauphas, N., Marty, B., Reisberg, L., 2002. Molybdenum evidence for inherited planetary scale isotope heterogeneity of the protosolar nebula. Astrophys. J. 565, 640. doi: 10.1086/324597.

Dauphas, N., Poitrasson, F., Burkhardt, C., Kobayashi, H., Kurosawa, K., 2015. Planetary and meteoritic Mg/Si and δ^{30} Si variations inherited from solar nebula chemistry. Earth Planet. Sci. Lett. 427, 236–248. doi: 10.1016/j.epsl.2015.07.008.

Dauphas, N., Pourmand, A., 2011. Hf-W-Th evidence for rapid growth of Mars and its status as a planetary embryo. Nature 473, 489–492. doi: 10.1038/nature10077.

Deienno, R., Gomes, R.S., Walsh, K.J., Morbidelli, A., Nesvorný, D., 2016. Is the Grand Tack model compatible with the orbital distribution of main belt asteroids? Icarus 272, 114–124. doi: 10.1016/j.icarus.2016.02.043.

DeMeo, F.E., Carry, B., 2014. Solar System evolution from compositional mapping of the asteroid belt. Nature 505, 629–634. doi: 10.1038/nature12908.

Desch, S.J., Kalyaan, A., Alexander, C.M.O.D., 2018. The effect of Jupiter's formation on the distribution of refractory elements and inclusions in meteorites. Astrophys. J., Suppl. Ser. 238, 11. doi: 10.3847/1538-4365/aad95f.

Drake, M.J., Righter, K., 2002. Determining the composition of the Earth. Nature 416, 39–44. doi: 10.1038/416039a.

Dreibus, G., Kruse, H., Spettel, B., Wänke, H., 1977. The bulk composition of the Moon and the eucrite parent body, in: Proc. Lunar Sci. Conf. 8, pp. 211–227.

Drążkowska, J., Alibert, Y., 2017. Planetesimal formation starts at the snow line. Astron. Astrophys. 608, A92. doi: 10.1051/0004-6361/201731491.

Drążkowska, J., Alibert, Y., Moore, B., 2016. Close-in planetesimal formation by pile-up of drifting pebbles. Astron. Astrophys. 594, A105. doi: 10.1051/0004-6361/201628983.

Duncan, M.J., Levison, H.F., Lee, M.H., 1998. A multiple time step symplectic algorithm for integrating close encounters. Astron. J. 116, 2067–2077. doi: 10.1086/300541.

Dwarkadas, V.V., Dauphas, N., Meyer, B., Boyajian, P., Bojazi, M., 2017. Triggered star formation inside the shell of a Wolf-Rayet bubble as the origin of the Solar System. Astrophys. J. 851, 147. doi: 10.3847/1538-4357/aa992e.

Ek, M., Hunt, A.C., Lugaro, M., Schönbächler, M., 2020. The origin of s-process isotope heterogeneity in the solar protoplanetary disk. Nat. Astron. 4, 273–281. doi: 10.1038/s41550-019-0948-z.

Fendyke, S.M., Nelson, R.P., 2014. On the corotation torque for low-mass eccentric planets. Mon. Not. R. Astron. Soc. 437, 96–107. doi: 10.1093/mnras/stt1867.

Fischer-Gödde, M., Burkhardt, C., Kruijer, T.S., Kleine, T., 2015. Ru isotope heterogeneity in the solar protoplanetary disk. Geochim. Cosmochim. Acta 168, 151–171. doi: 10.1016/j.gca.2015.07.032.

Fischer-Gödde, M., Elfers, B.M., Münker, C., Szilas, K., Maier, W.D., Messling, N., Morishita, T., Van Kranendonk, M., Smithies, H., 2020. Ruthenium isotope vestige of Earth's pre-late-veneer mantle preserved in Archaean rocks. Nature 579, 240–244. doi: 10.1038/s41586-020-2069-3.

Fischer-Gödde, M., Kleine, T., 2017. Ruthenium isotopic evidence for an inner Solar System origin of the late veneer. Nature 541, 525–527. doi: 10.1038/nature21045.

Fisher, R.A., Ciesla, F.J., 2014. Dynamics of the terrestrial planets from a large number of N-body simulations. Earth Planet. Sci. Lett. 392, 28–38. doi: 10.1016/j.epsl.2014.02.011.

Fitoussi, C., Bourdon, B., Kleine, T., Oberli, F., Reynolds, B.C., 2009. Si isotope systematics of meteorites and terrestrial peridotites: Implications for Mg/Si fractionation in the solar nebula and for Si in the Earth's core. Earth Planet. Sci. Lett. 287, 77–85. doi: 10.1016/j.epsl.2009.07.038.

Fitoussi, C., Bourdon, B., Wang, X., 2016. The building blocks of Earth and Mars: A close genetic link. Earth Planet. Sci. Lett. 434, 151–160. doi: 10.1016/j.epsl.2015.11.036.

Franchi, I.A., Wright, I.P., Sexton, A.S., Pillinger, C.T., 1999. The oxygen-isotopic composition of Earth and Mars. Meteorit. Planet. Sci. 34, 657–661. doi: 10.1111/j.1945-5100.1999.tb01371.x.

Fujimoto, Y., Krumholz, M.R., Tachibana, S., 2018. Short-lived radioisotopes in meteorites from Galactic-scale correlated star formation. Mon. Not. R. Astron. Soc. 480, 4025–4039. doi: 10.1093/mnras/sty2132.

Fukao, Y., Obayashi, M., 2013. Subducted slabs stagnant above, penetrating through, and trapped below the 660 km discontinuity. J. Geophys. Res. Solid Earth 118, 5920–5938. doi: 10.1002/2013JB010466.

Gaffey, M.J., Bell, J.F., Brown, R.H., Burbine, T.H., Piatek, J.L., Reed, K.L., Chaky, D.A., 1993. Mineralogic variations within the S-type asteroid class. Icarus 106, 573–602. doi: 10.1006/icar.1993.1194.

Gaffey, M.J., Gilbert, S.L., 1998. Asteroid 6 Hebe: The probable parent body of the H-type ordinary chondrites and the IIE iron meteorites. Meteorit. Planet. Sci. 33, 1281–1295. doi: 10.1111/j.1945-5100.1998.tb01312.x.

Garaud, P., 2007. Growth and migration of solids in evolving protostellar disks. I. Methods and analytical tests. Astrophys. J. 671, 2091. doi: 10.1086/523090.

Garaud, P., Lin, D.N.C., 2007. The effect of internal dissipation and surface irradiation on the structure of disks and the location of the snow line around Sun-like stars. Astron. Astrophys. 654, 606. doi: 10.1086/509041.

Goodrich, C.A., 1999. Are ureilites residues from partial melting of chondritic material? The answer from MAGPOX. Meteorit. Planet. Sci. 34, 109–119. doi: 10.1111/j.1945-5100.1999.tb01736.x.

Greenwood, R.C., Anand, M., 2020. What is the oxygen isotope composition of Venus? The scientific case for sample return from Earth's "sister" planet. Space Sci. Rev. 216, 52. doi: 10.1007/s11214-020-00669-8.

Greenwood, R.C., Burbine, T.H., Franchi, I.A., 2020. Linking asteroids and meteorites to the primordial planetesimal population. Geochim. Cosmochim. Acta 277, 377–406. doi: 10.1016/j.gca.2020.02.004.

Greenwood, R.C., Franchi, I.A., Kearsley, A.T., Alard, O., 2010. The relationship between CK and CV chondrites. Geochim. Cosmochim. Acta 74, 1684–1705. doi: 10.1016/j.gca.2009.11.029.

Grimm, S.L., Stadel, J.G., 2014. The GENGA code: Gravitational encounters in N-body simulations with GPU acceleration. Astrophys. J. 796, 23. doi: 10.1088/0004-637X/796/1/23.

Hansen, B.M.S., 2009. Formation of the terrestrial planets from a narrow annulus. Astrophys. J. 703, 1131. doi: 10.1088/0004-637X/703/1/1131.

Hartmann, D., Woosley, S.E., El Eid, M.F., 1985. Nucleosynthesis in neutron-rich supernova ejecta. Astrophys. J. 297, 837. doi: 10.1086/163580.

Hartmann, L., Calvet, N., E., G., D'Alessio, P., 1998. Accretion and the evolution of T Tauri disks. Astrophys. J. 495, 385. doi: 10.1086/305277.

Hasegawa, Y., Ida, S., 2013. Do giant planets survive type II migration? Astrophys. J. 774, 146. doi: 10.1088/0004-637X/774/2/146.

Hayashi, C., 1981. Structure of the solar nebula, growth and decay of magnetic fields and effects of magnetic and turbulent viscosities on the nebula. Prog. Theor. Phys. Suppl. 70, 35–53. doi: 10.1143/PTPS.70.35.

Hertogen, J., Vizgirda, J., Anders, E., 1977. Composition of the parent body of the eucrite meteorites. Bull. Amer. Astron. Soc. 9, 458–459.

Hewins, R.H., Bourot-Denise, M., Zanda, B., Leroux, H., Barrat, J.A., Humayun, M., Göpel, C., Greenwood, R.C., Franchi, I.A., Pont, S., Lorand, J.P., Cournéde, C., Gattacceca, J., Rochette, P., Kuga, M., Marrocchi, Y., B., M., 2014. The Paris meteorite, the least altered CM chondrite so far. Geochim. Cosmochim. Acta 124, 190–222. doi: 10.1016/j.gca.2013.09.014.

Hilton, C.D., Bermingham, K.R., Walker, R.J., McCoy, T.J., 2019. Genetics crystallization sequence, and age of the South Byron Trio iron meteorites: New insights to carbonaceous chondrite (CC) type parent bodies. Geochim. Cosmochim. Acta 251, 217–228. doi: 10.1016/j.gca.2019.02.035.

Hopp, T., Budde, G., Kleine, T., 2020. Heterogeneous accretion of Earth inferred from Mo-Ru isotope systematics. Earth Planet. Sci. Lett. 534, 116065. doi: 10.1016/j.epsl.2020.116065.

Ida, S., Guillot, T., Morbidelli, A., 2016. The radial dependence of pebble accretion rates: A source of diversity in planetary systems. I. Analytical formulation. Astron. Astrophys. 591, A72. doi: 10.1051/0004-6361/201628099.

Ikoma, M., Nakazawa, K., Emori, H., 2000. Formation of giant planets: Dependences on core accretion rate and grain opacity. Astrophys. J. 537, 1013. doi: 10.1086/309050.

Izidoro, A., Haghighipour, N., Winter, O.C., Tsuchida, M., 2014. Terrestrial planet formation in a protoplanetary disk with a local mass depletion: A successful scenario for the formation of Mars. Astrophys. J. 782, 31. doi: 10.1088/0004-637X/782/1/31.

Izidoro, A., Raymond, S.N., Morbidelli, A., Winter, O.C., 2015. Terrestrial planet formation constrained by Mars and the structure of the asteroid belt. Mon. Not. R. Astron. Soc. 453, 3619–3634. doi: 10.1093/mnras/stv1835.

Jacobson, S.A., Morbidelli, A., 2014. Lunar and terrestrial planet formation in the Grand Tack scenario. Philos. Trans. R. Soc. London, Ser. A 372, 20130174. doi: 10.1098/rsta.2013.0174.

Jacobson, S.A., Morbidelli, A., Raymond, S.N., O'Brien, D.P., Walsh, K.J., Rubie, D.C., 2014. Highly siderophile elements in Earth's mantle as a clock for the Moon-forming impact. Nature 508, 84–87. doi: 10.1038/nature13172.

Jacobson, S.A., Walsh, K.J., 2015. Earth and terrestrial planet formation, in: Badro, J., Walter, M. (Eds.), The Early Earth, American Geophysical Union (AGU). pp. 49–70. doi: 10.1002/9781118860359.ch3.

Jagoutz, E., Palme, H., Baddenhausen, H., Blum, K., Cendales, M., Dreibus, G., 1979. The abundances of major, minor and trace elements in the earth's mantle as derived from primitive ultramafic nodules, in: Proc. Lunar Planet. Sci. Conf. 10, pp. 2031–2050.

Jarosewich, E., 1990. Chemical analyses of meteorites: A compilation of stony and iron meteorite analyses. Meteoritics 25, 323–337. doi: 10.1111/j.1945-5100.1990.tb00717.x.

Jarosewich, E., Clark, R.S., Barrows, J.N., 1987. The Allende meteorite reference sample. Smithsonian Contrib. Earth Sci. 27, 1–53. doi: 10.5479/si.00810274.27.1.

Javoy, M., Kaminski, E., Guyot, F., Andrault, D., Sanloup, C., Moreira, M., Labrosse, S., Jambon, A., Agrinier, P., Davaille, A., Jaupart, C., 2010. The chemical composition of the Earth: Enstatite chondrite models. Earth Planet. Sci. Lett. 293, 259–268. doi: 10.1016/j.epsl.2010.02.033.

Jin, L., Arnett, W.D., Sui, N., Wang, X., 2008. An interpretation of the anomalously low mass of Mars. Astrophys. J. 674, L105. doi: 10.1086/529375.

Johansen, A., Blum, J., Tanaka, H., Ormel, C., Bizzarro, M., Rickman, H., 2014. The multifaceted planetesimal formation process, in: Beuther, H., Klessen, R.S., Dullemond, C.P., Henning, T. (Eds.), Protostars and Planets VI, University of Arizona Press. p. 547. doi: 10.2458/azu_uapress_9780816531240-ch024.

Johansen, A., Ida, S., Brasser, R., 2019. How planetary growth outperforms migration. Astron. Astrophys. 622, A202. doi: 10.1051/0004-6361/201834071.

Johansen, A., Mac Low, M.M., Lacerda, P., Bizzarro, M., 2015. Growth of asteroids, planetary embryos, and Kuiper belt objects by chondrule accretion. Sci. Adv. 1, e1500109. doi: 10.1126/sciadv.1500109.

Johansen, A., Ronnet, T., Bizzarro, M., Schiller, M., Lambrechts, M., Nordlund, Å., Lammer, H., 2021. A pebble accretion model for the formation of the terrestrial planets in the solar system. Sci. Adv. 7, eabc0444. doi: 10.1126/sciadv.abc0444.

Kaib, N.A., Cowan, N.B., 2015. The feeding zones of terrestrial planets and insights into Moon formation. Icarus 252, 161–174. doi: 10.1016/j.icarus.2015.01.013.

Kallemeyn, G.W., Rubin, A.E., Wasson, J.T., 1991. The compositional classification of chondrites: V. The Karoonda (CK) group of carbonaceous chondrites. Geochim. Cosmochim. Acta 55, 881–892. doi: 10.1016/0016-7037(91)90348-9.

Kallemeyn, G.W., Rubin, A.E., Wasson, J.T., 1994. The compositional classification of chondrites: VI. The CR carbonaceous chondrite group. Geochim. Cosmochim. Acta 58, 2873–2888. doi: 10.1016/0016-7037(94)90121-X.

Kallemeyn, G.W., Rubin, A.E., Wasson, J.T., 1996. The compositional classification of chondrites: VII. The R chondrites. Geochim. Cosmochim. Acta 60, 2243–2256. doi: 10.1016/0016-7037(96)88430-4.

Keil, K., 2002. Geological history of asteroid 4 Vesta: The "smallest terrestrial planet", in: Bottke, J.W.F., Cellino, A., Paolicchi, P., Binzel, R.P. (Eds.), Asteroids III, University of Arizona Press. pp. 573–584.

Klahr, H., Schreiber, A., 2020. Turbulence sets the length scale for planetesimal formation: Local 2D simulations of streaming instability and planetesimal formation. Astrophys. J. 901, 54. doi: 10.3847/1538-4357/abac58.

Kleine, T., Budde, G., Burkhardt, C., Kruijer, T.S., Worsham, E.A., Morbidelli, A., Nimmo, F., 2020. The non-carbonaceous-carbonaceous meteorite dichotomy. Space Sci. Rev. 216, 55. doi: 10.1007/s11214-020-00675-w.

Kleine, T., Touboul, M., Bourdon, B., Nimmo, F., Mezger, K., Palme, H., Jacobsen, S.B., Yin, Q.Z., Halliday, A.N., 2009. Hf–W chronology of the accretion and early evolution of asteroids and terrestrial planets. Geochim. Cosmochim. Acta 73, 5150–5188. doi: 10.1016/j.gca.2008.11.047.

Kokubo, E., Ida, S., 1995. Orbital evolution of protoplanets embedded in a swarm of planetesimals. Icarus 114, 247–257. doi: 10.1006/icar.1995.1059.

Kokubo, E., Ida, S., 1996. On runaway growth of planetesimals. Icarus 123, 180–191. doi: 10.1006/icar.1996.0148.

Kokubo, E., Ida, S., 1998. Oligarchic growth of protoplanets. Icarus 131, 171–178. doi: 10.1006/icar.1997.5840.

Kong, P., Mori, T., Ebihara, M., 1997. Compositional continuity of enstatite chondrites and implications for heterogeneous accretion of the enstatite chondrite parent body. Geochim. Cosmochim. Acta 61, 4895–4914. doi: 10.1016/S0016-7037(97)00278-0.

Kruijer, T.S., Burkhardt, C., Budde, G., Kleine, T., 2017. Age of Jupiter inferred from the distinct genetics and formation times of meteorites. Proc. Natl. Acad. Sci. 114, 6712–6716. doi: 10.1073/pnas.1704461114.

Kruijer, T.S., Touboul, M., Fischer-Gödde, M., Bermingham, K.R., Walker, R.J., Kleine, T., 2014. Protracted core formation and rapid accretion of protoplanets. Science 344, 1150–1154. doi: 10.1126/science.1251766.

Kurnosov, A., Marquardt, H., Frost, D.J., Ballaran, T.B., Ziberna, L., 2018. Evidence for a Fe^{3+}-rich pyrolitic lower mantle from (Al,Fe)-bearing bridgmanite elasticity data. Nature 543, 543–546. doi: 10.1038/nature21390.

Lambrechts, M., Johansen, A., 2012. Rapid growth of gas-giant cores by pebble accretion. Astron. Astrophys. 544, A32. doi: 10.1051/0004-6361/201219127.

Lambrechts, M., Johansen, A., 2014. Forming the cores of giant planets from the radial pebble flux in protoplanetary discs. Astron. Astrophys. 572, A107. doi: 10.1051/0004-6361/201424343.

Lambrechts, M., Johansen, A., Morbidelli, A., 2014. Separating gas-giant and ice-giant planets by halting pebble accretion. Astron. Astrophys. 572, A35. doi: 10.1051/0004-6361/201423814.

Larimer, J.W., 1979. The condensation and fractionation of refractory lithophile elements. Icarus 40, 446–454. doi: 10.1016/0019-1035(79)90038-1.

Larsen, K.K., Trinquier, A., Paton, C., Schiller, M., Wielandt, D., Ivanova, M.A., Connelly, J.N., Nordlund, Å., Krot, A.N., Bizzarro, M., 2011. Evidence for magnesium isotope heterogeneity in the solar protoplanetary disk. Astrophys. J. Lett. 735, L37. doi: 10.1088/2041-8205/735/2/L37.

Laskar, J., 2008. Chaotic diffusion in the Solar System. Icarus 196, 1–15. doi: 10.1016/j.icarus.2008.02.017.

Levison, H.F., Kretke, K.A., Duncan, M.J., 2015a. Growing the gas-giant planets by the gradual accumulation of pebbles. Nature 524, 322–324. doi: 10.1038/nature14675.

Levison, H.F., Kretke, K.A., Walsh, K.J., Bottke, W.F., 2015b. Growing the terrestrial planets from the gradual accumulation of submeter-sized objects. Proc. Natl. Acad. Sci. 112, 14180–14185. doi: 10.1073/pnas.1513364112.

Lichtenberg, T., Drążkowska, J., Schönbächler, M., Golabek, G.J., Hands, T.O., 2021. Bifurcation of planetary building blocks during Solar System formation. Science 371, 365–370. doi: 10.1126/science.abb3091.

Lin, D.N.C., Papaloizou, J.C.B., 1986. On the tidal interaction between protoplanets and the protoplanetary disk. III. Orbital migration of protoplanets. Astrophys. J. 309, 846. doi: 10.1086/164653.

Lodders, K., 2000. An oxygen isotope mixing model for the accretion and composition of rocky planets. Space Sci. Rev. 92, 341–354. doi: 10.1023/A:1005220003004.

Lodders, K., 2003. Solar System abundances and condensation temperatures of the elements. Astrophys. J. 591, 1220. doi: 10.1086/375492.

Lodders, K., Fegley, B., 1997. An oxygen isotope model for the composition of Mars. Icarus 126, 373–394. doi: 10.1006/icar.1996.5653.

Longhi, J., 1999. Phase equilibrium constraints on angrite petrogenesis. Geochim. Cosmochim. Acta 63, 573–585. doi: 10.1016/S0016-7037(98)00280-4.

Luu, T.H., Young, E.D., Gounelle, M., Chaussidon, M., 2015. Short time interval for condensation of high-temperature silicates in the solar accretion disk. Proc. Natl. Acad. Sci. 112, 1298–1303. doi: 10.1073/pnas.1414025112.

Mah, J., Brasser, R., 2021. Isotopically distinct terrestrial planets via local accretion. Icarus 354, 114052. doi: 10.1016/j.icarus.2020.114052.

Mashino, I., Murakami, M., Miyajima, N., Petitgirard, S., 2020. Experimental evidence for silica-enriched Earth's lower mantle with ferrous iron dominant bridgmanite. Proc. Natl. Acad. Sci. 117, 27899–27905. doi: 10.1073/pnas.1917096117.

Mason, B., Wiik, H.B., 1962. The composition of Solar system asteroids and Earth/Mars moons, and the Earth–Moon composition similarity. Amer. Mus. Novitates 2106, 1–11.

Matsumura, S., Brasser, R., Ida, S., 2016. Effects of dynamical evolution of giant planets on the delivery of atmophile elements during terrestrial planet formation. Astrophys. J. 818, 15. doi: 10.3847/0004-637X/818/1/15.

Matsumura, S., Brasser, R., Ida, S., 2017. *N*-body simulations of planet formation via pebble accretion. I. First results. Astron. Astrophys. 607, A67. doi: 10.1051/0004-6361/201731155.

McCord, T.B., Adams, J.B., Johnson, T.V., 1970. Asteroid Vesta: Spectral reflectivity and compositional implications. Science 168, 1445–1447. doi: 10.1126/science.168.3938.1445.

McDonough, W.F., 2016. The composition of the lower mantle and core, in: Terasaki, H., Fischer, R.A. (Eds.), Deep Earth: Physics and Chemistry of the Lower Mantle and Core, Geophysical Monograph 217, First Edition, John Wiley & Sons, Inc.. pp. 145–159.

McDonough, W.F., Sun, S.s., 1995. The composition of the Earth. Chem. Geol. 120, 223–253. doi: 10.1016/0009-2541(94)00140-4.

McSween, H.Y., Jr., Binzel, R.P., De Sanctis, M.C., Ammannito, E., Prettyman, T.H., Beck, A.W., Reddy, V., Le Corre, L., Gaffey, M.J., McCord, T.B., Raymond, C.A., Russell, C.T., the Dawn Science Team, 2013. Dawn; the Vesta-HED connection; and the geologic context for eucrites, diogenites, and howardites. Meteorit. Planet. Sci. 48, 2090–2104. doi: 10.1111/maps.12108.

Metropolis, N., Rosenbluth, A.W., Rosenbluth, M.N., Teller, A.H., 1953. Equation of state calculations by fast computing machines. J. Chem. Phys. 21, 1087. doi: 10.1063/1.1699114.

Mezger, K., Schönbächler, M., Bouvier, A., 2020. Accretion of the Earth–Missing components? Space Sci. Rev. 216, 27. doi: 10.1007/s11214-020-00649-y.

Mittlefehldt, D.W., Clayton, R.N., Drake, M.J., Righter, K., 2008. Oxygen isotopic composition and chemical correlations in meteorites and the terrestrial planets. Rev. Mineral. Geochem. 68, 399–428. doi: 10.2138/rmg.2008.68.14.

Mittlefehldt, D.W., McCoy, T.J., Goodrich, C.A., Kracher, A., 1998. Non-chondritic meteorites from asteroidal bodies. Rev. Mineral. Geochem. 36, 4–1–4–195.

Morbidelli, A., Bitsch, B., Crida, A., Gounelle, M., Guillot, T., Jacobson, S., Johansen, A., Lambrechts, M., Lega, E., 2016. Fossilized condensation lines in the Solar System protoplanetary disk. Icarus 267, 368–376. doi: 10.1016/j.icarus.2015.11.027.

Morbidelli, A., Bottke, W.F., Nesvorný, D., Levision, H.F., 2009. Asteroids were born big. Icarus 204, 558–573. doi: 10.1016/j.icarus.2009.07.011.

Morbidelli, A., Tsiganis, K., Crida, A., Levison, H.F., Gomes, R., 2007. Dynamics of the giant planets of the Solar System in the gaseous protoplanetary disk and their relationship to the current orbital architecture. Astron. J. 134, 1790. doi: 10.1086/521705.

Morgan, J.W., Higuchi, H., Takahashi, H., Hertogen, J.A., 1978. A "chondritic" eucrite parent body: Inference from trace elements. Geochim. Cosmochim. Acta 42, 27–38. doi: 10.1016/0016-7037(78)90213-2.

Moynier, F., Deng, Z., Lanteri, A., Martins, R., Chaussidon, M., Savage, P., Siebert, J., 2020. Metal-silicate silicon isotopic fractionation and the composition of the bulk Earth. Earth Planet. Sci. Lett. 549, 116468. doi: 10.1016/j.epsl.2020.116468.

Murakami, M., Ohishi, Y., Hirao, N., Hirose, K., 2012. A perovskitic lower mantle inferred from high-pressure, high-temperature sound velocity data. Nature 485, 90–94. doi: 10.1038/nature11004.

Nanne, J.A.M., Nimmo, F., Cuzzi, J.N., Kleine, T., 2019. Origin of the non-carbonaceous-carbonaceous meteorite dichotomy. Earth Planet. Sci. Lett. 511, 44–54. doi: 10.1016/j.epsl.2019.01.027.

O'Brien, D.P., Morbidelli, A., Levison, H.F., 2006. Terrestrial planet formation with strong dynamical friction. Icarus 184, 39–58. doi: 10.1016/j.icarus.2006.04.005.

O'Brien, D.P., Walsh, K.J., Morbidelli, A., Raymond, S.N., Mandell, A.M., 2014. Water delivery and giant impacts in the 'Grand Tack' scenario. Icarus 239, 74–84. doi: 10.1016/j.icarus.2014.05.009.

Ormel, C.W., Klahr, H.H., 2010. The effect of gas drag on the growth of protoplanets. Analytical expressions for the accretion of small bodies in laminar disks. Astron. Astrophys. 520, A43. doi: 10.1051/0004-6361/201014903.

Ormel, C.W., Kobayashi, H., 2012. Understanding how planets become massive. I. Description and validation of a new toy model. Astrophys. J. 747, 115. doi: 10.1088/0004-637X/747/2/115.

Ouellette, N., Desch, S.J., Bizzarro, M., Boss, A.P., Ciesla, F., Meyer, B., 2009. Injection mechanisms of short-lived radionuclides and their homogenization. Geochim. Cosmochim. Acta 73, 4946–4962. doi: 10.1016/j.gca.2008.10.044.

Paardekooper, S.J., Baruteau, C., Kley, W., 2011. A torque formula for non-isothermal Type I planetary migration—II. Effects of diffusion. Mon. Not. R. Astron. Soc. 410, 293–303. doi: 10.1111/j.1365-2966.2010.17442.x.

Paardekooper, S.J., Mellema, G., 2006. Dust flow in gas disks in the presence of embedded planets. Astron. Astrophys. 453, 1129. doi: 10.1051/0004-6361:20054449.

Pahlevan, K., Stevenson, D.J., 2007. Equilibration in the aftermath of the lunar-forming giant impact. Earth Planet. Sci. Lett. 262, 438–449. doi: 10.1016/j.epsl.2007.07.055.

Palme, H., Lodders, K., Jones, A., 2014. Solar System Abundances of the Elements, in: Davis, A.M. (Ed.), Treatise on Geochemistry (Second Edition), Elsevier. pp. 15–36. doi: 10.1016/B978-0-08-095975-7.00118-2.

Palme, H., O'Neill, H.S.C., 2014. Cosmochemical estimates of mantle composition, in: Carlson, R.W. (Ed.), Treatise on Geochemistry (Second Edition), Elsevier. pp. 1–39. doi: 10.1016/B978-0-08-095975-7.00201-1.

Petitat, M., Birck, J.L., Luu, T.H., Gounelle, M., 2011. The chromium isotopic composition of the ungrouped carbonaceous chondrite Tagish Lake. Astrophys. J. 736, 23. doi: 10.1088/0004-637X/736/1/23.

Piani, L., Marrocchi, Y., Rigaudier, T., Vacher, L.G., Thomassin, D., Marty, B., 2020. Earth's water may have been inherited from material similar to enstatite chondrite meteorites. Science 369, 1110–1113. doi: 10.1126/science.aba1948.

Pierens, A., Raymond, S.N., Nesvorný, D., Morbidelli, A., 2014. Outward migration of Jupiter and Saturn in 3:2 or 2:1 resonance in radiative disks: Implicationf for the Grand Tack and Nice models. Astrophys. J. Lett. 795, L11. doi: 10.1088/2041-8205/795/1/L11.

Poole, G.M., Rehkämper, M., Coles, B.J., Goldberg, T., Smith, C.L., 2017. Nucleosynthetic molybdenum isotope anomalies in iron meteorites – new evidence for thermal processing of solar nebula material. Earth Planet. Sci. Lett. 473, 215–226. doi: 10.1016/j.epsl.2017.05.001.

Portegies Zwart, S., Pelupessy, I., van Elteren, A., Wijnen, T.P.G., Lugaro, M., 2018. The consequences of a nearby supernova on the early solar system. Astron. Astrophys. 616, A85. doi: 10.1051/0004-6361/201732060.

Qin, L., Alexander, C.M.O.D., Carlson, R.W., Horan, M.F., Yokoyama, T., 2010a. Contributors to chromium isotope variation of meteorites. Geochim. Cosmochim. Acta 74, 1122–1145. doi: 10.1016/j.gca.2009.11.005.

Qin, L., Carlson, R.W., 2016. Nucleosynthetic isotope anomalies and their cosmochemical significance. Geochem. J. 50, 43–65. doi: 10.2343/geochemj.2.0401.

Qin, L., Rumble, D., Alexander, C.M.O.D., Carlson, R.W., Jenniskens, P., Shaddad, M.H., 2010b. The chromium isotopic composition of Almahata Sitta. Meteorit. Planet. Sci. 45, 1771–1777. doi: 10.1111/j.1945-5100.2010.01109.x.

Raymond, S.N., Izidoro, A., 2017a. Origin of water in the inner Solar System: Planetesimals scattered inward during Jupiter and Saturn's rapid gas accretion. Icarus 297, 134–148. doi: 10.1016/j.icarus.2017.06.030.

Raymond, S.N., Izidoro, A., 2017b. The empty primordial asteroid belt. Sci. Adv. 3, e1701138. doi: 10.1126/sciadv.1701138.

Raymond, S.N., O'Brien, D.P., Morbidelli, A., Kaib, N.A., 2009. Building the terrestrial planets: Constrained accretion in the inner Solar System. Icarus 203, 644–662. doi: 10.1016/j.icarus.2009.05.016.

Raymond, S.N., Quinn, T., Lunine, J.I., 2004. Making other earths: Dynamical simulations of terrestrial planet formation and water delivery. Icarus 168, 1–17. doi: 10.1016/j.icarus.2003.11.019.

Render, J., Fischer-Gödde, M., Burkhardt, C., Kleine, T., 2017. The cosmic molybdenum-neodymium isotope correlation and the building material of the Earth. Geochem. Perspect. Lett. 3, 170–178. doi: 10.7185/geochemlet.1720.

Rodmann, J., Henning, T., Chandler, C.J., Mundy, L.G., Wilner, D.J., 2006. Large dust particles in disks around T Tauri stars. Astron. Astrophys. 446, 211. doi: 10.1051/0004-6361:20054038.

Rubin, A.E., Warren, P.H., Greenwood, J.P., Verish, R.S., Leshin, L.A., Hervig, R.L., Clayton, R.N., Mayeda, T.K., 2000. Los Angeles: The most differentiated basaltic martian meteorite. Geology 28, 1011. doi: 10.1130/0091-7613(2000)28<1011:LATMDB>2.0.CO;2.

Safronov, V.S., 1969. Evolution of the protoplanetary cloud and formation of the Earth and the planets. Israel Program for Scientific Translations .

Sanloup, C., Jambon, A., Gillet, P., 1999. A simple chondritic model of Mars. Phys. Earth Planet. Inter. 112, 43–54. doi: 10.1016/S0031-9201(98)00175-7.

Sato, T., Okuzumi, S., Ida, S., 2016. On the water delivery to terrestrial embryos by ice pebble accretion. Astron. Astrophys. 589, A15. doi: 10.1051/0004-6361/201527069.

Schäfer, U., Yang, C.C., Johansen, A., 2017. Initial mass function of planetesimals formed by the streaming instability. Astron. Astrophys. 597, A69. doi: 10.1051/0004-6361/201629561.

Schiller, M., Bizzarro, M., Assis Fernandes, V., 2018. Isotopic evolution of the protoplanetary disk and the building blocks of Earth and the Moon. Nature 555, 507–510. doi: 10.1038/nature25990.

Schiller, M., Bizzarro, M., Siebert, J., 2020. Iron isotope evidence for very rapid accretion and differentiation of the proto-Earth. Sci. Adv. 6, eaay7604. doi: 10.1126/sciadv.aay7604.

Shakura, N.I., Sunyaev, R.A., 1973. Black holes in binary systems. Observational appearance. Astron. Astrophys. 24, 337.

Shukolyukov, A., Lugmair, G.W., 2006. Manganese-chromium isotope systematics of carbonaceous chondrites. Earth Planet. Sci. Lett. 250, 200–213. doi: 10.1016/j.epsl.2006.07.036.

Simon, J.B., Armitage, P.J., Li, R., Youdin, A.N., 2016. The mass and size distribution of planetesimals formed by the streaming instability. I. The role of self-gravity. Astrophys. J. 822, 55. doi: 10.3847/0004-637X/822/1/55.

Stracke, A., Palme, H., Gellissen, M., Münker, C., Kleine, T., Birbaum, K., Günther, D., Bourdon, B., Zipfel, J., 2012. Refractory element fractionation in the Allende meteorite: Implications for solar nebula condensation and the chondritic composition of planetary bodies. Geochim. Cosmochim. Acta 85, 114–141. doi: 10.1016/j.gca.2012.02.006.

Tanaka, H., Takeuchi, T., Ward, W.R., 2002. Three-dimensional interaction between a planet and an isothermal gaseous disk. I. Corotation and Lindblad torques and planet migration. Astrophys. J. 565, 1257. doi: 10.1086/324713.

Tanaka, H., Ward, W.R., 2004. Three-dimensional interaction between a planet and an isothermal gaseous disk. II. Eccentricity waves and bending waves. Astrophys. J. 602, 388. doi: 10.1086/380992.

Tang, H., Dauphas, N., 2014. ^{60}Fe-^{60}Ni chronology of core formation in Mars. Earth Planet. Sci. Lett. 390, 264–274. doi: 10.1016/j.epsl.2014.01.005.

Testi, L., Natta, A., Shepherd, D.S., Wilner, D.J., 2003. Large grains in the disk of CQ Tau. Astron. Astrophys. 403, 323. doi: 10.1051/0004-6361:20030362.

Thommes, E.W., Duncan, M.J., Levison, H.F., 1999. The formation of Uranus and Neptune in the Jupiter–Saturn region of the Solar System. Nature 402, 635–638. doi: 10.1038/45185.

Touboul, M., Kleine, T., Bourdon, B., Palme, H., Wieler, R., 2007. Late formation and prolonged differentiation of the Moon inferred from W isotopes in lunar metals. Nature 450, 1206–1209. doi: 10.1038/nature06428.

Trinquier, A., Birck, J.L., Allegre, C.J., 2007. Widespread ^{54}Cr heterogeneity in the inner Solar System. Astrophys. J. 655, 1179. doi: 10.1086/510360.

Trinquier, A., Birck, J.L., Allegre, C.J., Göpel, C., Ulfbeck, D., 2008. ^{53}Mn-^{53}Cr systematics of the early Solar System revisited. Geochim. Cosmochim. Acta 72, 5146–5163. doi: 10.1016/j.gca.2008.03.023.

Trinquier, A., Elliott, T., Ulfbeck, D., Coath, C., Krot, A.N., Bizzarro, M., 2009. Origin of nucleosynthetic isotope heterogeneity in the solar protoplanetary disk. Science 324, 374–376. doi: 10.1126/science.1168221.

Tsiganis, K., Gomes, R., Morbidelli, A., Levison, H.F., 2005. Origin of the orbital architecture of the giant planets of the Solar System. Nature 435, 459–461. doi: 10.1038/nature03539.

Von Michaelis, H., Ahrens, L.H., Willis, J.P., 1968. The composition of stony meteorites II. The analytical data and an assessment of their quality. Earth Planet. Sci. Lett. 5, 387–394. doi: 10.1016/S0012-821X(68)80070-6.

Walsh, K.J., Morbidelli, A., Raymond, S.N., O'Brien, D.P., Mandell, A.M., 2011. A low mass for Mars from Jupiter's early gas-driven migration. Nature 475, 206–209. doi: 10.1038/nature10201.

Wanajo, S., Janka, H.T., Müller, B., 2013. Electron-capture supernovae as origin of ^{48}Ca. Astrophys. J. Lett. 767, L26. doi: 10.1088/2041-8205/767/2/L26.

Wang, X., Tsuchiya, T., Hase, A., 2015. Computational support for a pyrolitic lower mantle containing ferric iron. Nat. Geosci. 8, 556–559. doi: 10.1038/ngeo2458.

Warren, P.H., 2011. Stable-isotopic anomalies and the accretionary assemblage of the Earth and Mars: A subordinate role for carbonaceous chondrites. Earth Planet. Sci. Lett. 311, 93–100. doi: 10.1016/j.epsl.2011.08.047.

Wasson, J.T., Kallemeyn, G.W., 1988. Compositions of chondrites. Phil. Trans. R. Soc. Lond. A 325, 535–544. doi: 10.1098/rsta.1988.0066.

Watters, T.R., Prinz, M., 1979. Aubrites: Their origin and relationship to enstatite chondrites, in: Proc. Lunar Planet. Sci. Conf. 10, pp. 1073–1093.

Weidenschilling, S.J., 1977. Aerodynamics of solid bodies in the solar nebula. Mon. Not. R. Astron. Soc. 180, 57–70. doi: 10.1093/mnras/180.2.57.

Wetherill, G.W., 1980. Formation of the terrestrial planets. Ann. Rev. Astron. Astrophys. 18, 77–113. doi: 10.1146/annurev.aa.18.090180.000453.

Wetherill, G.W., Stewart, G.R., 1989. Accumulation of a swarm of small planetesimals. Icarus 77, 330–357. doi: 10.1016/0019-1035(89)90093-6.

Wilner, D.J., D'Alessio, P., Calvet, N., Claussen, M.J., Hartmann, L., 2005. Toward planetesimals in the disk around TW Hydrae: 3.5 centimeter dust emission. Astrophys. J. 626, L109. doi: 10.1086/431757.

Wittmann, A., Korotev, R.L., Jolliff, B.L., Irving, A.J., Moser, D.E., Barker, I., Rumble, D., 2015. Petrography and composition of Martian regolith breccia meteorite Northwest Africa 7475. Meteorit. Planet. Sci. 50, 326–352. doi: 10.1111/maps.12425.

Wolf, D., Palme, H., 2001. The solar system abundances of phosphorus and titanium and the nebular volatility of phosphorus. Meteorit. Planet. Sci. 36, 559–571. doi: 10.1111/j.1945-5100.2001.tb01897.x.

Woo, J.M.Y., Brasser, R., Matsumura, S., Mojzsis, S.J., Ida, S., 2018. The curious case of Mars' formation. Astron. Astrophys. 617, A17. doi: 10.1051/0004-6361/201833148.

Woo, J.M.Y., Grimm, S., Brasser, R., Stadel, J., 2021. Growing Mars fast: High-resolution GPU simulations of embryo formation. Icarus 359, 114305. doi: 10.1016/j.icarus.2021.114305.

Woosley, S.E., 1997. Neutron-rich nucleosynthesis in carbon deflagration supernovae. Astrophys. J. 476, 801. doi: 10.1086/303650.

Worsham, E.A., Bermingham, K.R., Walker, R.J., 2017. Characterizing cosmochemical materials with genetic affinities to the Earth: Genetic and chronological diversity within the IAB iron meteorite complex. Earth Planet. Sci. Lett. 467, 157–166. doi: 10.1016/j.epsl.2017.02.044.

Worsham, E.A., Burkhardt, C., Budde, G., Fischer-Gödde, M., Kruijer, T.S., Kleine, T., 2019. Distinct evolution of the carbonaceous and non-carbonaceous reservoirs: Insights from Ru, Mo, and W isotopes. Earth Planet. Sci. Lett. 521, 103–112. doi: h10.1016/j.epsl.2019.06.001.

Yamakawa, A., Yamashita, K., Makishima, A., Nakamura, E., 2010. Chromium isotope systematics of achondrites: Chronology and isotopic heterogeneity of the inner Solar System bodies. Astrophys. J. 720, 150. doi: 10.1088/0004-637X/720/1/150.

Yamakawa, A., Yin, Q.Z., 2014. Chromium isotopic systematics of the Sutter's Mill carbonaceous chondrite: Implications for isotopic heterogeneities of the early Solar System. Meteorit. Planet. Sci. 49, 2118–2127. doi: 10.1111/maps.12346.

Yamashita, K., Maruyama, S., Yamakawa, A., Nakamura, E., 2010. ^{53}Mn-^{53}Cr chronometry of CB chondrites: Evidence for uniform distribution of ^{53}Mn in the early Solar System. Astrophys. J. 723, 20. doi: 10.1088/0004-637X/723/1/20.

Yoshizaki, T., McDonough, W.F., 2020. The composition of Mars. Geochim. Cosmochim. Acta 273, 137–162. doi: 10.1016/j.gca.2020.01.011.

Youdin, A.N., Shu, F.H., 2002. Planetesimal formation by gravitational instability. Astrophys. J. 580, 494. doi: 10.1086/343109.

Zellner, B., 1975. 44 Nysa: An iron-depleted asteroid. Astrophys. J. Lett. 198, L45. doi: 10.1086/181807.

Zellner, B., Leake, M., Morrison, D., Williams, J.G., 1977. The E asteroids and the origin of the enstatite achondrites. Geochim. Cosmochim. Acta 41, 1759–1767. doi: 10.1016/0016-7037(77)90208-3.

Zhang, H., Zhou, J.L., 2010. On the orbital evolution of a giant planet pair embedded in a gaseous disk. I. Jupiter-Saturn configuration. Astrophys. J. 714, 532. doi: 10.1088/0004-637X/714/1/532.

Zhang, J., Dauphas, N., Davis, A.M., Leya, I., Fedkin, A., 2012. The proto-Earth as a significant source of lunar material. Nat. Geosci. 5, 251–255. doi: 10.1038/ngeo1429.

Zhang, J., Dauphas, N., Davis, A.M., Pourmand, A., 2011. A new method for MC-ICPMS measurement of titanium isotopic composition: Identification of correlated isotope anomalies in meteorites. J. Anal. At. Spectrom. 26, 2197–2205. doi: 10.1039/C1JA10181A.